ISSN 1810-648X

ACADEMY OF SCIENCES
OF MOLDOVA

PHYSICAL SOCIETY OF MOLDOVA

STATE UNIVERSITY OF MOLDOVA

Moldavian Journal of the Physical Sciences

Chisinau
2015

Volume 14
No. 3-4

Scientific journal **Moldavian Journal of the Physical Sciences** includes original scientific articles, communications and reviews concerning various problems of modern physics. The journal is published in English, its periodicity is 4 numbers a year, with circulation of 200 copies.

web: http://sfm.asm.md/moldphys/

GUIDELINES FOR AUTHORS

The "Moldavian Journal of Physical Sciences" appears quarterly and publishes in English papers referring to original scientific research in physics and related fields, including applications in electronics and technology, material engineering and device physics. A review paper for every issue is planned and short communications with hot news are encouraged.

Papers must be prefaced by a brief abstract in English up to 100 words. Single space of the rows in the manuscript is required.

Authors are invited to send two printed copies of their papers, as well as an electronic record on a $3^{1/4}$ inches diskette, or by e-mail, in English. The articles will be edited by using WORD for Windows. Chapters must be numbered by using Arabic figures, as follows:

3. Experimental results.
3.1. Results analysis.
3.2. Methods of calculus.

Formulae must be written very clearly and easy-to-read. Do not use non-explained abbreviations. Illustrations and diagrams must be realized on computer drafts (on images). All graphic and text objects must be of very good quality and easy to read. Figures included in the text are preferable.

Reference citations will be presented as follows: author's forename initial and last name, journal name, volume, page number, year (in parentheses), for example: F.A. Moldovan, S.P. Russu, Phys. Rev. Let. 85, 357, (2000). Complete title, publisher, city and year will be written for book's author's name and forename initial, for example: M. Teodorescu, Cooperation in science and technology with Eastern and European countries, Editura Tehnica, Bucuresti, vol. 1, 1992. References into the text will be made within square brackets, for example [7]; reference citation numbers must be made successively, as they appear into the text.

Manuscripts of regular papers should be limited up to 10 pages and will be signed by authors; they also must be marked "Ready to print". Reviews are limited up to 20 pages. Maximum 4 pages are admitted for short communications. One full page of the journal (size A4) contains 54 rows with 95 characters/row; font size - 12. Page set up: top, left, right – 2,5; bottom – 3,5 cm. The very manuscript which is marked "Ready to print" will be published within 6 months from sending.

The submitted papers must be reviewed, if possible, by two independent reviewers. The papers must contain original work and have not submitted for publication to any other journal. The papers which have been published previously, as well those accepted to be published in other reviews, will be not be admitted by Editorial Board; the authors have to mention this situation.

Proofs will be sent to authors for checking. Corrections must be restricted to errors since modifications to the text may be charged to the author. The publishers reserve the right to adapt the presentation of an article to conform to our style. After their publishing in our journal, the manuscripts and corresponding illustrations become the property of Editorial Board and will not be returned to the authors. The same for the papers, which have not been admitted for publication. The publishing in our journal is made free of charge.

The papers sent for publishing are considered not secret. The authors only are responsible for this in front of their own institutes or employers. Authors have to mention their complete address and telephone, fax number and e-mail.

Papers from around the world can be sent to be published to the following address:

Department of Mathematical, Physical and Technical Sciences, 5 Academy St., MD 2028 Kishinev, the Republic of Moldova, tel. (+37322) 72-71-57, 73-81-66; E-mail: vcantser@phys.asm.md, E-mail of responsible secretary: sofiadonu@yahoo.com

RECOGNIZED RESEARCHER AND VALUABLE UNIVERSITY PROFESSOR ON THE OCCASION OF THE 80th ANNIVERSARY OF PROF. ANATOLIE CASIAN

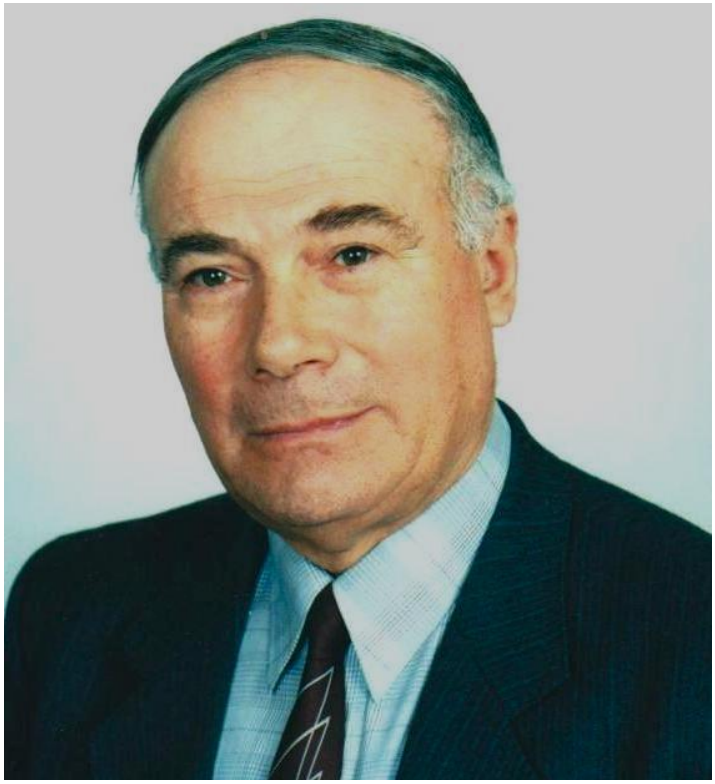

On November 17, 2015, Anatolie Iradion Casian (until 1995 Kasiyan), Head of Theoretical Mechanics Department of Technical University of Moldova, Professor, DSc, Academician of International Thermoelectric Academy, corresponding member of American-Romanian Academy of Arts and Sciences, Laureate of National Prize in the Domain of Science and Technique celebrated his eightieth anniversary.

Anatolie Casian was born in the village Colicautsi, Briceni region, Republic of Moldova. He graduated from the Department of Theoretical Physics with first degree honors of Kishinev State University (now State University of Moldova, Chisinau), in 1957. Being one of the best students during the study at the University, he received a Lenin scholarship. In the period of 1957–1960, he continued postgraduate study in theoretical physics at the same University. In 1965 he defended his candidate's dissertation (now doctoral) in physics and mathematics under the guidance of acad. V. Moscalenco. His dissertation was focused on the theoretical study of the polaron effect in ionic crystals taking into account the Coulomb interaction between the polarons. The coupled plasmon–phonon modes were studied, and the scattering of polarons on these mixed modes was considered in the framework of the developed approach based on the method of diagrams and Green functions. It was one of the most advanced treatments of the polaronic problems for that time.

In the period of 1960–1969, he was engaged at the Academy of Sciences of Moldova (ASM) in different positions: junior and senior researcher, scientific secretary of Physical-Technical and Mathematical Section of the ASM. At the same time, in 1962–1963, he studied at

Moscow State University under the supervision of acad. N. N. Bogoliubov. He used the opportunity to attend the course of Prof. V. L. Bonch-Bruevich, acad. A. A. Abricosov, and acad. I. M. Lifshits at Moscow State University for advancing his professional qualification. He also participated in work of the all scientific seminars headed by Prof. V. L. Bonch-Bruevich and Professors S. V. Tyablicov and D. N. Zubarev at the Steklov Institute of Mathematics. On this basis, he became one of the qualified physicists in Moldova.

At the end of the sixties (1967–1969), he was delegated in Algeria as Professor of Alger University. There, under his supervision, the assistant of Alger University Naziha Kesri defended the doctoral thesis; at that time, she was the second Algerian woman with a PhD degree at Alger University. Later, she defended the second thesis of DSc.

After the return from Algeria, A. Casian accepted the invitation of Rector, acad. S. Radautsan, and became the Head of Theoretical Mechanics Department of the Kishinev Polytechnic Institute until 1976. At this Institute position, he continued the activities on the consolidation of Theoretical Mechanics Department which was begun by the founder and the first Head of Department Dr. A. Marinciuc. Since 1970, he has been the scientific secretary of the Institute Council and has contributed essentially to the improvement of the Council's activities. In the period of 1976–1982, he worked at the Moldova Filial of Research Institute of Current Sources, Scientific and Production Enterprise Kvant, Moscow, as senior researcher, Head of laboratory, Vice director, and Director. There, he has established new scientific relations in the domain of thermoelectricity, in particular, the collaboration with Prof. Z. Dashevsky that continues up to now. From May 1982 till present, he works again at Kishinev Polytechnic Institute (now Technical University of Moldova) as the Head of Theoretical Mechanics Department. In 1988 he defended his doctoral dissertation (now Doctor Habilitat) "Kinetic Effects in Semiconductors and Multilayer Structures Caused by Dynamical Screening and Interference of Scattering Mechanisms." After that, in 1990, he received the title of university professor.

In 1994 he was elected full member of the International Thermoelectric Academy in and in 1999 a corresponding member of the American–Romanian Academy of Arts and Sciences. He was Vice-Head of theoretical physics Council at the Academy of Sciences of Moldova, Vice-Head of the PhD and DSc thesis examination board in theoretical physics at the Academy of Sciences of Moldova. He is a member of the International Editorial Board of "Journal of Thermoelectricity," Assistant Editor of "Moldavian Journal of the Physical Sciences," Academy of Sciences of Moldova, and a member of the editorial board of the journal "Physics and Modern Technologies," Chisinau.

For more than 50 years, Prof. A. Casian actively has been involved in different scientific investigations; he has more than 300 scientific publications, including 2 monographs and 7 manuals for students. He supervised more than 20 scientific projects. In the last years, he has participated, as a team leader, in the implementation of five International projects: INTAS-96-535; USA Grant N00014-97-C-0219 supported by Office of Naval Research, USA; CRDF-MRDA grant No ME-3010; INTAS-01-0184", STCU 5344. All these projects have been successfully implemented. At present, he participates, as a team leader, in the implementation of international project FP7 308768, together with four teams from the United Kingdom, Germany, Latvia, Bulgaria, and an industrial company from the United Kingdom. He presented reports at many international scientific conferences, including invited papers (most recently, at XIII, XIV, XV, and XVI International Forums on Thermoelectricity, 2009, 2011, 2013, and 2015). He participated with oral communications at European Conference on Thermoelectricity ECT-2013, Netherlands, and ECT-2014, Madrid. Prof. A. Casian received the Diploma of the

best paper at the 7th International Forum on Thermoelectricity, Kiev, 1996. He is Laureate of the National Prize in the Domain of Science and Technique (2004).

The name of Prof. A. Casian is well known in the scientific community. He was invited professor to the Ben-Gurion University, Beer-Sheva, Israel (1996 and 2002); H. Poincare University, Nancy, France (1997 and 1998); Institute Nationale Polytechnique de Lorraine, Nancy, France (2000) (for one month each year); office of Naval Research, Washington, USA (1999) where he presented a report to the Technical Council; University of California-Riverside (2002) for one week; Observatoir des Micro et Nano Technologies, Paris, France (2005); Institute of Surface Chemistry of Academy of Sciences of Ukraine, Kiev (2012, 2013); University of Wurzburg, Germany (2013); and Institute of Solide State Physics of Latvia University (2014), where he participated in seminars on thermoelectric organic materials. Under his guidance, seven PhD theses were defended and two theses are currently under preparation.

The area of scientific research of Prof. A. Casian is considerably extended by a lot of considered physical problems as well as by the diversity of investigated solid state materials: fundamental problems of the crystal lattice dynamics and the theory of semiconductors; transport and thermoelectric phenomena in low-dimensional quantum well structures; and thermoelectric properties of quasi-one-dimensional organic crystals. Some of the research directions where he has obtained new and valuable results are as follows.

1. *Theory of kinetic and optical phenomena in polar semiconductors under conditions of dynamic screening.*
2. *Thermoelectric effects in the structures with many p-n-homo and heterojunctions.*
3. *Kinetics of current of nonequilibrium carriers in the detectors of ionizing radiation.*
4. *Optical, transport, and thermoelectric properties of some low-dimensional structures.*
5. *Thermoelectric properties of quasi-one-dimensional organic crystals.*

The list of selective representative publications includes:

1. **A. I. Casian**, Kinetic effects in Semiconductors of Different Dimensionality (in Russian) Kishinev, *Stiintsa*, 1989, 122 p.
2. I. I. Balmus, Z. M. Dashevsky, and **A. I. Casian**, Thermoelectric Effects in Multilayered Semiconductors Structures (in Russian) Chisinau, *Stiintsa*, 1992, 144 p.
3. **A. Casian,** I. Sur, and A. A. Balandin, Modeling of the Electrical Conductivity in Multivalley PbTe/$Pb_{1-x}Eu_xTe$ Quantum Wells (chapter in *Nanoscience and Nanoengineering*, Series in Micro and Nanoengineering, V.3). Ed. by E. Andronescu, et al., *Romanian Academy of Sciences* Publishers, Bucharest, 2002.
4. **A. I. Casian**, Thermoelectric Properties of Electrically Conducting Organic Materials (Chapter 36 in *Thermoelectric Handbook: Macro to Nano-Structured Materials*). Ed. by M. Rowe, CRC Press, FL, USA, 2006.

Prof. A. Casian is still actively engaged in different investigations; this is certified by new results obtained in the last years. The most important publications of A. Casian in the last three years include:

1. **A. Casian** and I. Sanduleac. Thermoelectric properties of nanostructured tetrathiotetracene iodide crystals: 3D modeling. *Mat. Today. Proc*., 2, 504, (2015).
2. S. Andronic, **A. Casian**, and V. Dusciac. Peierls structural transition in Q1D crystals of TTF-TCNQ type for different values of carrier concentration. *Mat. Today. Proc*., 2, 3829, (2015).

3. I. Sanduleac and **A. Casian**. Nanostructured TTT(TCNQ)2 Organic Crystals as Promising Thermoelectric n-Type Materials: 3D Modeling. *J. Electron. Mat*. DOI 10.1007/s11664-015-4018-8, (2015).
4. **A. I. Casian**, J. Pflaum, and I. Sanduleac. Prospects of low-dimensional organic materials for thermoelectric applications, *J. Thermoelectricity,* N 1, 16, (2015).
5. **A. Casian** and I. Sanduleac. Thermoelectric Properties of Tetrathiotetracene Iodide Crystals: Modeling and Experiment, *J. Electron. Mat*, 43, 3740-3745, 2014. DOI: 10.1007/s11664-014-3105-6.
6. I. Sanduleac, **A. Casian**, and J. Pflaum. Thermoelectric Properties of Nanostructured Tetrathiotetracene Iodide Crystals in a Two-Dimensional Model, *J. Nanoeletron. Optoelectron*. **9**, 247-252, 2014. ISSN. 1555-130X (Open access).
7. **A. Casian** and V. Dusciac. Effect of Lorentz number decrease on thermoelectric efficiency in quasi-one-dimensional organic crystals. *J. Electron. Mat.* 42, 2151, 2013. DOI: 10.1007/s11664-013-2555-6.

Editorial Board of "Moldavian Journal of Physical Sciences" and Physical Society of Moldova heartily congratulate Anatolie Casian on the occasion of his jubilee and wish him good health and new creative achievements in the pedagogic and scientific activities.

ON THE OCCASION OF THE 80th BIRTHDAY OF GALINA FEDOROVNA VOLODINA

On July 2, 2015 Dr. Galina Volodina—well known crystallographer, doctor in physics and mathematics, senior scientific worker of the Laboratory of Physical Methods of Solid State Investigation "Tadeusz Malinowski" of the Institute of Applied Physics of the Academy of Sciences of Moldova—celebrated her 80th anniversary.

In 1958 Galina F. Volodina graduated from the Faculty of Physics and Mathematics of the State University of Rostov-on-Don, began the Doctoral studies in the Institute of Crystallography of the Academy of Sciences of the USSR in Moscow, and published her first scientific paper "Kristallicheskaya structura natrokhal'tsita" (Crystal Structure of Natrochalcite) in *Doklady Akademii Nauk SSSR*. In 1961 her next research papers addressing inorganic compounds containing rare earth elements and written in co-authorship with her supervisors—acad. N.V Belov and Prof. I.M Rumanova—were published in the leading scientific journal Kristallographiya. Her papers continuously attract attention of the researchers working in this field and have a good citation. On December 20, 1961 she was engaged as a scientific worker in the Institute of Chemistry of the Moldavian Academy of Sciences. In 1964 G. Volodina successfully defended her candidate's dissertation "The Application of Modified Weighted Projections for Determination of Structures with Large Cations: Praseodymium Nitrate Hexahydrate, Cainosite, and Natrochalcite," which was supervised by acad. Belov and Prof. Rumanova, and was awarded the scientific degree of Candidate of Physics and Mathematics (now Doctor).

In collaboration with acad. Ablov, Dr. Volodina has accomplished a study of a series of cadmium complexes containing aromatic amines and revealed temperature-dependent structural transitions in these solids.

In 1975 Dr. Volodina joined the Laboratory of Physical Methods of Solid State Investigation of the Institute of Applied Physics as a senior researcher and then—from 1980 to 1993—she headed the Department of roentgenographic methods of materials research at the Center for automation and metrology of the Academy of Sciences of Moldova. In this period, her efforts were concentrated on the implementation of phase X-ray structural analysis for all requesting organizations and scientific centers in Moldova; this target has been successfully achieved.

In 1993 she came back to the Laboratory of Physical Methods of Solid State Investigation of the Institute of Applied Physics where she has been working fruitfully until now. The scientific results obtained by Dr. Volodina were published in 65 scientific articles and presented at scientific conferences in the form of about 70 abstracts. In 2005 at the International Exhibition in

Chisinau, Moldova, among a group of scientists, Dr. Volodina was awarded a silver medal for the research "ASE Technologies with the Use of New Electrode Materials: The Method of Identifying Products of Aluminum Alloys." She was also awarded a “Veteran al Muncii” Medal (1988) and an Honorable Diploma of the Presidium of the Academy of Sciences of Moldova (2004, 2010).

Galina Fedorovna is a very talented researcher and devoted crystallographer; she celebrates her 80th anniversary being full of energy and creative power. She holds a most unique position in the physical, chemical, geological, and crystallographic community in Moldova. Intellect, intelligence, and kindness are evident in all the actions of her everyday life.

Dear Galina Fedorovna, we wish you good health and a lot of achievements in that scientific field which you are so faithful to.

Laboratory of Physical Methods of Solid State Investigation “Tadeusz Malinowski” of the Institute of Applied Physics, Academy of Sciences of Moldova

PETRU DUMITRAS
A RECOGNIZED EXPERT IN CAVITATION TECHNOLOGIES
(ON THE OCCASION OF THE 70th ANNIVERSARY)

Doctor of Engineering, Associated Professor, Leading Researcher, expert in the field of intensification of the processes of heat and mass transfer under the action of cavitation fields and high power ultrasound

Petru Dumistras, our colleague and good friend for many years, was born in one of midsummer days, on July 11 of the memorable year 1945 in a picturesque area near Soroca. He has been working in the Institute of Applied Physics from 1974 and occupied positions from engineer to the Head of Laboratory.

He spent his childhood in a family of good hosts in the Rublenita village, finished the Soroca secondary school (1963) and in the same year became a student at the Kishinev State University (now State University of Moldova, Chisinau). After military service (1964) he continued his studies at the Kishinev Polytechnical Institute (now Technical University of Moldova). After graduation from the Institute, he began his academic and research activities as an assistant at the Chair of Descriptive Geometry of this institute. In 1975 he continued his studies as a trainee and post-graduate student at the Moscow Institute of Steel and Alloys and defended his candidate's dissertation (now doctoral) in 1980.

As a young researcher, he began to work in the field of physics and engineering application of ultrasound. He investigated the mechanisms of ultrasonic effects and ultrasonic cavitation, studied the action of cavitation fields on the physicochemical characteristics of

materials at the liquid–liquid, liquid–solid, and liquid–solid–gas interfaces.

At the beginning of the 1990s, Petru Dumitras, in collaboration with the researchers of the Moscow Institute of Steel and Alloys and Gh. Asachi Technical University in Iasi, was involved in active fundamental research related to the action of bifrequency cavitation on the processes of dispergation and homogenization in heterogeneous systems.

On the basis of the performed fundamental research, new methods, techniques and equipment have been developed for the intensification of technological processes for the electrotechnical, food processing, textile, pharmaceutical industries. Several domains of research can be named: "Intensification of processes of metallization and impregnation of superconductive cables with metals and alloys under the action of cavitation ultrasonic field"; "Technology and equipment for preparation of starch sizes for impregnation of cotton yarns"; "Technology and equipment for dispergation and homogenization during preparation of natural juices"; "Technology and equipment for dispergation and homogenization of bentonite for clarification and deproteinization of wines and juices". The cavitation techniques and equipment have been introduced in practice at various enterprises in Moldova, Romania, Russia, and Ukraine.

Petru Dumitras has been responsible for investigations related to the application of cavitation fields for preparation of metal coatings by materials with low wettability, fine dispergation, and homogenization of heterogeneous systems (emulsions and suspensions) in the framework of institutional, governmental, and international projects.

Permanently working in the direction of improvement of technological processes in cavitation field, P. Dumitras published more than 140 scientific works, received 13 patents, and participated at numerous national and international conferences.

He is a good-minded colleague, a respectable member of the family of Christians Dumitras known for ages, a founder and counsellor of the known Peter and Paul church in Chisinau municipality.

Dear colleague, may you spend the range of decades following ahead in harmony with your wishes and realizations.

Colleagues of the Laboratory of Thermal and Hydrodynamic Processes of the Institute of Applied Physics, Academy of Sciences of Moldova

SYNTHESIS AND OPTICAL CHARACTERIZATION OF $Eu(TTA)_3(Ph_3PO)_2$

O. T. Bordian[1], V. I. Verlan[1*], M. S. Iovu[1], I. P. Culeac[1], V. E. Zubarev[2], D. E. Bojin[3], and M. Enachescu[3]

[1]Institute of Applied Physics, Academy of Sciences of Moldova, Academiei str. 5, Chisinau, MD-2028 Republic of Moldova
[2]Institute of Chemistry of the Academy of Sciences of Moldova, Academiei str. 3, Chisinau, MD-2028 Republic of Moldova
[3]CSSNT, University Politehnica of Bucharest, Nr 313 Splaiul Independentei, sector 6, Bucharest, RO-060042, Romania
*E-mail *vverlan@gmail.com*

(Received October 15, 2015)

Abstract

Coordination compound tris(thenoyltrifluoroacetonato)bis(triphenylphosphine oxide) europium(III) $Eu(TTA)_3(Ph_3PO)_2$, where TTA is the thenoyltrifluoroacetonate monoanion ($C_8H_5F_3O_2S$), Ph_3PO is triphenylphosphinoxide (TPPO), is synthesized. Solutions with different molar ratios of $Eu(TTA)_3(Ph_3PO)_2$ and thin film samples is characterized by optical transmission and photoluminescence (PL) spectroscopy. The displacement of the absorption threshold to infrared is observed with increasing coordination material concentration in solutions. PL emission at T = 300 K in the solutions and the bulk material is detected as specific bands of the internal transitions in the *4f* shell of the Eu^{3+} ion $^5D_0 \rightarrow {}^7F_i$ (i = 0,1,2,3 and 4) centered at 537, 578, 615, 650, and 702 nm. The dominant PL band is positioned at 615 nm with the FWHM less than 10 nm, and this band is attributed to the transition $^5D_0 \rightarrow {}^7F_2$.

1. Introduction

Coordination compounds of rare earth metals are excellent materials for a new generation of light emitting devices with high efficiency, easy color tuning, temperature insensitivity, and high stability [1]. Owing to excellent PL properties, these compounds and solutions thereof are widely used in medicine, solar cells, optical amplifiers, etc. For application in visible spectrum, compounds with europium (Eu^{3+}) and terbium (Tb^{3+}) ions are more frequently used. Improvement of the luminescence properties of the compounds depends on the type of ligands used for surrounding of the rare earth ions. For example, in this case, photoactive complexes of organic compounds of lanthanides may be used, such as the trivalent ion of Eu^{3+} chelated with β-diketonates, or the cyclic ligands of carboxylate, when the coordination number of Eu^{3+} varies in a range of 6–9 [2]. The efforts of the researchers have been oriented towards achieving compatible coordinated surrounding of the Eu^{3+} ion in order to improve the luminescence efficiency and prepare a final stable compound.

Spectroscopic studies of rare earth organic compounds and applications of the technology associated with effective luminescence with the half-width of the luminescence (FWHM) less than 10 nm in the visible and near-infrared are of special interest. An advantage of application of coordination compounds of rare earth ions with β-diketonates and ligands is based on the so-called "antenna" effect, or the transfer of excitation energy from outside of the system of Eu^{3+} ion towards

the energy levels thereof [2–5]. In this case, the population of upper energy levels increases with subsequent transition to ground states. Strong luminescence of lanthanide complexes determines the application as excitation energy transfer additives in polymer materials in optoelectronics, biology, power industry, and medicine.

Over the last years, attention has been focused on studying the structure and luminescent properties of europium complexes with different acceptor diketonates and donor ligands [6]. The use of these diketonetes and donor ligands gives the possibility to modify the symmetry of the structure around the rare earth ion and thus allow transitions *4f* → *4f*, which are forbidden in the symmetric spherical surround of the Eu^{3+} ion, making luminescence uninterrupted without accumulation or loss of energy, and the application of dissolution of coordination compounds in different solvents, both polar and nonpolar.

2. Experimental

The synthesis of coordination compound of tris(thenoyltrifluoroacetonato)bis(triphenylphosphine oxide)europium(III) ($Eu(TTA)_3(Ph_3PO)_2$) was conducted similar to the scheme described in [7] with some modifications. All chemicals were purchased from Aldrich Chemical Company.

Synthesis: 0.66 g (3 mmole) of thenoyltrifluoroacetone (TTA) and 0.56 g (2 mmole) of triphenylphosphine oxide (TPPO) were dissolved in 10 mL of warm 96% ethanol and 3 mL of a 1 N sodium hydroxide solution was added. The mixture was stirred, while 1 mmole of europium chloride in 5 mL of water was added dropwise. A light pink precipitate was immediately formed. The precipitate was filtered off, washed with small portions of ethanol and diethyl ether, dried thoroughly in air, and the solid of the complex was obtained. The yield was 0.68 g.

For $C_{60}H_{42}F_9EuO_8P_2S_3$ calcd, %: C = 52.53; H = 3.09.

Found, %: C = 52.37; 52.28; H = 3.18; 2.98.

Structural formula of $Eu(TTA)_3(Ph_3PO)_2$ ($C_{60}H_{42}F_9EuO_8P_2S_3$) [8] is represented in Fig. 1.

Solutions of $Eu(TTA)_3(Ph_3PO)_2$ in toluene were prepared with different ratios of weight concentrations, %: 0.017, 0.053, 0.16, 0.5, 1.5, 4.5, and 13.6.

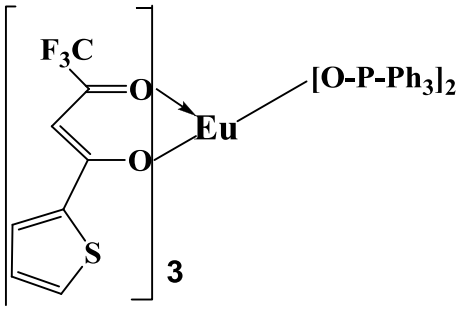

Fig. 1. Structural formula of $C_{60}H_{42}F_9EuO_8P_2S_3$.

Microscopic investigations of the morphology of the surface were carried out with a TEM EM 410 transmission electron microscope. PL spectra excited by a N_2-laser (λ = 337 nm) or a diode laser (λ = 405 nm) were measured using a set-up based on an MDR-23 monochromator connected to a PC. For optical transmission investigations, a Specord UV/VIS (300–800 nm) CARL ZEISS Jena unit was used. All the measurements were performed at room temperature.

The Fourier transform infrared (FTIR) spectra were measured on a Perkin-Elmer infrared spectrophotometer using the KBr pellet technique.

3. Experimental results

TEM examination of solutions of the powder samples in a toluene solution reveals that $Eu(TTA)_3(Ph_3PO)_2$ complexes are dispersed homogenously without any phase separation. According to TEM, the dimensions of the $Eu(TTA)_3(Ph_3PO)_2$ particles in the thin films and in the solutions are in a range of 20–30 nm.

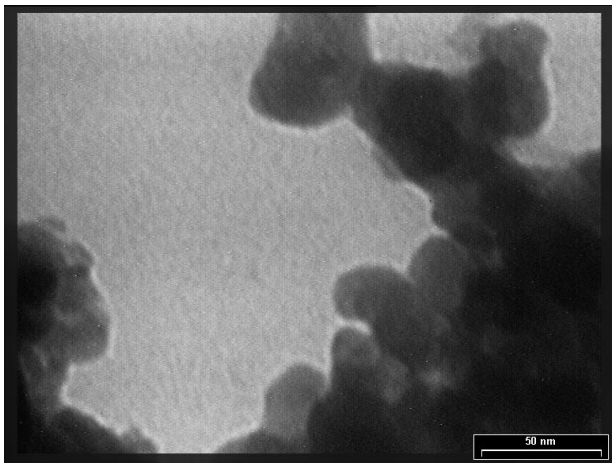

Fig. 2. TEM image showing the distribution of $Eu(TTA)_3(Ph_3PO)_2$ particles.

Figure 3 illustrates optical transmission spectra of the solution of $Eu(TTA)_3(Ph_3PO)_2$ particles in toluene at different concentrations. The absorption threshold in the domain of 320–400 nm can be clearly seen; with an increase in the $Eu(TTA)_3(Ph_3PO)_2$ concentration in the solution, it is shifted towards the infrared. Figure 3 shows the transmission spectrum of the thin film samples deposited on a quartz substrate. Transmission spectra $T(\lambda)$ of the solutions with different $Eu(TTA)_3(Ph_3PO)_2$ concentrations in the ultraviolet (UV) clearly show absorption bands peaking at 3.39, 4.56, 5.37, and 6.14 eV. A sharp absorption threshold is present at all concentrations of the $Eu(TTA)_3(Ph_3PO)_2$ coordinated compounds in a spectral range of 370-380 nm.

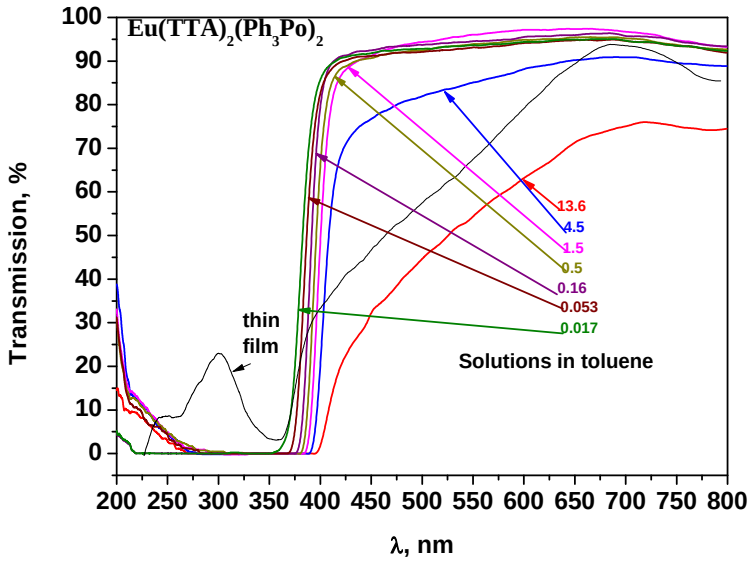

Fig. 3. Transmission spectra of the solutions and the thin layers deposited on quartz substrates at different $Eu(TTA)_3(Ph_3PO)_2$ concentrations at room temperature.

Absorption spectra $\alpha(\lambda)$ are calculated from transmission spectra $T(\lambda)$ through the relation ship $D(\lambda) = \alpha(\lambda)cl = - lnT$, where D is the optical density, c is the molar concentration of $Eu(TTA)_3(Ph_3PO)_2$ in solution, l is the thickness of the measuring quartz cuvette, and α is the absorption coefficient. The band-gap energy of the NC, ΔE_{HL} = LUMO – HOMO, (where HOMO is the energy of the highest occupied molecular orbital, and LUMO is the energy of the lowest unoccupied molecular orbital), which is obtained from 80% of the absorption threshold $T(\lambda)$, are in a range of 3.14–3.16 eV.

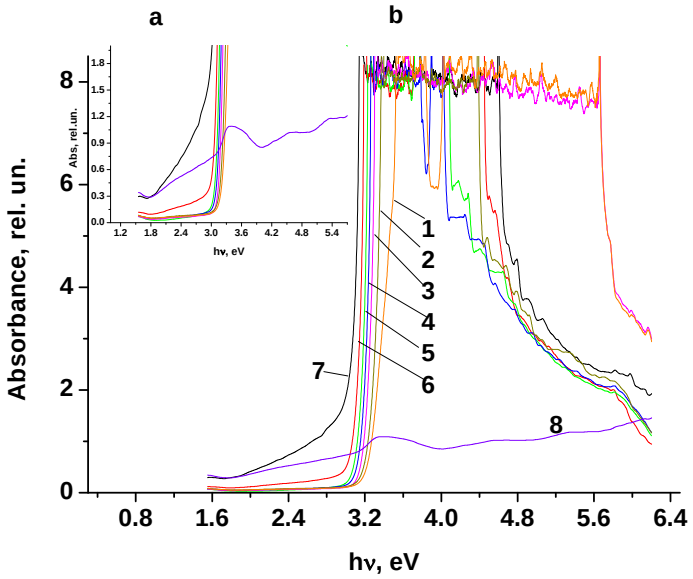

Fig. 4. Absorption spectra of the solutions and the thin layer on a quartz substrate at different $Eu(TTA)_3(Ph_3PO)_2$ concentrations in solution at room temperature, wt %: (*1*) 4.5, (*2*) 1.5, (*3*) 0.5, (*4*) 0.16, (*5*) 0.053, (*6*) 0.017; (*7*) the thin film of $Eu(TTA)_3(Ph_3PO)_2$; *(8)* thin layer $Eu(TTA)_3(Ph_3PO)_2$/PEPC deposited on quartz substrate.

The difference in the absorption onset of the solutions with different $Eu(TTA)_3(Ph_3PO)_2$ concentrations is mostly determined by the difference in the particles size which probably increases with increasing concentration. This fact is generally attributed to particles aggregation; it is confirmed by the registered TEM images.

Figure 5 illustrates the PL spectra of the $Eu(TTA)_3(Ph_3PO)_2$ solution in toluene under excitation of an N_2-laser beam. The registered PL bands correspond to the radiative transitions between the energy *4f*-levels of the Eu^{3+} ions and are centered at 537, 578, 615, 650, and 702 nm and can be attributed to the spin forbidden $4f \rightarrow 4f$ transitions $^5D_0 \rightarrow {}^7F_i$ (i = 0, 1, 2, 3, 4). The most effective luminescence at room temperature has a maximum at 615 nm, which is about 20 times higher than that of other PL bands, and its half-width is less than 10 nm. The PL intensity of almost monotonically increases with increasing compound concentration in the solution; this feature is characteristic of all thin film samples at room temperature.

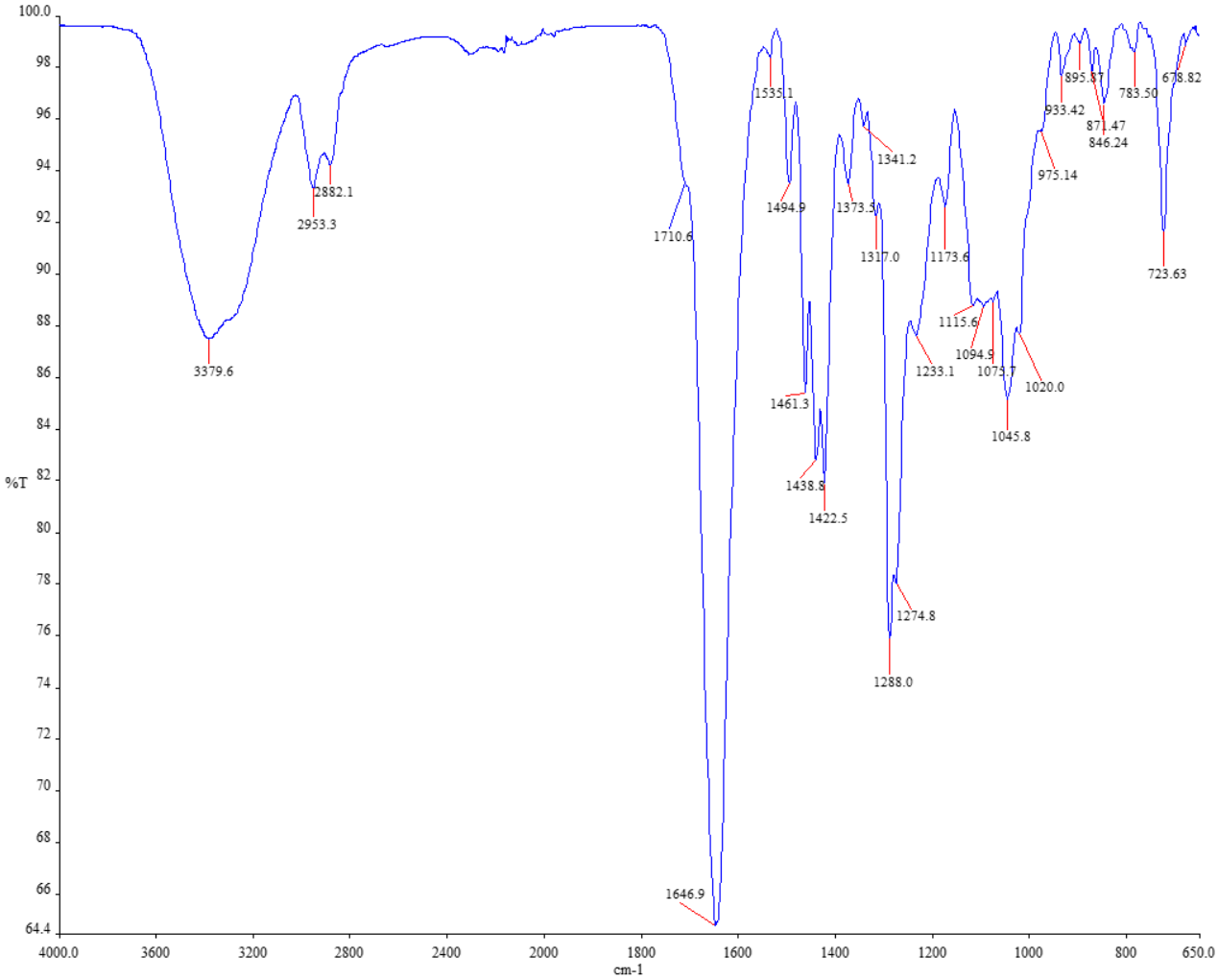

Fig. 5. IR transmission spectra of the thin film samples deposited on quartz substrates at different $Eu(TTA)_3(Ph_3PO)_2$ concentrations at room temperature.

Table 1. Positions of the IR absorption peaks (cm^{-1}) for the $Eu(TTA)_3(Ph_3PO)_2$ powder samples (cm^{-1})

λ, cm^{-1}	λ, cm^{-1}	λ, cm^{-1}	λ, cm^{-1}	λ, cm^{-1}
3379.6	1494.9	1317.0	1094.9	895.9
2953.3	1461.3	1288.0	1075.7	871.5
2882.1	1438.8	1274.8	1045.8	846.2
1710.6	1422.5	1233.1	1020.0	783.5
1646.9	1373.5	1173.4	975.1	723.8
1535.1	1341.2	1115.6	933.4	671.8

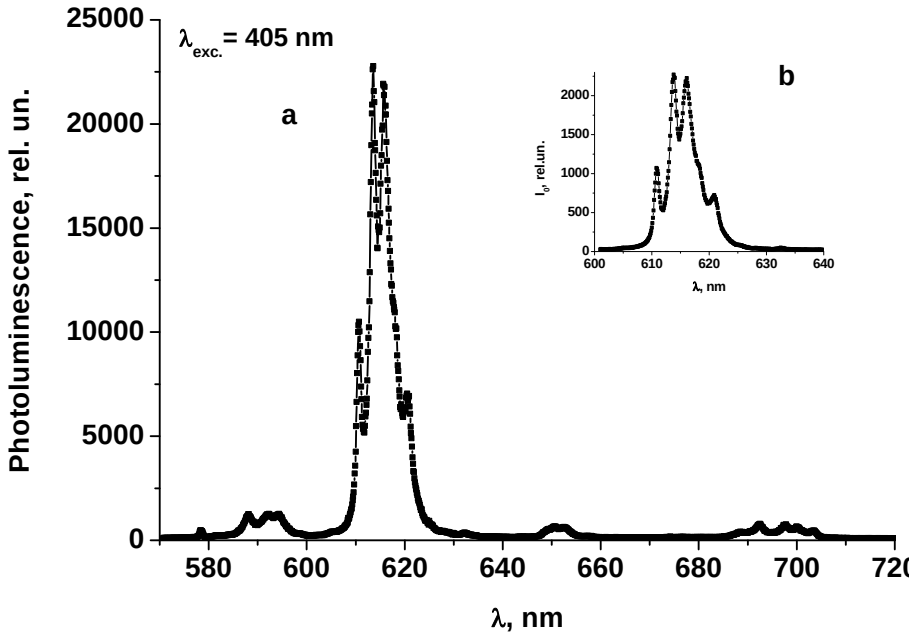

a), b)

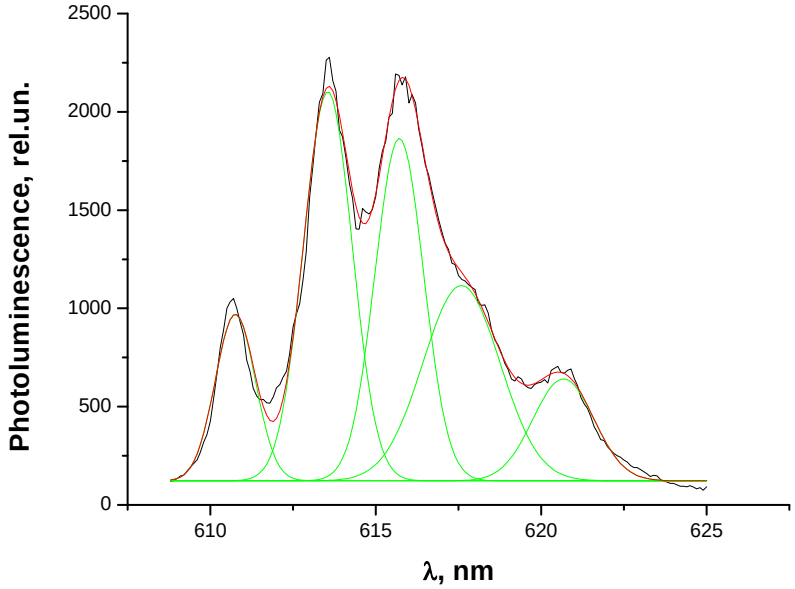

c)

Fig. 6. PL spectra at room temperature of thin sample layers of the $Eu(TTA)_3(Ph_3PO)_2$ complex: (a) the total spectrum; (b) PL graphic in the interval (600 – 640 nm) (c) the detailed spectrum of main maximum.

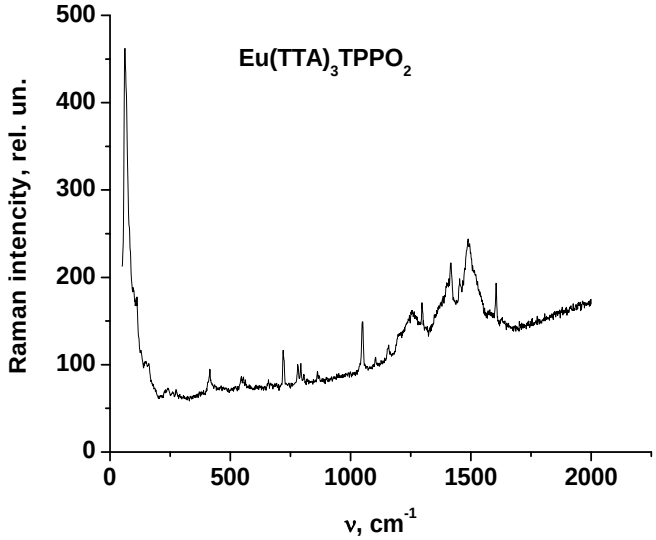

Fig. 7. Raman spectrum of the $Eu(TTA)_3(Ph_3PO)_2$ powder.

Table 2. The position of maxima of Raman interactions in the $Eu(TTA)_3(Ph_3PO)$ powder

λ, cm^{-1}	λ, cm^{-1}	λ, cm^{-1}	λ, cm^{-1}
69.5	667.2	1108.6	1420.0
156.7	723.2	1164.7	1488.4
237.6	791.7	1208.3	1575.5
418.1	870.0	1258.1	1606.7
548.9	1046.9	1295.4	

4. Discussion

There is a rather weak and broad band at 578.5 nm associated with the $^5D_0 \rightarrow {}^7F_0$ transition. Based on selection rules, the band at 594 nm is attributed to the $^5D_0 \rightarrow {}^7F_1$ parity-allowed magnetic dipole transition, which is independent of the surroundings symmetry. The $^5D_0 \text{—>} {}^7F_2$ transitions are allowed electrical-dipole transitions. The most intensive band around 614 nm belongs to the $^5D_0 \text{-}\rightarrow {}^7F_2$ transition, which is hyper-sensitive to the symmetry of the crystal field surrounding the Eu ion, and will be relatively strong if the surroundings symmetry is low. In this respect, it is known that the ratio of emission intensities $R = I(^5D_0 \rightarrow {}^7F_2)/I(^5D_0 \rightarrow {}^7F_1)$ is an asymmetry parameter for the Eu^{3+} sites and a measure of the extent of Eu^{3+} interaction with surrounding ligands, indicating on the environment of the Eu^{3+} ion.

In Fig. 5, one can clearly observe two well developed emission lines centered at 652 and 702 nm that originate from $^5D_0 \rightarrow {}^7F_3$ and $^5Do \rightarrow {}^7F_4$ transitions, respectively. It is also important to note that crystallized particles exhibit much stronger luminescence emission.

PL spectra characterize the efficiency of energy transfer from the LUMO energy levels of chelates and ligands of the compound to the energetic levels of Eu^{3+} ion of 4f level: $^5D_0 \rightarrow {}^7F_i$. HOMO and LUMO levels of the $Eu(TTA)_3(Ph_3PO)_2$ complex are found to be situated between

levels *S* and *T* of the ligands; this case is similar to doping of semiconductors.

The registered PL emission spectra are similar to those of the respective $Eu(TTA)_3Phen$ complex [1–2], and half widths of the strongest PL band are found to be less than 10 nm. In the case of this band, $Eu(TTA)_3(Ph_3PO)_2$ exhibits the most high fluorescence intensity and color purity. In this case, the PL displays a bright and narrow Eu^{3+} ion emission, which is due to the so-called "antenna" effect, defined as a light conversion process via an absorption energy transfer-emission sequence, involving distinct photon absorption by a ligand and subsequent energy transfer to Eu^{3+} ions and final photon emission. The PL experimental data can be explained taking into account the surrounding environment of the Eu^{3+} ion. For the Eu complex, the intensity of optical transitions $^5D_0 \rightarrow {}^7F_i$ (i = 0, 1, 2, 3, 4) increases with increasing $Eu(TTA)_3(Ph_3PO)_2$ concentration in the solutions (Fig. 8).

The difference of the PL spectra of the $Eu(TTA)_3(Ph_3PO)_2$ complex in different solutions can be interpreted as follows. If complexes of particles are dissolved in solutions, the molecular motion is restricted and the stretching and bond vibrations are weakened by the solutions, both of which decrease the nonradiative transition. These results indicate that the solutions cannot provide a relatively stable environment for lanthanide complexes.

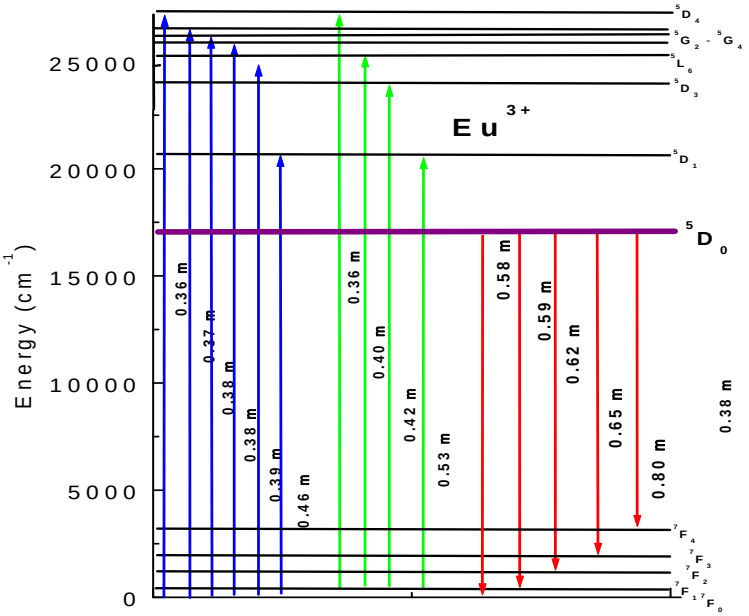

Fig. 8. Illustration of optical transitions in the 4f shell of the Eu^{3+} ion related to absorption (blue and green arrows) and emission processes (red arrows).

We can suppose that the interaction of macromolecular ligands and the Eu^{3+} ion in solutions leads to the partial formation of coordinated unsaturated complexes and ionic aggregates resulting in the luminescence quenching. From the PL spectra (Fig. 6), we can suppose a low local symmetry of the ligand field of the Eu^{3+} ion owing to the observed line transition $^5D_0 \rightarrow {}^7F_0$, which is forbidden under the high symmetry of the luminescence centre. The intensity of the transition $^5D_0 \rightarrow {}^7F_0$ is comparable with intensities of $^5D_0 \rightarrow {}^7F_1$, indicating also a significant asymmetry around of the rare-earth ions. The presence of splitting of all transition lines $^5D_0 \rightarrow {}^7F_i$ on five components indicates also the absence of an axial symmetry of the inner coordination sphere of the central Eu^{3+} ion [1].

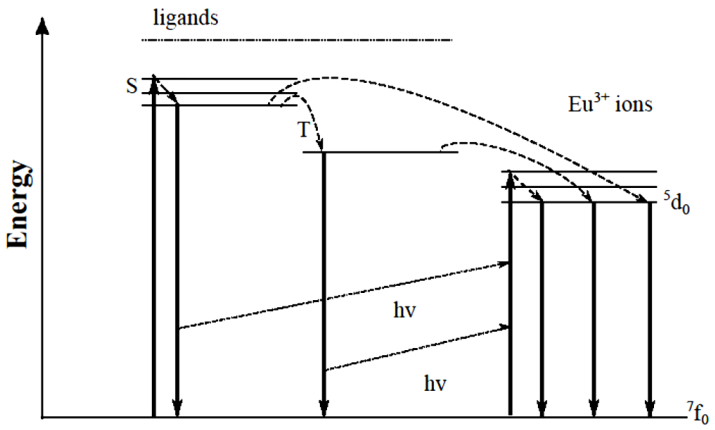

Fig. 9. Illustration of the mechanism of energy transfer and PL in the $Eu(TTA)_3(Ph_3PO)_2$ solution in toluene.

5. Conclusions

A PL solution based on the $Eu(TTA)_3(Ph_3PO)_2$ coordination compound has been synthesized and characterized by PL and UV-Vis absorption spectroscopy. From the transmission spectra, we have identified the basic absorption bands with maximums centered at 3.8, 4.5, and 4.8 eV in the UV. The absorption threshold has been estimated as E_{LH} = 3.15 eV. It is slightly shifted to *IR* with increasing $Eu(TTA)_3(Ph_3PO)_2$ concentration in the solution.

The PL properties can be attributed to the internal *4f* transition of the Eu^{3+} ion $^5D_0 \rightarrow {}^7F_i$ (i = 0, 1, 2, 3, 4). The FWHM of the PL band at 615 nm is less than 10 nm; this fact suggests that the $Eu(TTA)_3(Ph_3PO)_2$ compound exhibits high emission and color purity. Each maximum of the PL band is split in five components.

The positive effect of TTA and TPPO ligands on the coordinative environment of the Eu^{3+} ions has been found. A possible method for improving the fluorescence efficiency of $Eu(TTA)_3(Ph_3PO)_2$ is the energy transfer from *S* and *T* of ligands levels to internal *4f* levels of the Eu^{3+} ion. This research may provide a new method for designing and studying the crystal structure and symmetry of the luminescent $Eu(TTA)_3(Ph_3PO)_2$ hybrid material for the preparation of UV excited devices; further studies are currently underway.

Acknowledgments. This work was supported by the Romanian Executive Agency for Higher Education, Research, Development and Innovation Funding (UEFISCDI) through the program PN-686/ 22.04.2013, by the Supreme Council for Science and Technological Development (CSȘDT) of the Academy of Sciences of Moldova of numbers 15.817.02.03A and research grants 11.817.05.03A, 13.820.05.15/RoF and 14.819.02.20A.

References

[1] Koen Binnemans, Rare-Earth Beta-Diketonates, in Handbook on the Physics and Chemistry of Rare Earths, ed. by K. A. Gschneidner, Jr., J.-C. G. Bünzli and V. K. Pecharsky, Elsevier, vol. 35, ch. 225, pp. 107–271, 2005.

[2] M. S. Iovu, A. M. Andriesh, S. A. Buzurniuc, V. I. Verlan, M. I. Caraman, and V. E. Zubarev, J. Optoelelectron. Adv. Mater. 10 (4), 841, (2008).

[3] A. Andriesh, S. Buzurniuc, V. Verlan, M. I. Caraman, S. Robu, and N. Barba, J. Optoelelectron. Adv. Mater. 10, 353, (2008).
[4] M. S. Iovu, A. M. Andriesh, S. A. Buzurniuc, V. I. Verlan, C. I. Turta, V. E. Zubareva, and M. I. Caraman, J. Non-Cryst. Solids 355, 1890, (2009).
[5] M. S. Iovu, S. A. Buzurniuc, V. I. Verlan, I. P. Culeac, and Yu. H. Nistor, Advanced Topics in Optoelectronics, Microelectronics, and Nanotechnologies IV, Ed. by P. Schiopu, C. Panait, G. Caruntu, and A. Manea, Proc. SPIE 7297, 729703, (2009).
[6] V. A. Batyreva, A. I. German, and V. V. Serebrenikov, Synthesis of Rare Earth Compounds, Part 2, Tomsk, University of Tomsk, 1986, p. 121.
[7] V. I. Verlan, M. S. Iovu, I. Culeac, Y. Nistor, C. I. Turta, V. E. Zubareva, and S. Buzurniuc, J. Non-Cryst. Solids 357, 1004, (2011).
[8] Cambridge Structural Database. www.ccdc.cam.ac.uk/data_request/cif.

EXPERIMENTAL AND THEORETICAL FIELD DEPENDENCES OF THE THERMOPOWER OF $Pb_{1-x}Sn_xTe$

D. Meglei and S. Alekseeva

Gitsu Institute of Electronic Engineering and Nanotechnologies,
Academy of Sciences of Moldova
E-mail: alexeeva@nano.asm.md

(Received November 04, 2015)

Abstract

Experimental studies of transport phenomena in $Pb_{1-x}Sn_xTe$ provide the most complete information on the kinetics and energy spectrum of charge carriers over a wide range of charge carrier concentration, impurities, and temperature.

Experimental field dependences of the thermopower of $Pb_{1-x}Sn_xTe$ with different carrier concentrations were determined at a temperature of 77 K in magnetic fields of up to 3 T; theoretical field dependences were calculated. The dependence of the thermopower on magnetic field exhibited a peak. The nonmonotonic dependence of the thermopower can be attributed to the anisotropy of the electron spectrum, the anisotropy of the electron relaxation time, and the multivalley pattern.

The differential thermopower was calculated using the formula given in the paper of V. D. Kagan, N. A. Red'ko, N. A. Rodionov, and V. I. Pol'shin. Satisfactory agreement between theory and experiment was obtained.

1. Introduction

Significant interest in studying the properties of narrow-gap semiconductors, particularly lead telluride–tin telluride single crystals, is attributed to wide possibilities of the practical use of these materials as detectors and radiation sources in the infrared spectrum, thermocouples, strain gauges, etc. At the same time, scientific interest in these materials is primarily associated with their unusual galvanomagnetic, thermomagnetic, and magneto-optical properties.

Calculation of kinetic coefficients in semimetals and narrow-gap semiconductors in general is an extremely difficult problem because it is impossible to strictly take into account all the factors related to charge transfer in the crystal owing to the strong nonparabolicity of the bands and the complex mechanism of carrier scattering.

However, an experimental study of transport phenomena in these semiconductors provides the most complete information on the kinetics and energy spectrum of charge carriers over a wide range of variation in the charge carrier concentration, impurities, and temperature.

2. Results and Discussion

The quality requirements for the samples under study are very high in order to obtain reliable experimental results: the volume distribution of the components must be uniform, and mechanical defects must be reduced to minimum. The most effective technique for preparing homogeneous $Pb_{1-x}Sn_xTe$ single crystals is the gas-phase growth method. We have developed a

special technology for gas-phase growth of single crystals using high-purity Pb, Sn, and Te of the OSCh-0000 grade as initial materials (Te was purified by multiple zone recrystallization). Microstructural and spectral studies and Hall-effect measurements have confirmed the high quality of the prepared $Pb_{1-x}Sn_xTe$ (x = 0.18) single crystals.

To determine the concentration, charge sign, and mobility of carriers, measurements of the Hall effect and electric conductivity were conducted. Measurements of the temperature dependence of thermoelectric power, electric conductivity, and Hall effect in the same samples made it possible to calculate the parameters of $Pb_{1-x}Sn_xTe$ (x = 0.18). In our previous studies [1, 2], using $Pb_{0.82}Sn_{0.18}Te$ samples with the same carrier concentrations, the Shubnikov-de Haas oscillations and the temperature dependences of thermopower were examined. Based on the data, using the formulas given in [3–5], a number of kinetic coefficients were calculated (Table 1).

Table 1. Characteristics of $Pb_{1-x}Sn_xTe$ (x = 0.18) at 77 K

Sample	Carrier concentration p, 10^{17} cm^{-3}	Carrier mobility μ, cm^2/(V s), 10^4	Fermi energy, E_f, eV	$\frac{m_{eff}}{m_0}$, 10^2
3	5.2	0.37	0.03	3.1
4	2.6	1.91	0.017	1.8
5	0.52	2.34	0.066	0.6

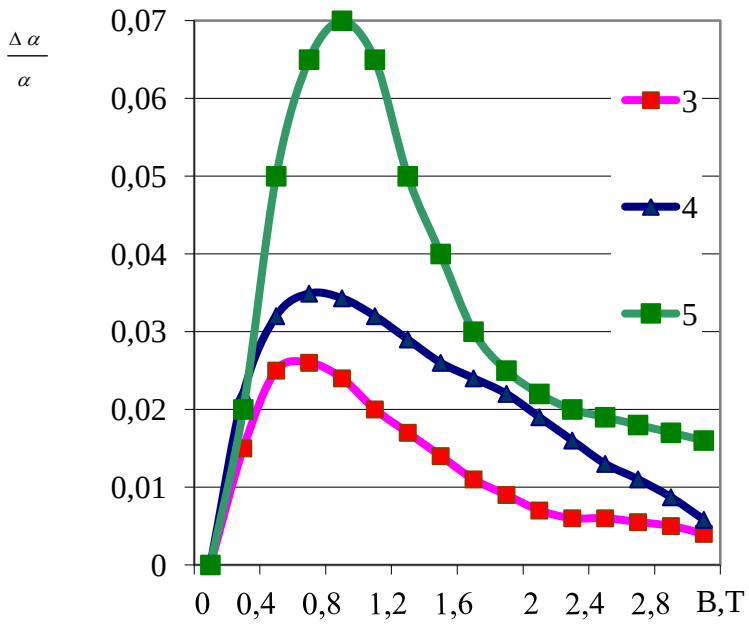

Fig. 1. Field dependences of differential thermopower $\frac{\Delta\alpha}{\alpha}$ on magnetic field induction B for three $Pb_{0,82}Sn_{0,18}Te$ samples with different charge carrier concentrations. Hole concentration, cm^{-3} ,77 K, 10^{17} : 3-5.2; 4-2.6; 5-0.52.

In this study, field dependences of the thermopower of $Pb_{0.82}Sn_{0.18}Te$ samples at different carrier concentrations ($0.52 \cdot 10^{17}$ to $5.2 \cdot 10^{17}$ cm^{-3}) have been examined. The results have shown that the thermopower heavily depends on charge carrier concentration (Fig. 1)

Using the experimental data shown in Fig. 1, the field dependences of differential thermopower $\frac{\Delta\alpha}{\alpha}$ of $Pb_{0,82}Sn_{0,18}Te$ at different carrier concentrations were calculated. The theoretical calculations were based on the following analytical dependences of $\frac{\Delta\alpha}{\alpha}$ on magnetic field induction *B*:

$$\frac{\Delta\alpha(B)}{\alpha(0)} = k\left[1 + \frac{\Omega^2\tau^2(\delta - 2) - \delta}{(1 + \Omega^2\tau^2)(\delta + \Omega^2\tau^2)}\right] \tag{1}$$

$$k = \frac{3\left(1 + 2\frac{E_f}{E_g}\right)}{2\left(1 + \frac{E_f}{E_g}\right)} - \beta \tag{2}$$

$$\Omega = \frac{eB}{m_{eff}} \tag{3}$$

where Ω is the cyclotron frequency, τ is the charge carrier lifetime, E_f is the Fermi energy, E_g is the bandgap, β is an adjustable parameter associated with the dependence of relaxation time τ and effective mass m_{eff} on the Fermi energy, and δ is the parameter that takes into account the energy spectrum anisotropy.

Equation (1) implies that the function of $\frac{\Delta\alpha}{\alpha}$ has a maximum at

$$(\Omega\tau)^2 = \frac{\delta + (\delta - 1)\sqrt{2\delta}}{\delta - 2} \tag{4}$$

Thus, the experimental data on $\frac{\Delta\alpha}{\alpha}$ shown in Fig. 1 make it possible to calculate the charge carrier lifetime τ and determine the δ value from two magnetic field inductions at which the $\frac{\Delta\alpha}{\alpha}$ values are equal. Table 2 lists the τ values calculated according to the experimental data.

Table 2. Carrier concentration, differential thermopower and charge carrier lifetime of $Pb_{1-x}Sn_xTe$ (x = 0.18) at 77 K

Sample	Carrier concentration p, 10^{17} cm^{-3}	$\frac{\Delta\alpha}{\alpha}_{max}$ B, T	τ, 10^{-12} s
3	5.2	0.058	1.65
4	2.6	0.06	0.992
5	0.52	0.08	0.24

From the relationship $\frac{\Delta\alpha(B_1)}{\alpha} = \frac{\Delta\alpha(B_2)}{\alpha}$, according to formula (1), the δ value was found to be 4.22. At known τ and δ, considering k as an adjustable parameter, according to formula (1), the field dependences of differential thermopower $\frac{\Delta\alpha}{\alpha}$ of $Pb_{0,82}Sn_{0,18}Te$ at different charge carrier concentrations were calculated; the results are shown in Fig. 2.

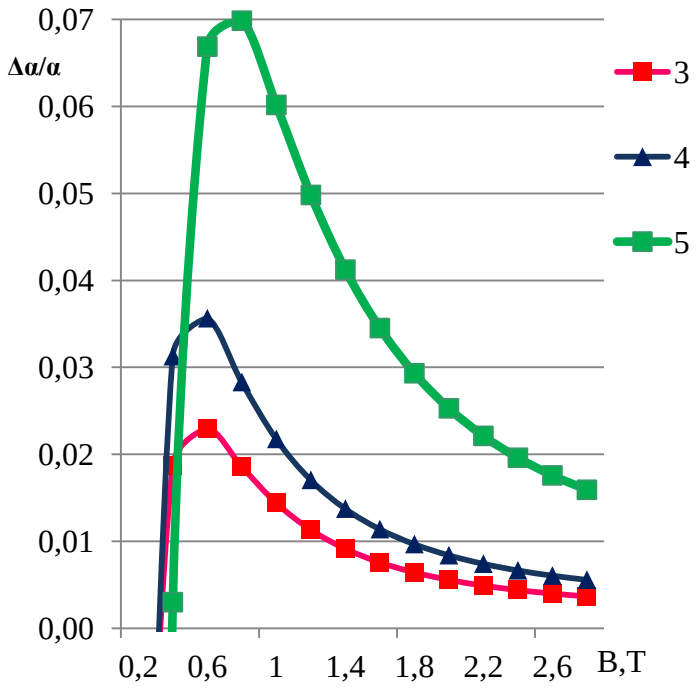

Fig. 2. Calculated field dependences of differential thermopower $\frac{\Delta\alpha}{\alpha}$ on magnetic field induction B for three $Pb_{0,82}Sn_{0,18}Te$ samples with different charge carrier concentrations. Hole concentration, cm^{-3}, 77 K, 10^{17} : *3*-5.2; *4*-2.6; *5*-0.52.

Comparison of the data in Figs. 1 and 2 shows satisfactory agreement between the experimental and calculated data.

A comprehensive study of the temperature dependence of thermoelectric power, electric

conductivity, and Hall effect and the dependence of thermoelectric power on magnetic field induction conducted using the same samples has made it possible to calculate a number of kinetic parameters of three $Pb_{1-x}Sn_xTe$ (x = 0.18) samples with different charge carrier concentrations.

Acknowledgments. The authors thank L. Ambartsumyan for her assistance in the calculations.

References

[1] D. Meglei and S. Alekseeva, Ostsillyatsii Shubnikova-de Gaaza v monokristallakh $Pb_{0,82}Sn_{0,18}Te$, Proceedings of the IV International Conference Telecomunicatii, Electronica si Informatica, 1, 321-325, Chisinau (2012).
[2] D. Meglei and S. Alekseeva, Mold. J. Phys. Sci. 13 (1–2), 20, (2014).
[3] A. I. Ansel'm, Vvedenie v teoriyu poluprovodnikov, Nauka, Moscow, 2nd. Ed, 1978.
[4] B. M. Askerov, Elektronnye yavleniya perenosa v poluprovodnikakh, Nauka, Moscow, 1985.
[5] U. Gottwick, K. Gloss, S. Horn, E. Stegiich, and A. Grewe, J. Magn. Magn. Mater. 47–48, 536, (1985).
[6] V. D. Kagan, N. A. Red'ko, N. A. Rodionov, and V. I. Pol'shin, Zh. Teor. Eksp. Fiz. 122, 377, (2002).
[7] N. A. Red'ko and V. D. Kagan, Fiz. Tverd. Tela 50, 385, (2008).

CREEP OF St–Mba–Ma POLYMERS UNDER MICROINDENTATION

R. Zhitaru[1], S. Robu[2,1], and E. Vieru[3]

[1]Institute of Applied Physics, Academy of Science of Moldova, Academiei str. 5, Chisinau, MD-2028 Republic of Moldova
[2]Moldova State University, Alexei Mateevici str. 60, Chisinau, MD-2009 Republic of Moldova
[3]Institute of Chemistry, Academy of Sciences of Moldova, Academiei str. 3, Chisinau, MD-2028 Republic of Moldova

E-mail: raisa@phys.asm.md

(Received September 29, 2015)

Abstract

The deformation, temperature and time dependences of the ST–BMA–MA copolymer have been studied; the relationship between creep and microhardness has been found. The results of ampicillin grafting onto the copolymer have been described; the effect on mechanical properties has been shown.

Studies of the mechanical properties of solid polymers make it possible to reveal the polymer deformations and provide information on micromechanical mechanisms that determine the respond of the polymer to external thermal and power impacts in different physical states. In this paper, the results of a more detailed study of the structure and physicomechanical properties of polymers is aimed at obtaining information about the conformation dynamics of molecular chains, i.e., the dynamics and kinetics of motion of molecular nanosegments capable of moving as a whole relative to other sites [1–3].

The scheme of the copolymer synthesis is shown below.

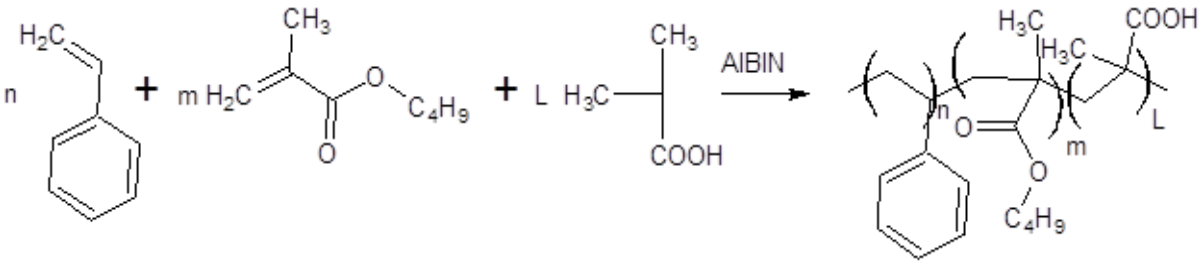

Scheme 1. Synthesis of the styrol (ST) + butyl methacrylate (BMA) + methacrylic acid (MA) copolymer.

Grafting of ampicillin onto the copolymer was conducted according to the following scheme (Scheme 2) using ethyl chloroformate.

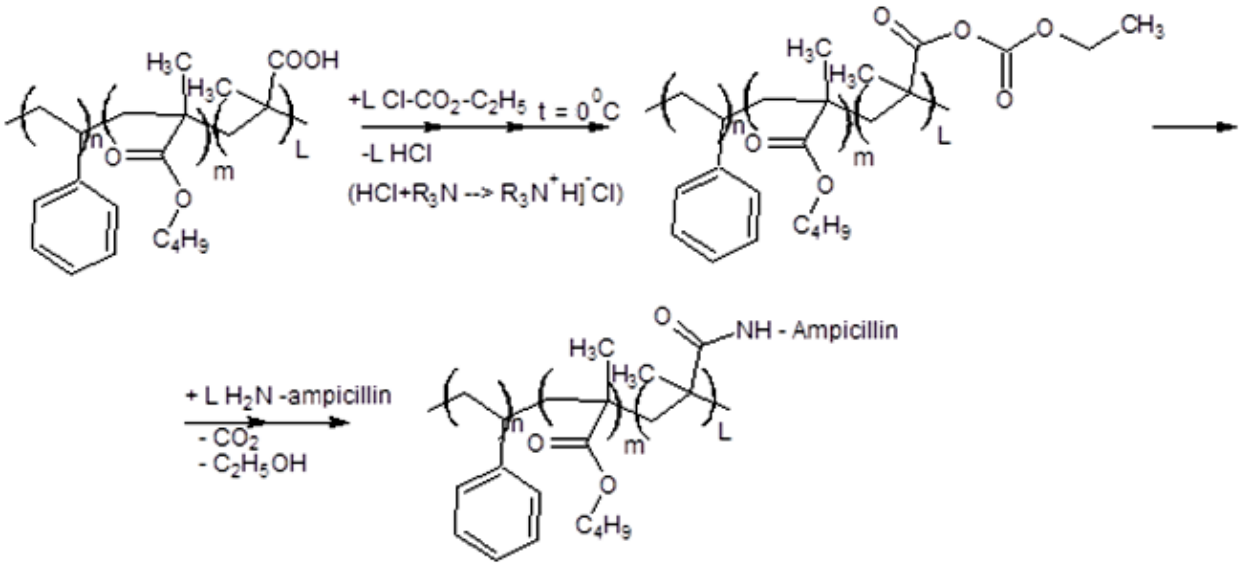

Scheme 2. Grafting of ampicillin onto the ST + BMA + MA copolymer.

Copolymers № 1M and № 2M were purified by reprecipitation. The structure of copolymer № 2M is that of copolymer № 1M grafted with 10–30% ampicillin. Copolymer films with a thickness of about 10–12 μm were prepared by solution casting on a glass substrate. The aim of this study is to show that the microindentation method can be used to examine the short and long-term creep of polymeric materials and analyze the temperature and time dependences of the creep of the polymer materials.

1. Experimental techniques and results

The stability of the studied polymer is characterized by its mechanical properties, the stability of these properties, and behavior as a function of temperature and aging time. The microhardness method (Vickers pyramid) was used as a method characterizing important physical properties [4-5]. The objects of study were amorphous copolymers № 1 composed of ST + BMA + MA (40 : 50 : 10 mol %) and № 2 with the same composition that was modified by grafting ampicillin onto COOH groups.

The ampicillin concentration was 10–30 mol %. The glass transition temperature of these polymers ranges within 80–87°C, i.e., above room temperature; therefore, the microindentation method can be used for the studies. Microhardness (H_v) was calculated by the known formula:

$$Hv = 1854\ P/d^2, \tag{1}$$

where P is the indentation load and d is the size of indenter imprint diagonal [6].

The kinetics of the creep of the polymers was investigated in a temperature range of 45–100°C.

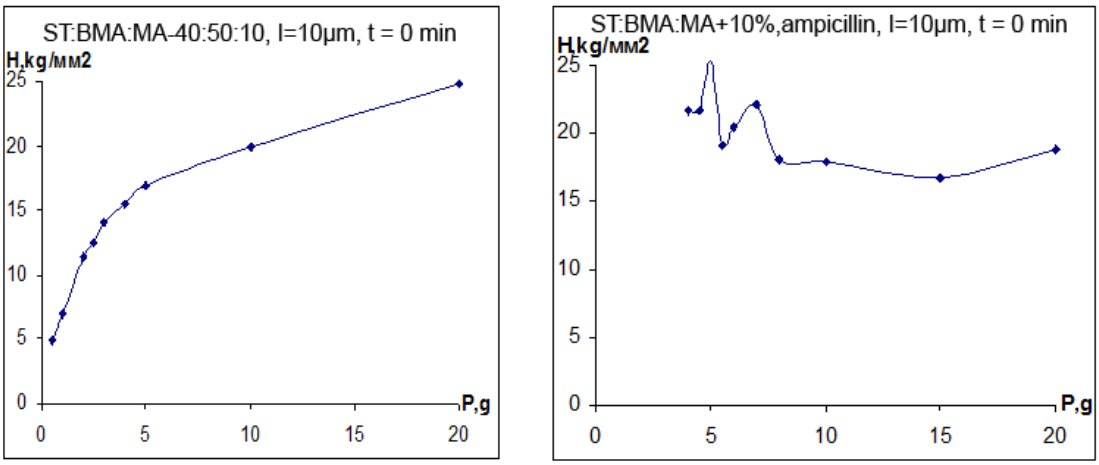

a) b)

Fig. 1. Dependence of microhardness on deforming force (indentation load). Indentation time is 2 min. Polymers with a thickness of 10 μm containing ampicillin: (a) 0 % and (b) 10%.

Figure 1 shows, for comparison, the plots of change in the microhardness versus the deforming force (penetration stress) for the polymers with and without the addition of ampicillin (Figs. 1b and 1a, respectively).

The data show that samples with the addition of ampicillin leads to a change in the behavior of the *H(P)* dependence. The difference is most pronounced in the load range of 0.05–0.1 N. An abrupt decrease in microhardness is observed in this region of loads (Fig. 1b). At the same time, in the same range of loads without additions, the microhardness uniformly increases [7–8].

However, at P = 0.05 N, the microhardness of polymers №1 is significantly less than the microhardness of polymers № 2M. The latter polymers are more reinforced in this load range; for P = 0.05 N, H_2 = 25 kg/mm^2; at the same time, for polymer №1, H_1 = 15 kg/mm^2. The effect is apparently attributed to the grafting of ampicillin onto polymer structure №1. The data are presented taking into account the effect of creep during indentation of samples №1. The changes in the microhardness suggest that the grafting of the additive onto the polymer structure contributes to strengthening of the polymer and a decrease in the creep [9–10].

The dependence of the indent size (or microhardness (H)) is determined not only by the indentation load, but also, to a considerable extent, by the duration of loading (t) at a certain constant temperature T. Changes in the microhardness duration a long-term indentation at a certain load indicate the presence of the creep of the material under the action of constant concentrated force P (Fig. 2). The zone under the imprint increases. It is this zone that determines the size of the area covered by the indenter during creep [11].

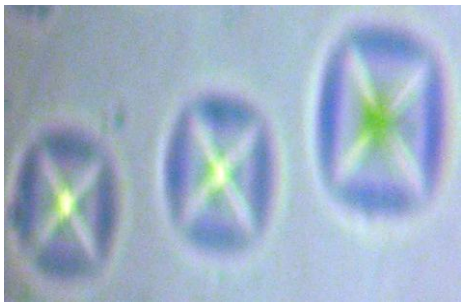

a) b) c)

Fig. 2. Image of the imprint left by the indenter during the penetration into the surface on the polymer with the addition of ampicillin at an indentation load of P = 0.05 N. Indentation time: (a) 1 min, (b) 30 days, and (c) 12 months.

Changes in the creep as a function of temperature during indentation were studied (Fig. 3).

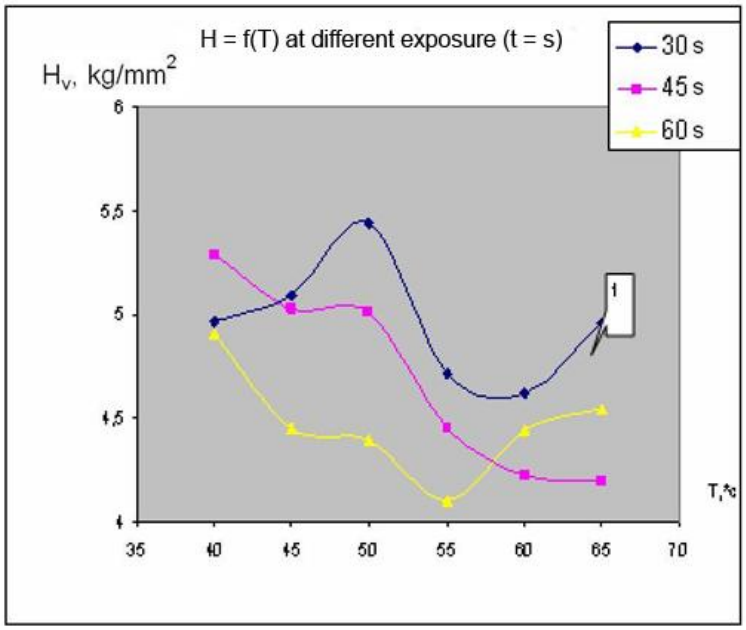

Fig. 3. Temperature dependence of the creep ($d^2 = 1854\ P/H$) at different durations (t) for polymer materials №2M. $P = 0.02$ N.

Figure 3 shows that, with an increase in the time of exposure to 60 s, the $d^2(T)$ curve is located lower than the curves in the range of 15–30 s, unlike the behavior of microhardness, as follows from formula (1) $d^2 = 1854\ P/H$. In this experiment, P is a constant value, but d^2 and H change in opposite sign to each other (Fig. 3).

With increasing temperature the creep rate increases; hence, the contribution of creep process under microindentation increases, the indent diagonal is elongated, and the microhardness decreases [12–13].

The temperature dependence of creep is clearly pronounced if we consider the cross section of the curves in Fig. 3 (along the microhardness axis) at a certain temperature. It is evident that maximum differences between the magnitudes of creep are observed in a temperature range of 45–55°C and maximal (minimal) d^2 is at 50°C.

In a range of 50–55°C, the diagonal size sharply decreases, which indicates an increase in the creep rate. The diagonal length increases, particularly for the time of 50-60 s (Fig. 4b). The diagonal of the imprint was recorded at a constant indentation load of 0.02 N.

It should also be noted that, with increasing indentation load, the $H(T)$ dependences of the sample undergoes changes. Two stages instead of one are observed. The effect is apparently attributed to the behavior of micropores in the polymer structure or to the changes in the creep in the zone under microindentation.

Figure 4 shows that the size and shape of indents have significantly changed under the action of aging time. The figure suggests the occurrence of mechanical stresses around and inside the indent, which obviously reinforce the material. The relaxation of these stresses most probably contributes to an increase in the indent size and in the diagonal size (Fig. 4b). Thus, stress relaxation and an increase in the imprint and diagonal sizes determine the creep magnitude.

Figures 4a and 4b show the imprints for the polymers containing 30 mol % of ampicillin and the deformation zones around the microindentations. Figure 4b shows the imprints on the surface of the polymer after a long rest (about 6 months at 30°C). Comparison shows that the rest increases the imprint size due to stress relaxation around the imprints (increases respectively) and is responsible for the form of the zone shown in Fig. 4b.

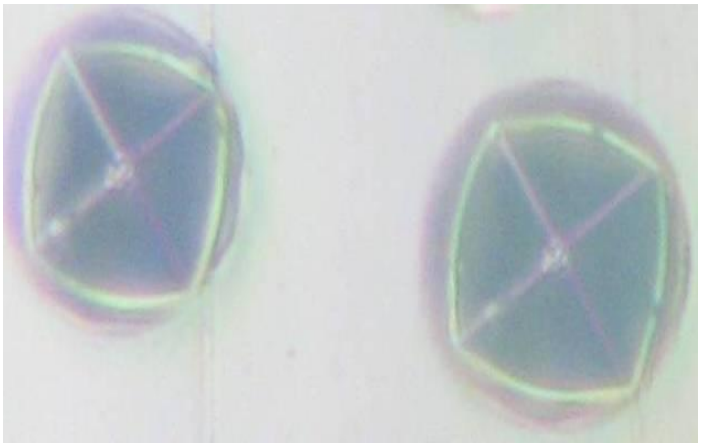

a) b)

Fig. 4. Images of the creep during the relaxation of stresses around the indents (P = 0.05 N) in the polymer materials after rest at room temperature: the view after (a) 10 days and (b) 40 days.

The role of indentation time and indentation load on the creep phenomenon was studied (Fig. 5).

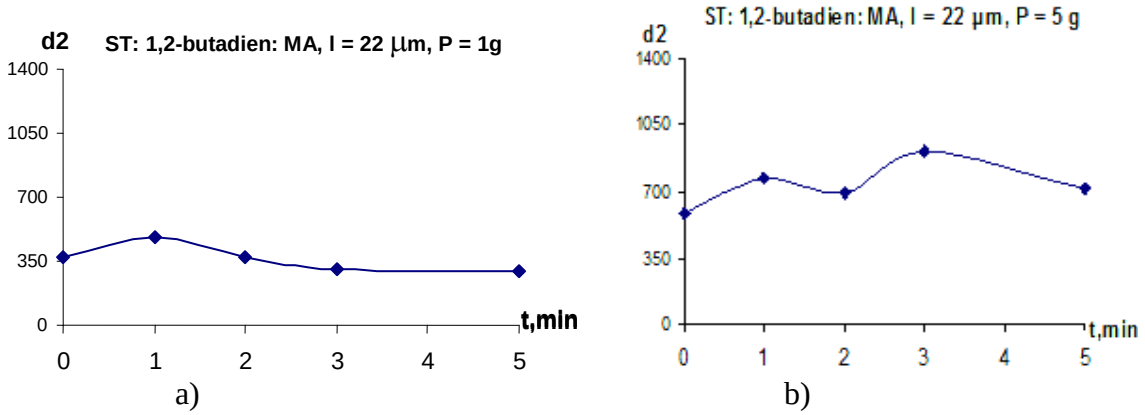

Fig. 5. Effect of indentation time (t) and indentation load (P) on the creep behavior at room temperature.

The indentation load was varied in a range of 0.05–0.6 N. The studies were conducted in a range of 0–5 min. The results show that, in the studied range of indentation time and indentation load, the creep intensity depends on the load and the stresses generated during indentation (Figs. 4, 5).

Figure 5 shows that d^2 increases from 350 to 700 units with a increase in the indentation load from P = 0.01 (Fig. 5a) to P = 0.05 N (Fig. 5b). The latter value corresponds to the

maximum indentation load of this experiment; the curve of d^2, with a load of 0.5 N, lies above the curves with a load of 0.1 N (Fig. 5). This means that, in this case, the larger the deformation zone during the microindentation of the same materials (in our case, polymer № 2M), the more significant the creep. The presence and nonuniform pattern of creep can cause a change in the imprint size and shape, particularly at large indentation loads and indentation times (Fig. 5) [15].

At an indentation load of 1 N, creep d^2 is 350 units, while at P = 5 N, the creep is 700; that is, two times higher (Fig. 6). We can conclude that, for polymer materials, the following relationship holds true: the higher the indentation strength, the more pronounced the creep.

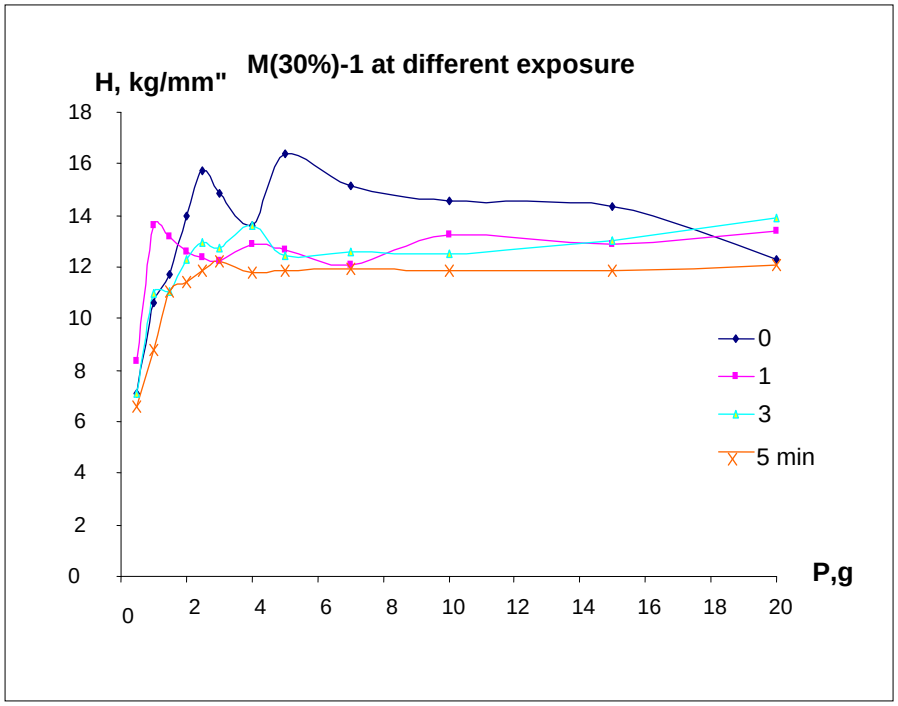

Fig. 6. *H(P)* dependence of the samples containing 30% ampicillin that were deformed at P= 0.02 N and then left to rest for different time.

The squared diagonal that symbolizes the creep and value of H (microhardness) show the inhomogeneous changes depending on the microindentation duration and the load magnitude. At light loads, the creep exhibits a weak maximum at a short time (t = 1 min) and d^2 = 350 units; over time, the creep rate achieves a maximum value not only at the one exposure time, but also at other times (t = 5 min, Fig. 6). This result suggests that the penetration of the indenter triggers additional sources of creep or leads to an increase in the creep rate.

The data of Fig. 7 also show the effect of creep on the microhardness of the polymers containing ampicillin as a supplement. The following pattern is observed: the longer the time of preliminary indentation, the lower the location of the *H(P)* curve. Most probably, this effect is attributed to the increasing effect of deformation creep in the area under indenter.

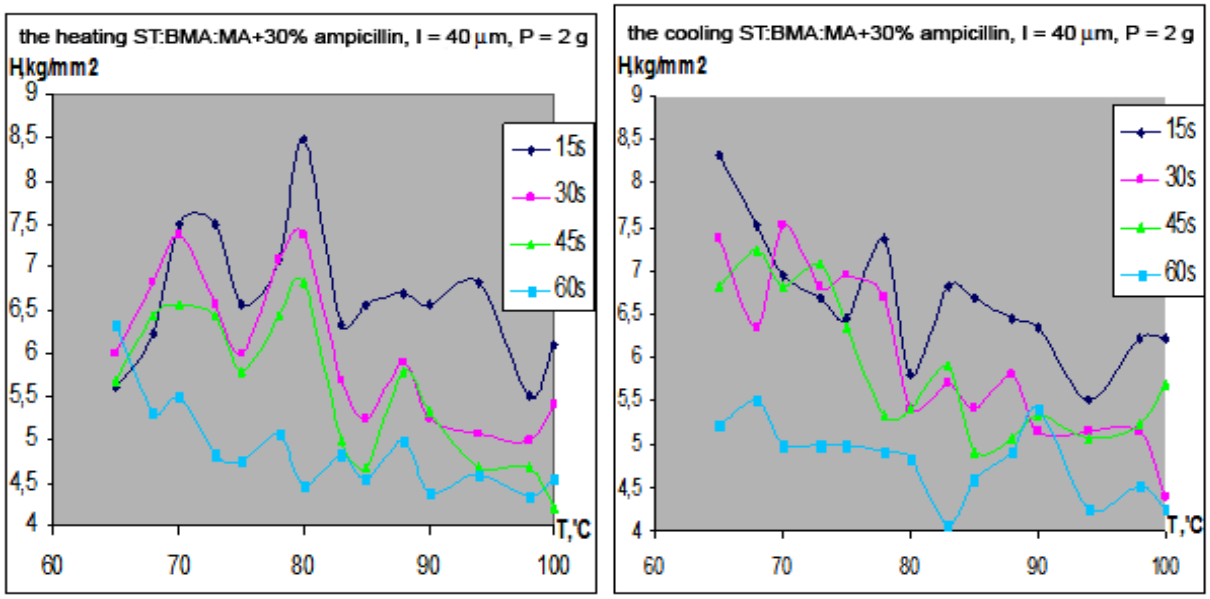

a) b)

Fig. 7. Effect of preliminary exposure at room temperature on dependence *H(T)* in the heating–cooling cycle during the microindentation of polymers 2M.

Temperature dependence *H(T)* under microindentation of polymer № 2M at different exposures (*t*) in a temperature range of 60–100°C was measured. The heating–cooling cycle was im[plemented by the microindentation method (Fig. 7).

Figure 7 shows a plot of the *H(T)* temperature dependence of microhardness in a temperature range of 60–100°C in the heating–cooling cycle of polymers 2M. There are some light areas in the region of a temperature of 80°C, where the *H* value achieves a maximum. At longer exposure times, the peaks are aligned in value; however, they remain in certain areas. This behavior is observed for the microhardness values during the heating of polymers 2M.

At T = 80°C, minima instead of maxima and a more dramatic increase in H_v with decreasing temperature are observed. At T approaching 80°C, in this region, the maximum H_v passes into a minimum. It should be noted that, during heating, a slight change in microhardness and a weakly pronounced plateau are observed in this region. During cooling, H_v slightly increases and the plateau is less pronounced (Fig. 8). This behavior can be most probably regarded as the effect of creep on the microhardness value. Apparently, these data show the role of creep in the change in microhardness H_v as a function of temperature.

It is evident that, at the same indentation load, the microhardness is lower or higher depending on the indentation time. The exposure time is different in each case. In the first case, the indentation time and, therefore, the creep are higher than in the second case. This means that, in the latter case, the creep makes a greater contribution to the indentation and, hence, to the microhardness value, which decreases owing to this process. The curves corresponding to $H_v(T)$ with a shorter exposure time are placed below the curves with longer times. The longer the exposure, the greater the decrease in H_v [15–17].

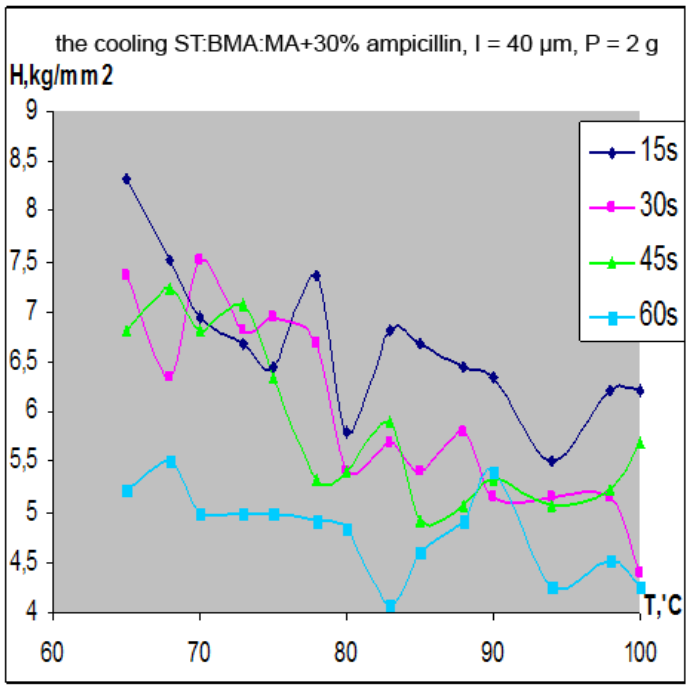

Fig. 8. Creep behavior under stress relaxation of polymer materials № 2M in a temperature range of 60–100°C during cooling.

2. Conclusions

It has been found that the Vickers microhardness measurement is one of the most common methods for testing the mechanical properties not only of crystals and solids, but also polymer materials exhibiting an elastic-plastic behavior of the creep.

The presence of the ampicillin group grafted onto the polymer chain changes the morphology of the copolymer, as evidenced by the microhardness–temperature diagrams; however, it does not significantly affect the glass transition.

References

[1] D. S. Sanditov and G. M. Bartenev, Physical Properties of Irregular Structures, Nauka, Novosibirsk, 1982, 256 p.
[2] F. J. Balta-Galleja, D. S. Sanditov, and V. P. Privalko, J. Mater. Sci. 37, 4507, (2002).
[3] M. F. Mina, Ania F. Balta-Calleja, and T. L. Asano, J. Appl. Polym. Sci. (1), 205, (2004).
[4] E. J. Pavlina and C.J. Van-Tine, J. Mater. Eng. Perfom. 17(6), 416, (2008).
[5] A. Flores and Ania F. Balta-Gallejja, J. Polymer 50(3), 729, (2009).
[6] R. Zhitaru, S. Robu, E. Vieru, and V. Filip, Proceedings of 7th Intern. Conference on Materials Science, Chisinau, Moldova, 2014, p.7.
[7] M. Stamm, Polymer Surface and Interface, Springer Verlag. Berlin, 2008.
[8] M. F. Mina, G. H. Michler, and F. J. Balta–Galleja, J. Banglades Acad. Sci. 33 (1), 15, (2009).

[9] P. Chioca, S. Robu, V. Prisacari, V. Filip, B. Spurcachiu, L. Iancu, and R. M. Grigorescu, Mat. Plast. 51, 41, (2014).
[10] G. M. Bartenev and Yu. V. Zelenev, Fizika i Mekhanika Polimerov, Vyisshaya Shkola, Moscow, 1983, 94 p.
[11] P. P. Kusy, J. Q. Witley, and S. Kalachandra, Polymer 42 (6), 2586, (2001).
[12] J. L. Bucaille, F. E. Feider, and G. J. Hochstetter, Mater Sci., 37 (18), 3999, (2002).
[13] A. Pusza and K. Michalik, Archives of Nater..Sci.Eng 28(8), 467, (2007).
[14] Y. T. Cheng and C. M. Cheng, Mater. Sci Eng . 44, 87, (2004).
[15] V. Rubanik, R.P. Zhitaru, N.A. Palistrant, et al., Proceedings of the Int. Symposium, Vitebsk, 2009, p. 93.
[16] S. Robu, R. Jitaru, G. Dragalina, E. Vieru, V. Filip, Studia Universitatis Moldaviae, Chisinau № 1(7), 2014, p.161.
[17] S. Robu, R. Zhitaru, E. Vieru, V. Filip, N. Palistrant, A. Meshalkin, P. Chioca, and L. Iancu, Mater. Plast. 51 (2), 141, (2014).

CRYSTALLINE STRUCTURE AND PHOTOLUMINESCENCE OF GaSe-CdSe NANOCOMPOSITE

Liliana Dmitroglo[1], Igor Evtodiev[1,2], Iuliana Caraman[3], Valeriu Kantser[1,2], Dumitru Untila[1,2*], Marius Stamate[3], Petru Gashin[1]

[1] Moldova State University, A. Mateevici, 60, MD-2009, Chisinau, Republic of Moldova.
[2] Institute of the Electronic Engineering and Nanotechnologies, Academy of Sciences of Moldova, Academiei, 3/3, MD-2028, Chisinau, Republic of Moldova.
[3] Vasile Alecsandri University of Bacau, Calea Marasesti 157, Bacau, 600115, Romania
E-mail: dumitru.untila@yahoo.com

(Received November 04, 2015)

Abstract

A material consisting of CdSe and GaSe crystallites with average dimensions of 34 nm and 30 nm respectively was obtained by heat treatment at 753K and 853K of GaSe single crystal plates in Cd vapors during 24 hours. As a result of Cd atoms interaction with Se atoms CdSe layers are formed both onto outer surface and at interface of layered Se-Ga-Ga-Se packages. CdSe crystallites on the surface grow in the form of plates along C_6 crystallographic axis. Photoluminescence spectra of the composite, at 78K and 300K, contain predominant bands from the luminescent emission of GaSe and CdSe components.

1. Introduction

Layered III−VI compounds represent an emerging class of electronic materials, composed of elementary Chalcogen-Metal-Metal-Chalcogen layered packages. Atomic layers of GaSe consist of 2 monoatomic sheets of Ga sandwiched between 2 monoatomic sheets of Se. The ionic-covalent (predominant) bonding inside a package is much stronger than forces between packages, of Van der Waals type, which determines its specific quasi-*2D* structure and marked anisotropy of physical properties [1].

GaSe single crystal is an optically transparent material in a large wavelength range (0.6−28 μm) [2, 3], exhibits a *p*-type electric conductivity [4] and a band gap of ~ 2.0 eV [5]. These properties along with its high structural anisotropy determine a wide range of applications, including photoelectrical devices [6], linear and nonlinear optics, from electro-optical modulators to THz band generators/receivers [7].

The range of physical properties (suitable for applications) of layered III−VI compounds, in particular of GaSe, can be extended through doping [8] and intercalation [9]. Groups I, II and IV doping elements (Cu, Cd, Zn, Sn) and lanthanide impurities (Gd, Er) [10, 11] lead to an increase in hole concentration from 10^{14} cm^{-3} to 10^{17} cm^{-3} [12, 13].

The characteristic feature of III−VI compounds doping consists of the fact that at low concentrations, impurity atoms liquidate the structural defects present in metal Ga, In) sublattice, while for higher doping concentrations, the exceeding impurity atoms localize mainly between *Se* planes of Se-Ga-Ga-Se packages, producing new hydrogen bonds between Se atoms belonging to neighboring packages. Besides traditional doping mechanisms, substitution and interstitial, impurity insertion (atomic and molecular ions) into the interlayer space (intercalation) is typical

for the layered III–VI materials. Presence of impurity intercalated atoms may lead to the formation of novel nano-composites with completely different characteristics and perfectly ordered structures that exhibit atomically flat surfaces, with unusual, controllable (anisotropic) physical properties [9, 14].

In present work structural, morphological and photoluminescence (PL) characteristics of the micro-composite obtained by Cd intercalation (from vapor phase) of GaSe single crystals are examined.

2. Experimental procedures

The starting GaSe single crystals have been grown by Bridgman-Stockbarger technique, from their component elements (all of 5N purity) in a three-zone vertical furnace. From GaSe ingots, plan-parallel plates, of thickness between 60 μm and 300 μm have been split along the *cleavage* planes, from which rectangular samples with surface area of 0.5−2 cm^2 have been cut. Hole concentration in *p*-type selected samples was of 2.5×10^{14} cm^{-3}. Single crystal plates were put, together with 2.5 mg/cm^3 Cd (5N) metal, in quartz ampoules which were pumped down to 5×10^{-5} Torr and tight closed, before being placed inside an electric oven with stabilized temperature in the range of 573−873K, for heat treatment. Samples annealing was performed at temperatures from 753K to 830K, for 12 and 24 h.

The chemical composition of the primary samples and of the intercalated materials has been studied by X-ray diffraction (XRD, CuK_α radiation, wavelength $\lambda_{CuK\alpha}$ = 0.154182 nm) with a DRON-4 apparatus, as well as by micro-Raman scattering experiments.

Surface morphology of lamellar samples and the interface between elementary Se-Ga-Ga-Se packages were analyzed by means of Scanning Electron Microscopy (SEM, Quanta 200 system) and Atomic Force Microscopy (AFM, NT-MDT SOLVER PRO-M equipment) techniques. The PL measurements were carried out in the temperature range of 78−300K and PL excitation was performed by using the second harmonic of a *Nd:YAG* laser (λ=532 nm), with a power density up to 0.5 W/cm^2.

3. Experimental results and interpretations

3.1 Chemical composition of the studied samples

The composition of the material obtained by Cd intercalation of GaSe lamellas was analyzed by X-ray diffraction. The XRD pattern of primary GaSe single crystal samples is shown in Fig. 1.

Parameters of the hexagonal lattice of GaSe single crystals, calculated by using 2θ positions of (202) and (0012) XRD lines, were found to be a = 3.756 Å and c = 15.863 Å.

As can be inferred from XRD patterns presented in Fig. 2 and the Table 1, by Cd intercalation of GaSe lamellas at temperature of 753K, a composite consisting of CdSe and GaSe micro-crystals is formed (Figs. 5 and 6). Peak intensity analysis of XRD patterns shows that CdSe phase (microcrystals) is predominant. At the same time one can mention that CdSe crystallites are formed both on the surfaces of GaSe lamellas and at the interfaces between layered packages.

The XRD pattern of the primary GaSe single crystals displays narrow lines, characteristic for the scattering from micro- and macro-crystallites in the whole 2θ measured range, but the XRD reflections of CdSe-GaSe composite exhibit a wider contour, which is characteristic to the crystallites in sub-micrometer and nanometer range sizes. Crystallite mean size (d) was estimated

appealing to Debye-Scherrer's formula [15]:

$$d = \frac{0.94\lambda}{B\cos\theta}, \tag{1}$$

where λ is the X-ray wavelength ($\lambda_{CuK\alpha}$ = 1.54182 nm), B - angular full width at half maximum (FWHM) intensity, and θ - Bragg diffraction angle.

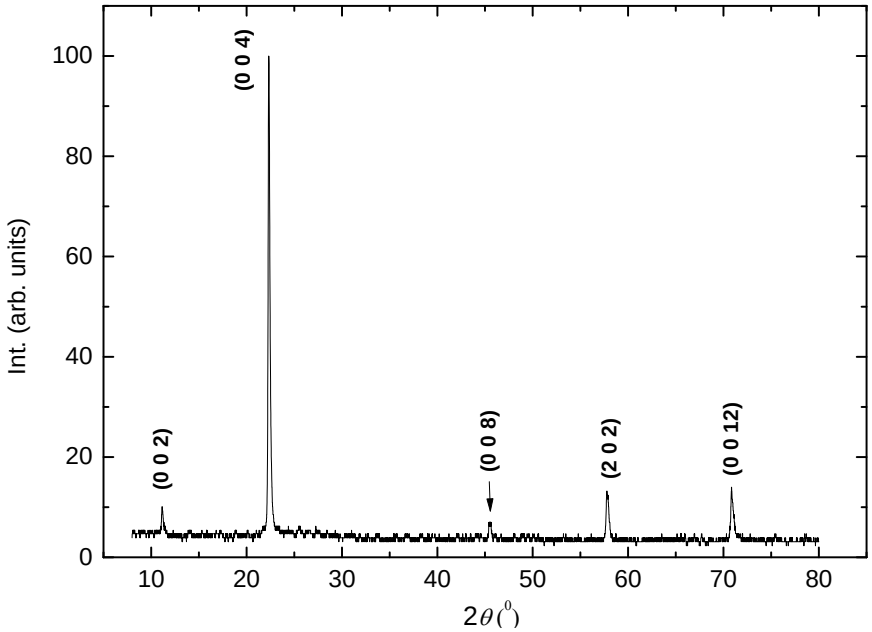

Fig. 1. XRD pattern of GaSe single crystals.

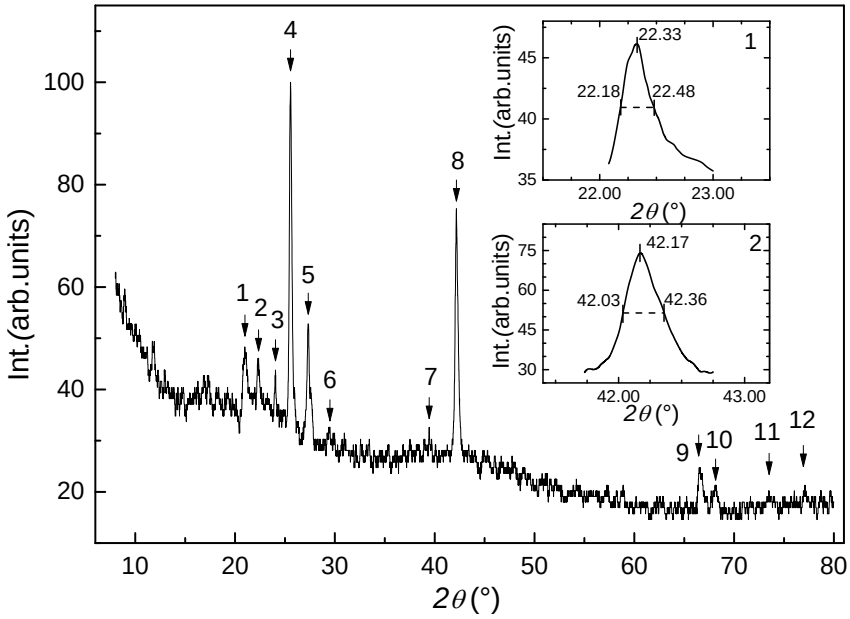

Fig. 2. XRD pattern of GaSe lamella intercalated with Cd at temperature of 753K. Inset 1 – XRD peak profile for the (006) line at $2\theta = 22.33°$ (hexagonal ε-GaSe lattice). Inset 2 - XRD peak profile for the (220) line at $2\theta = 42.17°$ (wurtzite-type CdSe lattice).

Table 1. Structural parameters of GaSe and CdSe components from composite

Nr.	Experimental values			ICDD-JCPDS cards			
	2θ (°)	*Iht-f*	Sample	PDF	2θ (°)	*Int-f*	*h k l*
1	20.99	47.44					
2	22.33	45.43	GaSe	81-1971	22.338	99.3	0 0 6
3	24.05	43.8					
4	25.56	100	CdSe	65-2891	25.480	99.9	1 1 1
5	27.33	52.8	GaSe	37-0931	27.623	4	1 0 0
6	29.50	32.24	CdSe	65-2891	29.505	40	2 2 0
7	39.45	32.6	δ-GaSe	29-0628	39.479	20	1 0 10
8	42.17	75.3	CdSe	19-0191	42.044	55	2 2 0
9	66.5	24.7	CdSe	02-0330	66.280	30	2 1 0
10	68.14	21.3	GaSe	79-6611	68.499	1	1 1 16
11	73.5	20.00	CdSe	81-1911	73.511	26	0 0 17
12	76.93	20.00	CdSe	19-0191	76.851	4	4 2 2

Using (006) XRD line located at $2\theta = 22.33°$ (FWHM=5.18×10^{-3} rad) (Fig. 2, Inset 1), of ε-GaSe hexagonal lattice and (220) line at $2\theta = 42.17°$ (FWHM=5.72×10^{-3} rad) (Fig. 2, Inset 2), of CdSe wurtzite-type lattice, average crystallite sizes of ~ 30 nm and ~ 34 nm, respectively, have been found.

3.2 Se-Ga-Ga-Se packages surface and interface morphology

The structural features of layered GaSe compound allow facile crystal cleavage in plan-parallel single crystalline lamellas, atomically smooth and optically homogeneous, of quite different thicknesses, ranging from millimeter down to nanometric size [16]. As was mentioned above, the valence bonds in the outer atomic layer of GaSe lamellas are practically closed, which leads to a low surface state concentration. According to estimates made in [17], the surface state density does not exceed 10^{10} cm^{-2}. Usually, the surface states behave as adsorption centers for ambient atmospheric atoms (molecules), with the formation of Ga and Se oxide nanoislands [18]. SEM images of GaSe surface and of lamellae interface, kept in normal ambient conditions (temperature, humidity, pressure) for over 3 years, are given in Figs.3 and 4, respectively.

If we admit the surface defect based mechanism of nanoislands formation [i.e. formation of the oxide nanoislands (Fig. 3) is mainly due to surface defects of GaSe, which act as adsorption centres for ambient particles], surface state density of cleaved GaSe lamellas can be estimated as $\sim 2\times 10^{10}$ cm^{-2}. One can mention that this value is in good agreement with the estimates made in Ref. [16, 17], which reported surface states densities of ~ 10^{10} cm^{-2} and less.

Therefore, as a result of long time preservation of GaSe plates in normal atmosphere, a nanosized oxide layer (nanoislands), composed of Ga_2O_3, SeO_2, SeO_3, $Ga_2O_3(SeO_4)^{2-}$, $Ga_2(SeO_4)_3$ and gallium selenide hydrate in [19, 20].

At the same time, the interface nanostructuring occurs (Fig. 4), but the size of nanostructuring centers is much smaller in comparison with that for the outer GaSe surface.

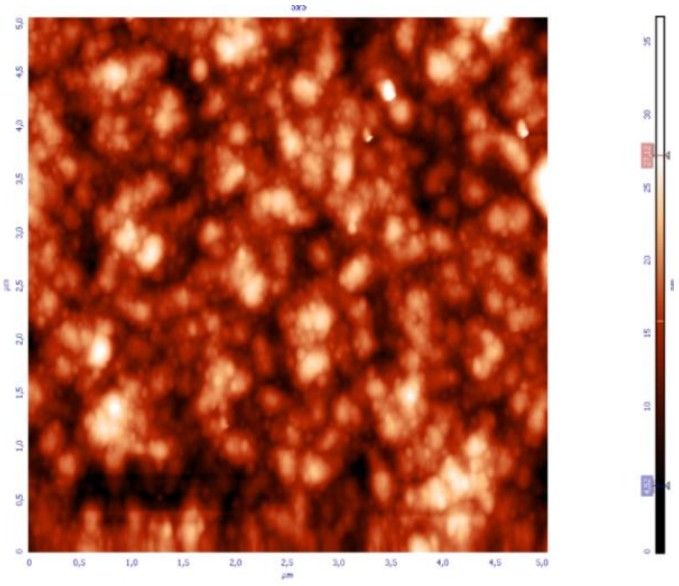

Fig. 3. SEM image of GaSe surface, kept in normal atmosphere.

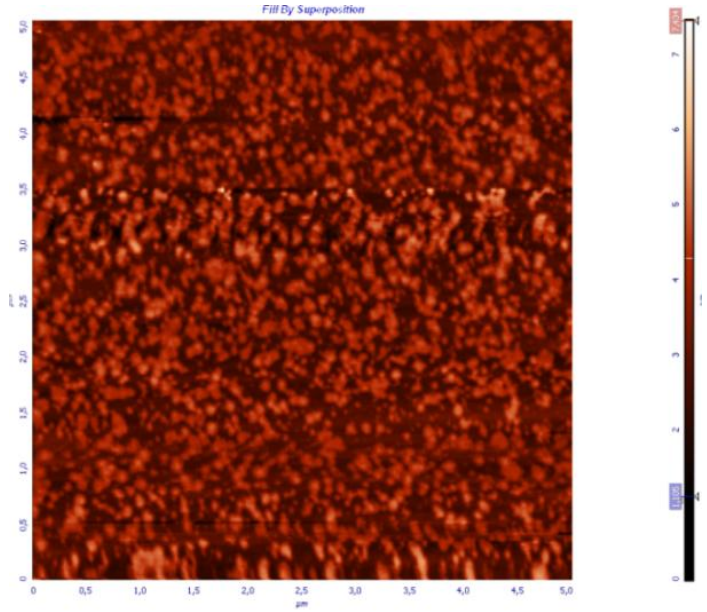

Fig. 4. SEM images of GaSe lamellae interface, kept in normal atmosphere.

In spite the low density of adsorption centers on the surface of GaSe single crystal plates, as a result of Cd-vapor heat treatment at temperatures in the range of 753−833K, formation of variable shape and size microclusters takes place, both on the outer surface and at the interfaces of elementary Se-Ga-Ga-Se packages.

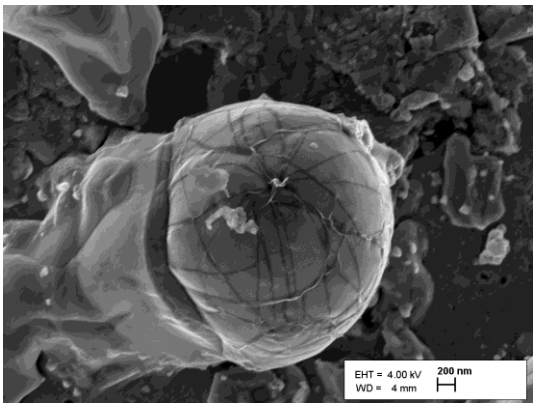

Fig. 5. AFM image of the GaSe plate surface, subjected to a heat treatment at 753K, for 24 hours, in the Cd vapors.

As can be seen in Fig. 5, the microclusters on the GaSe surface grow preponderantly in layers along C_6 crystallographic axis, while at the interface between layered packages flat clusters form (Fig. 6).

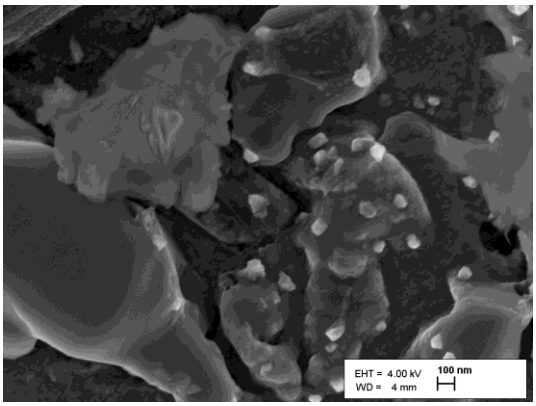

Fig. 6. AFM image of the GaSe plate interface, subjected to heat treatment at 753K, for 24 hours, in Cd vapors.

Nanosized clusters (drops-white spots) can be seen (Fig. 6) on the surface of larger formations, that are produced by Ga metal condensation, which is released from elementary packages as a result of the formation of new compositions (in particular, of CdSe nanoparticles).

3.3 The photoluminescence of non-intercalated and Cd intercalated GaSe lamella

As was demonstrated higher, in the van der Waals crack of GaSe crystal by cadmium intercalation from vapour phase at 833K a composite containing CdSe and GaSe micro- and nano- crystallites is obtained. This material is a radiation source in the red spectrum region when being excited with radiation from absorption band of its components (GaSe and CdSe). At first the PL spectra of GaSe and CdSe in micro- and poly- crystals were analysed.

The PL spectra of CdSe single crystals (Fig. 7), at chamber temperature (a) and at 80K (b), represent *a* band with asymmetric contour and maxima at energy 1.720 eV and 1.787 eV respectively. Whereas the CdSe bandgap at 78K is ~1.84 eV [21] the band with maximum at

energy 1.787 eV is associated to free excitons recombination with holes from the acceptor level of energy E_V + 0.038 eV.

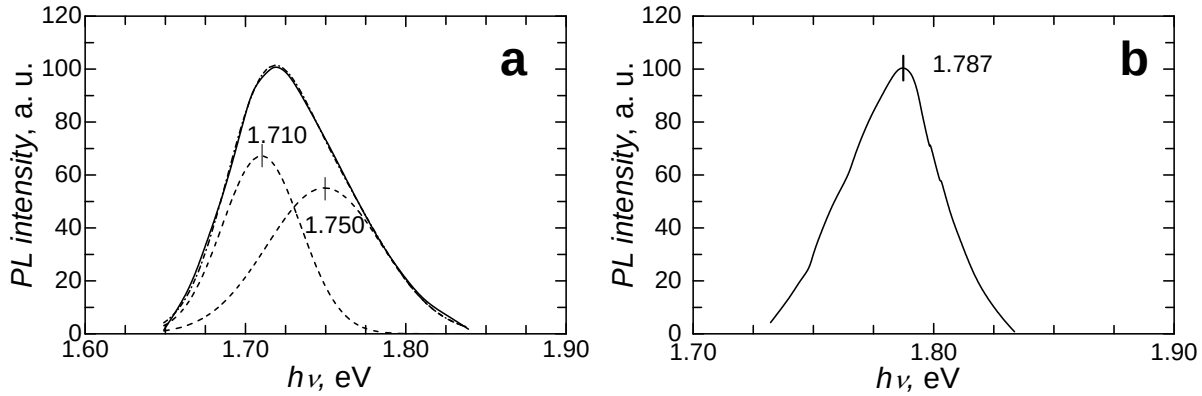

Fig. 7. The PL spectra of CdSe compound at 300K (a) and 80K (b).

The PL spectrum of GaSe single crystals at 80K (Fig. 8), used for GaSe-CdSe composites obtaining, contains at least four bands (A-D) with maxima at energies of 2.091 eV (A), 2.070 eV (B), 2.049 eV (C) and 1.910 eV (D).

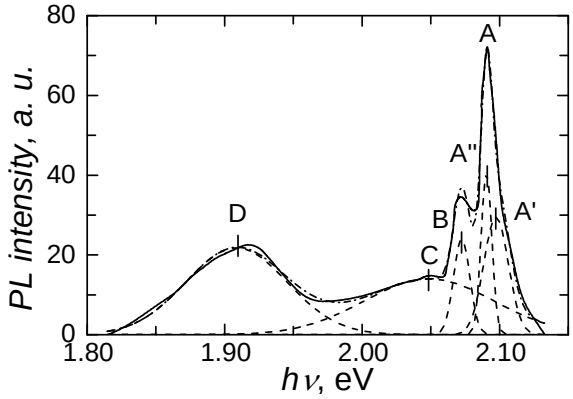

Fig. 8. The PL spectrum of GaSe crystals at 80K.

The band A is well described by two bands with maxima at energies of 2.097 eV (A') and 2.091 eV (A"). The band A' is interpreted as luminescent emission as a result of direct excitons' annihilation [22]. The band A" can be interpreted as radiative emission of excitons localized at neutral acceptor centres with bond energy of ~6 meV [23]. The band B can be considered as first phonon repetition of A" band with phonon emission of energy 19 meV. The band C, with maximum at energy 2.049 eV, well correlates with indirect excitons' energy at 80K and can be considered as luminescent emission of localized indirect excitons [24]. The band D is well studied in [22] where is interpreted as donor-acceptor emission. The own structural defects form in the bandgap of GaSe compound an acceptor level of energy E_V + 0.152 eV. The levels of energy E_C – 0.056 eV are formed in GaSe by Ga impurities [22] that are present in GaSe as

uncontrollable impurities.

The PL spectrum of CdSe-GaSe composite at chamber temperature is composed by a wide band with maximum at energy 1.775 eV (Fig. 9). This band contour can be well decomposed in three Gauss curves with maxima at 1.806 eV, 1.750 eV and 1.691 eV. As result of formation of CdSe crystallites free Ga atoms are obtained. At 833K these atoms are doping the both GaSe and CdSe crystallites. The PL band with maximum at 1.750 eV is also present in the PL spectrum of CdSe single crystals (Fig. 7) and could by caused by radiative band-band recombination. The band 1.691 eV is determined most probably by the Ga and Cd impurities present in CdSe crystallites.

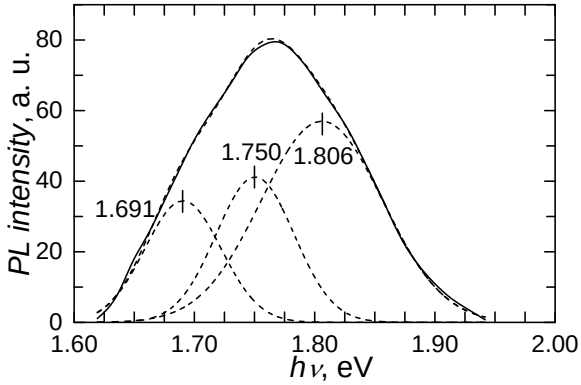

Fig. 9. The PL spectrum, at 300K, of GaSe-CdSe composite obtained by heat treatment of GaSe plates in Cd vapors at 833K for 20 hours.

The temperature decrease from 300K (Fig. 9) to 80K (Fig. 10) leads to PL band increasing in intensity and shifting to higher energies.

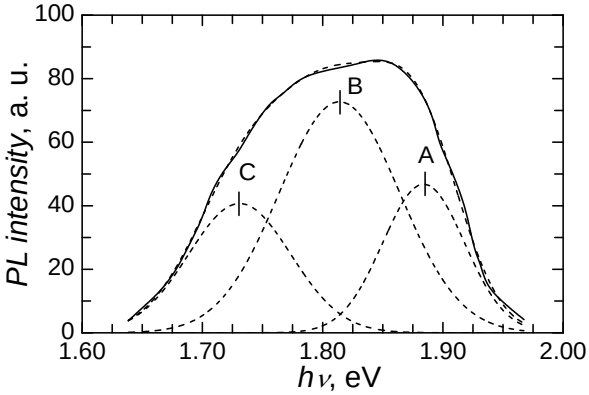

Fig. 10. The PL spectrum, at 80K, of GaSe-CdSe composite obtained by heat treatment of GaSe plates in Cd vapors at 833K for 20 hours.

As we can observe from Fig.10 this band contour decomposes well in three Gauss curves with maxima at energies 1.884 eV (A), 1.814 eV (B) and 1.781 eV (C). As can be observed by comparison of Fig.10 and Fig.8 these three bands are shifted to lowest energies toward PL bands of GaSe compound. So these bands could be associated to luminescent emission in CdSe crystallites from composite. We mention that this band contour is not modified at PL excitation

with radiation of He-Ne laser. The energy of this radiation is 1.96 eV and it is lowest than bandgap of GaSe compound which at 80K is equal to 2.104 eV. The bandgap of CdSe crystallites is equal to 1.84 eV [21]. The fundamental absorption edge band of CdSe crystallites at 80K is formed by the band of excitons in the state n = 1 which bond energy is ~16 meV [25]. The band B could be interpreted as radiative emission of localized excitons with the bond energy of electron to ionized donor equal with ~11 meV.

The CdSe layer from the surface has *n* type conductivity determined by the presence of Se vacancies. The Ga atoms also form a donor level with the energy much smaller than the energy of deep acceptors generated by the Se atoms (energy 0.6 eV [26]). Taking into account these energetic parameters, we can admit that the band C has a donor-acceptor nature with the participation of donors formed by the atoms of Ga impurity, diffused in CdSe crystallites. The band A (1.884 eV) is shifted by ~43 meV inside the absorption band of CdSe compound.

The bands with maxima at 1.806 eV (at T = 300K) and 1.884 eV (at T = 80K) have their maxima localized at energies higher than bandgap of CdSe compound by 66 meV and 44 meV respectively.

It is well known [27; 28] that the PL spectra of CdSe nanoparticles are shifted to higher energies against the PL spectra of single crystals and polycrystalline thin structures. The diameter *D* of nanoparticles according to the theoretical approach developed by Brus [29] is given by the formula:

$$\Delta E = \frac{\hbar^2 \pi^2}{2D^2}\left[\frac{1}{m_e} + \frac{1}{m_h}\right] - \frac{1.8e^2}{\varepsilon \varepsilon_0 D} \qquad (2)$$

where m_e and m_h are the effective masses of electrons and holes, which for CdSe are 0.13 m_0 and 0.45 m_0 respectively [30], ε – static dielectric permittivity equal with 9.6, $\varepsilon_0 = 8.85 \cdot 10^{-12} F/m$.

For antiStockes shift of PL band, at T = 300K, equal with ΔE = 66 meV we obtained an average diameter of CdSe nanoparticles of ~0.7 μm. For ΔE = 44 meV, at T = 80K, the average diameter of CdSe nanoparticles is ~0.85 μm. We mention that the average dimensions of crystallites from the sample's outer surface, calculated using formula (1) have the same order of magnitude as dimensions of inhomogeneities presented in the AFM images.

4. Conclusions

- by GaSe lamella intercalation with Cd from vapor phase was obtained the GaSe-CdSe composite consisting of CdSe and GaSe micro-crystallites and condensed CdSe nanoparticles. The defects from the GaSe lamella surface serve as centres of CdSe crystallites formation. These defects' density is about $10^{10}\ cm^{-2}$.
- the CdSe micro-crystallites grow prevalent in the perpendicular direction on to GaSe lamella (0 0 0 1) natural surface.
- the PL spectrum of CdSe-GaSe composite obtained by heat treatment in Cd vapors, at 833K, for 24 hours, at 300K contains the band-band recombination emission bands, since at 80K temperature – annihilation of localized excitons in CdSe crystallites.
- the antiStockes luminescence at 300K and 80K is determined by the reduced dimensionality (~0.8 μm) of crystallites from the composite.

Acknowledgments. The authors acknowledge the support of Institutional Project 15.817.02.34A „*Optoelectronic and optical information registration devices obtained on multifunctional semiconductor materials and nano-layered structures*" (Moldova State University).

References

[1] F. Levi (ed.), Crystallography and crystall chemistry of materials with layered structures, D. Reidel Publishing Company, Dodrecht/Holland; Boston/USA, 1976.
[2] V. G. Voevodin, O. V. Voevodina, S. A. Bereznaya, Z. V. Korotchenko, A. N. Morozov, S. Yu. Sarkisov, N.C. Fernelius, J.T.Goldstein. Opt. Mater. 26, 495, (2004).
[3] K. L. Vodopyanov, L. A. Kulevskii. Opt. Commun. 118, 375-378, (1995).
[4] Y. Depeursinge, C. Depeursinge. J. Phys. C: Solid State Phys. 12, 4851, (1979).
[5] R. Le Toullec, N. Piccioli, J. C. Chervin. Phys. Rev. B: Condens. Matter 22, 6162, (1980).
[6] A. G. Kyazym-zade, A. A. Agaeva, V. M. Salmanov, A. G. Mokhtari. Tech. Phys. 52, 1611, (2007).
[7] L. Yan-Zhao, W. Xin-Bing, M. Liang, Z. Du-Luo, C. Zu-Hai. Chin. Phys. Lett. 28, 034201, (2011).
[8] A. Kuhn, R. Chevalier, A. Rimsky. Acta Cryst. B 31, 2841, (1975).
[9] C. M. Julien. Mater. Sci. Eng., R 40, 47, (2003).
[10] B. Gurbulak, M. Yildirim, S. Tuzemen. J. Appl. Phys. 83, 2030, (1998).
[11] Y. K. Hsu, C. S. Chang, W.F. Hsieh. Jpn. J. Appl. Phys. 42, 4222, (2003).
[12] S. Shigetomi, T. Ikari, H. Nakashima. J. Appl. Phys. 73, 4686, (1993).
[13] S. Shigetomi, T. Ikari, H. Nakashima. J. Appl. Phys. 80, 4779, (1996).
[14] A. P. Bakhtinov, V. N. Vodopyanov, Z. D. Kovalyuk, V. V. Netyaga, D. Yu. Konoplyanko. J. Semicond. 45, 338, (2011).
[15] A. L. Patterson. Phys. Rev. 56, 978, (1939).
[16] J. P. Guesdon, D. Kobbi, C. Julien, M. Balkanski. Phys. Status Solidi A 102, 327, (1987).
[17] D. Untila, V. Kantser, M. Caraman, I. Evtodiev, L. Leontie, L. Dmitroglo. Phys. Status Solidi C 12, 65, (2015).
[18] O. A. Balitskii. Mater. Lett. 60, 594, (2006).
[19] O. A. Balitskii, V. P. Savchyn, V. O. Yukhymchuk. Semicond. Sci. Technol. 17, L1, (2002).
[20] S. I. Drapak, S. V. Gavrylyuk, Z. D. Kovalyuk, O. S. Lytvyn. J. Semicond. 42, 414, (2008).
[21] M. Cardona, G. Harbeke. Phys. Rev. 137, A1467, (1965).
[22] V. Capozzi, A. Minafra. J. Phys. C: Solid State Phys. 14, 4335, (1981).
[23] S. Shigetomi, T. Ikari. J. Appl. Phys. 94, 5399, (2003).
[24] C.H. Chung, S. R. Hahn, H. L. Park, W. T. Kim, S. I. Lee. J. Lumin. 40, 405, (1988).
[25] M. Aven, J. S. Prener (Auth.), H. H. Woodbury (ed.), Physics and Chemistry of II-VI Compounds, North-Holland Publishing Company, Amsterdam, 1967.
[26] K. L. Chopra, S. R. Das. Thin Film Solar Cells. Plenum Press, New York, 1983.
[27] G. Hodes, A. Albu-Yaron, F. Decker, P. Motisuke. Phys. Rev. B: Condens. Matter 36, 4215, (1987).
[28] E. M. Boatman, G. C. Lisensky, K. J. Nordell. J. Chem. Educ. 82, 1697, (2005).
[29] L. Brus. J. Phys. Chem. 90, 2555, (1986).
[30] W. Seith, O. Kubaschewski. Z. Elektrochem. Angew. Phys. Chem. 43, 743, (1937).

SYNTHESIS AND BIOLOGICAL APPLICATION OF MAGNETITE NANOPARTICLES

T. Gutul[1], I. Rastemisina[2], O. Postolachi[2], A. Nicorici[1], D. Dvornikov[1], and P. Petrenco[3]

[1]*Institute of Electronic Engineering and Nanotechnologies 'D.Ghitu', Academy of Sciences of Moldova, Academiei str. 3/3, Chisinau, MD-2028 Republic of Moldova*
E-mail: tatiana.g52@mail.ru

[2]*Institute of Microbiology and Biotechnology, Academy of Sciences of Moldova, Academiei str. 1, Chisinau, MD-2028 Republic of Moldova*
E-mail: rastimesina@gmail.com

[3]*Institute of Applied Physics, Academy of Sciences of Moldova, Academiei str. 5, Chisinau, MD-2028 Republic of Moldova*
E-mail: peter.petrenco@phys.asm.md

(Received December 3, 2015)

Abstract

Magnetite (Fe_3O_4) nanoparticles were prepared by chemical coprecipitation from a ferrous/ferric mixed salt-solution in the presence of PVP used as a stabilizer and without it. The resulting magnetite nanoparticles were characterized by X-ray powder diffraction (XRD) analysis and scanning electron microscopy (SEM). Aqueous colloidal solutions of the prepared nanoparticles were used in the biotest.

The biotest was conducted to determine the degree of growth of wheat seeds in the contaminated soil treated with nanoparticles Fe_3O_4/PVP and nano Fe_3O_4. The maximum stimulatory effect on the growth of wheat seedlings in a soil subjected to long-term contamination with pesticides, mostly trifluralin, was observed in the case of incubation of the soil with a solution of Fe_3O_4/PVP nanoparticles at a concentration of 50 mg/kg of dry soil for 4 days; the effect was evident from an increase in the length of both the roots (by 165.0%) and the seedlings (by 141.0%) relative to the reference sample.

1. Introduction

Since the contamination and degradation of the environment cannot be completely hindered, the development and assimilation of effective technologies for the remediation and reclamation of soils and lands is an objective necessity.

A rational approach to this issue is based on the optimum use of natural processes of self-purification and self-regeneration, such as bioremediation, and novel processing techniques.

In recent years, many studies focused on the decomposition of pesticides in aqueous media and soils using nanoparticles as the active component have been reported. Much attention has been paid to the iron-containing nanoparticles (magnetite (Fe_3O_4), goethite FeO(OH), hematite α-Fe_2O_3, and zero-valent iron Fe^0) that exhibit pronounced redox properties. It has been proposed to use these nanoparticles for the remediation of both organochlorine pesticides and phosphorus-containing pesticides. Studies on nitro pesticides, which include trifluralin, are scarce

and mostly focused on the degradation of the pesticides in water [1–3].

Trifluralin is an herbicide (toxic group III) characterized by long-term persistence in soil. It has the ability to accumulate in the soil and hardly undergoes biodegradation. According to the "National Program for Monitoring Pesticide Residues in Soil and Water," the maximum trifluralin residues in the soils of Moldova are 0.1 mg/kg of soil. Thus, the search for methods for the purification of soils from trifluralin is an urgent problem.

The aim of this study is to synthesize magnetite nanoparticles without stabilizer (nanoFe_3O_4) and nanoparticles stabilized with biocompatible polymer poly-*N*-vinylpyrrolidone (nanoFe_3O_4/PVP) and examine the effect of the iron nanoparticles on wheat seed germination against the background of the inhibiting (toxic) action of trifluralin. The test-objects were seeds of wheat *Triticum aestivum*. The length of the roots and seedlings of the wheat was used as a test-response.

2. Experimental

2.1 Materials

Iron(II) sulfate(≥ 99.7%), a saturated iron(III) chloride solution (≥ 99.0%), poly-*N*-vinylpyrrolidone (PVP, MW: 8000), and ammonium hydroxide (≥ 99.9%) were purchased from Sigma-Aldrich. Trifluralin (≥ 99.9%) was purchased from Sigma-Aldrich. Deionized water was used in the experiment. All chemicals were used directly without further purification.

2.2 Synthesis of nano Fe_3O_4 (Sample 1)

Fe_3O_4 nanoparticles were prepared using iron(II) sulfate and iron(III) chloride according to the chemical co-precipitation method. To this end, 0.560g of iron(II) sulfate was dissolved in 35 mL of deionized water. Three milliliters of a 0.01-mol/L saturated iron(III) chloride solution were added dropwise to the stock solution. After 30 min of reaction, 15 mL of ammonium hydroxide was added. Synthesis was conducted at 75˚C in an argon atmosphere under stirring for 5 h.

The resulting black powder of magnetite was separated from the mother solution, washed with ethanol, and dried at 100°C.

2.3 Synthesis of nano Fe_3O_4 PVP (Sample 2)

Fe_3O_4 nanoparticles were prepared according to the chemical co-precipitation method using iron(II) sulfate and iron(III) chloride in the presence of poly-*N*-vinylpyrrolidone (PVP). To this end, 0.560g of iron(II) sulfate was dissolved in 35 mL of distilled water. Three milliliters of a 0.01-mol/L PVP solution and 3 mL of a saturated iron(III) chloride solution were added dropwise to the stock solution. After 30 min of reaction, 15 mL of ammonium hydroxide was added. Synthesis was conducted at 75˚C in an argon atmosphere under stirring for 5 h.

The resulting black powder of magnetite was separated from the mother solution, washed with ethanol, and dried at 100°C.

2.4 Methods

The resulting material was studied by FTIR spectroscopy using a PerkinElmer Spectrum

100 FT-IR spectrometer in a spectral range of 650–4000 cm^{-1}. Spectral range was about 400–4000 cm^{-1} into vaseline. The samples were prepared in vaseline for recording in a range of 400–4000 $см^{-1}$.

X-ray diffraction analysis was carried out on a DRON-UM diffractometer using a (e-K_α- radiation at λ = 1.93604 A°) in a range of 2θ = 10°–80° at room temperature.

Scanning electron microscope (SEM) images were recorded with a Quanta 200 electronic microscope (ESEM) operating at 30 kV with secondary and backscattering electrons in a high vacuum mode.

The effect of iron nanoparticles on the germination capacity of wheat seeds against the background of the inhibiting (toxic) action of trifluralin was studied. The test-object was seeds of wheat *Triticum aestivum*. The test response was the length of the roots and shoots of the wheat. Biotesting was conducted by the soil plate method [3]. A colloidal solution of Fe_3O_4 (sample 1) and Fe3O4/PVP (sample 2) magnetite nanoparticles in concentrations of 10, 50, and 100 mg/kg of dry soil was used. The prepared colloidal solutions of iron-containing nanoparticles and trifluralin were mixed and incubated for 1 day and 4 days.

The experimental results were subjected to statistical processing using the Microsoft Excel software package for Windows XP.

3. Results and discussion

To study the effect of nanoparticles on the remediation of trifluralin, two types of magnetite nanoparticles–particles without stabilization (nano Fe_3O_4, sample 1) and particles coated with functional groups as a stabilizer (Fe_3O_4/PVP, sample 2) –were synthesized and studied.

The morphology and sizes of the Fe_3O_4 nanoparticles (sample 1) are shown in Fig. 1. The micrographs show that the nanoparticles are spherical and have sizes of 8–20 nm. The spread in size is characteristic of the formation of nanoparticles by synthesis without a stabilizer. Since the nanoparticles exhibit high surface energy, they undergo a rapid interparticle interaction, coarsening, and then aggregation in solution. It is evident from the photographs that the resulting nanoparticles have agglomerated into larger entities with a size of 25–35 nm. Apparently, the formation of the nanoparticles occurs in the iron hydroxide gel matrix. [4]. An important role in the formation of a gel matrix is played by water molecules, which contribute to the formation of a continuous bound system owing to hydrogen bonds.

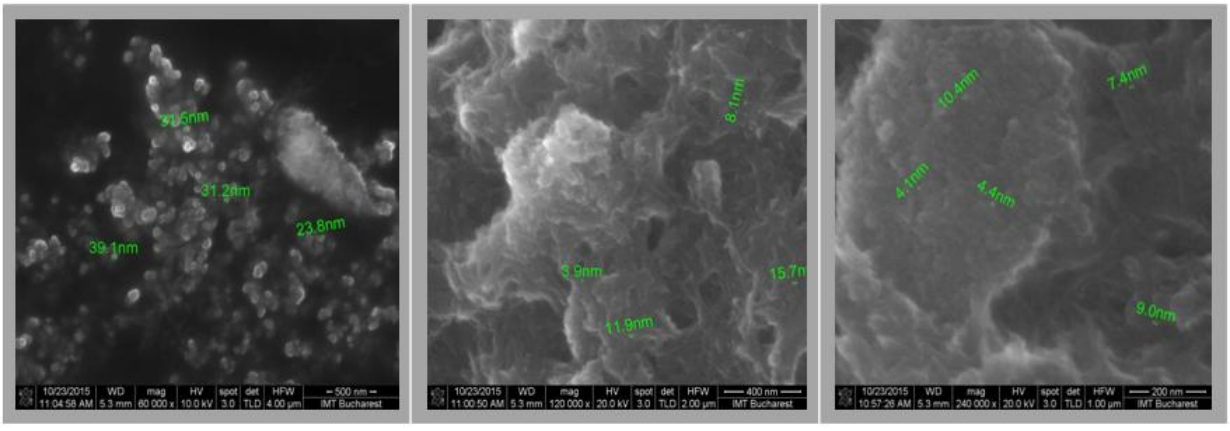

Fig. 1. SEM images of magnetite nanoparticles (sample 1).

Figure 2 shows the diffraction patterns of the Fe_3O_4 nanopowder. Diffraction peaks corresponding to the cubic phase of Fe_3O_4 nanoparticles are observed (space group *Fd3m*, a = 8.3952 Å); the main diffraction peaks correspond to the crystallographic planes of the cubic inverted spinel Fe_3O_4: (111), (220), (311), (222), (400), (333), (440), and (533). The results are in good agreement with the spectra from the database of diffractograms [5]. Thus, the crystallinity of the resulting iron oxide is confirmed. Size d of the Fe_3O_4 crystallites was determined from the half-width of the diffraction peaks by the Scherrer formula

$$d = k \cdot \lambda/(\beta \cdot \cos\theta),$$

where k = 1 is a constant, λ = 1.93604 Å is the X-ray radiation wavelength, β is the full width half maximum, and θ is the diffraction angle.

The crystallite size of magnetite Fe_3O_4, which was calculated according to the X-ray diffraction line width, was $d = 15 \pm 1$ nm.

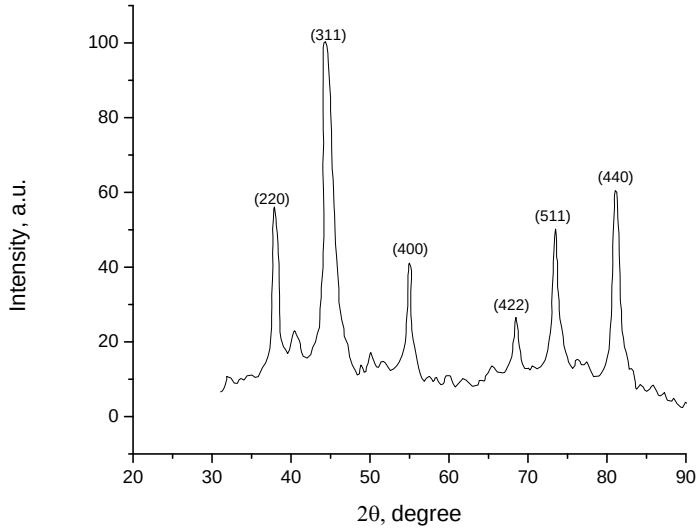

Fig. 2. XRD pattern of Fe_3O_4.

Results of FTIR spectroscopic studies of sample 1 are shown in Figs. 3 and 4. The FTIR spectra of Fe_3O_4 nanoparticles exhibit absorption peaks at 3342.6, 2302–2054, and 1640 cm^{-1} (Fig. 3). The band near at 3342.6 and 1640.2 cm^{-1} is assigned to H–O–H bending vibrations due to the adsorption of moisture. The absorption band around 2054–2302 cm^{-1} is attributed to the existence of CO_2 molecules in the air [4]. At 500–600 cm^{-1}, there is a peak responsible for the Fe–O bond in Fe_3O_4; this peak can be observed in the case of recording the sample in vaseline.

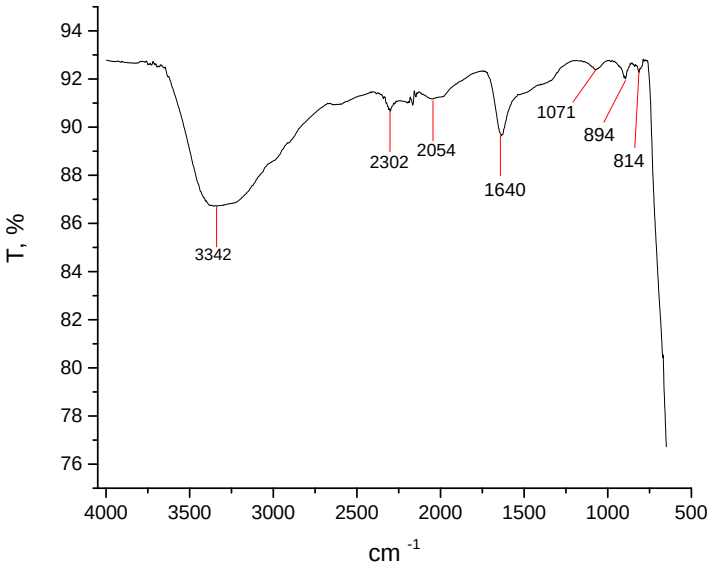

Fig. 3. FTIR spectrum of the Fe_3O_4 nanoparticles.

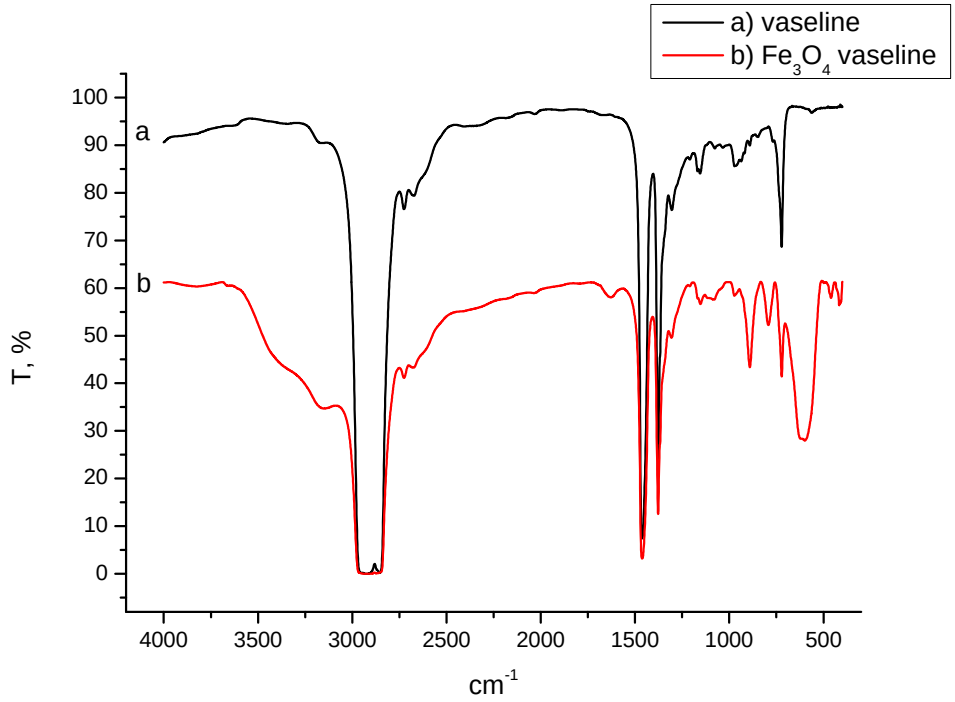

Fig. 4. FTIR spectrum of the Fe_3O_4 nanoparticles (a) and Fe_3O_4 nanoparticles with vaseline (b).

Figure 3 shows the IR spectrum of sample 1 recorded in vaseline. The main absorption peaks are attributed to the absorption relating to vaseline (a), while the split peak at 589–623 cm^{-1} corresponds to the Fe–O bond of the magnetite [6].

Further studies were conducted with sample 2 synthesized with PVP used as a stabilizer of magnetite nanoparticles.

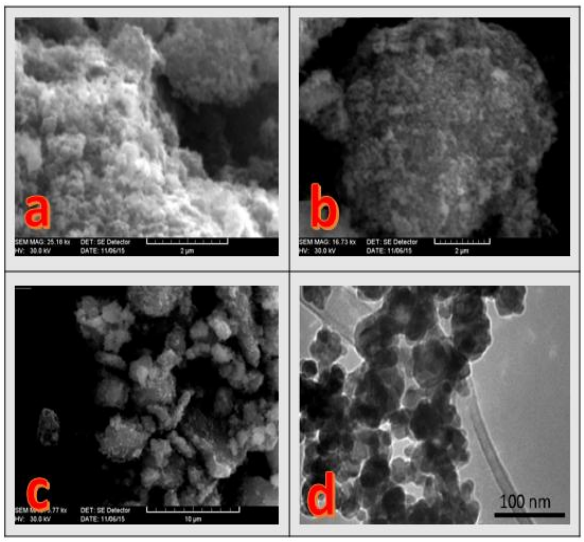

Fig. 5. SEM and TEM images of nano Fe_3O_4/PVP.

Figure 5 shows the morphology of the nano magnetite sample synthesized in the presence of PVP with clearly visible globules composed of nanoparticles surrounded by PVP; the size is 35–50 nm.

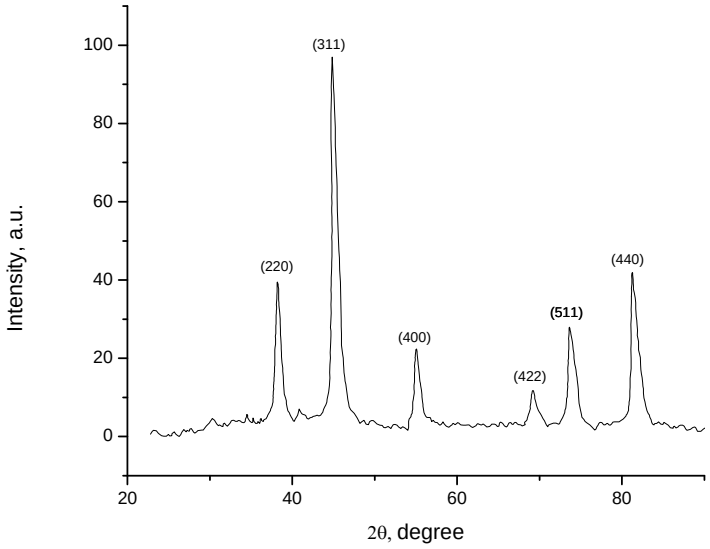

Fig. 6. XRD pattern of Fe_3O_4/PVP.

Figure 8 shows X-ray diffraction patterns of the Fe_3O_4 nanopowder. The observed diffraction peaks correspond to the cubic phase of Fe_3O_4 nanoparticles (space group *Fd3m*, a = 8.3952 Å). The main diffraction peaks correspond to the crystallographic planes of cubic inverted spinel Fe_3O_4: (111), (220), (311), (222), (400), (333), (440), and (533). Thus, the crystallinity of the resulting magnetite is confirmed. Size d of the Fe_3O_4 crystallites is d = (35± 1) nm; this value corresponds to this microscopy data.

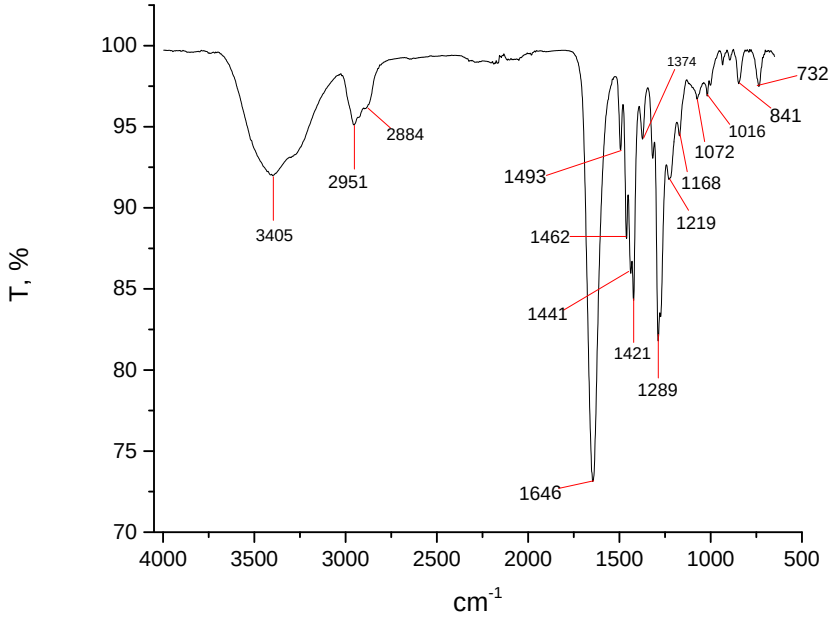

Fig. 7. FTIR spectrum of the PVP.

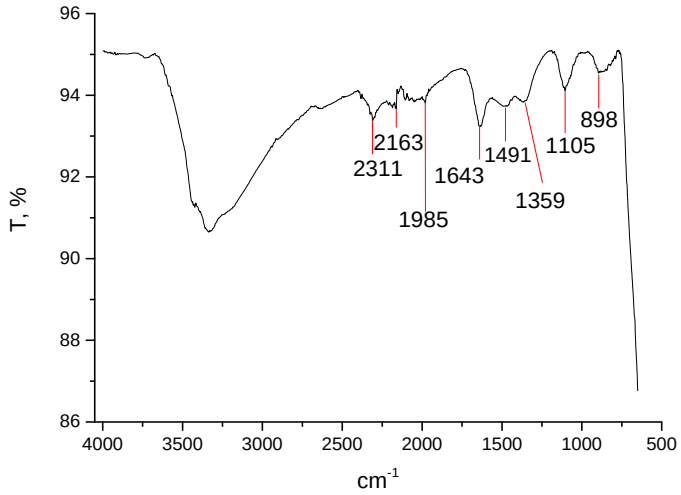

Fig.8. FTIR spectrum of the Fe_3O_4/ PVP nanoparticles.

Comparison of the spectra of the prepared Fe_3O_4/PVP nanoparticles (Fig 5) and pure PVP reveals similar absorption bands in regions of 3600–2400 and 1650–650 cm^{-1}. The peak observed in pure PVP at 1645 cm^{-1}, which is attributed to the C=O bonds, is red-shifted to 1559.6 cm^{-1} as a result of the interaction between the carbonyl oxygen and the magnetite [6]. In the absorption region of 1500–1200 cm^{-1}, the absorption bands of PVP overlap with the bands of the hydrated oxide; an interaction between them occurs. As a result, a broad band with a maximum at 1406.5 cm^{-1} and a peak at 1341.3 cm^{-1} is observed. The first of these bands is related to the peak observed in the Fe_3O_4 nanoparticles at 1448.2 cm^{-1}, which stems from the hydrated iron oxide, yet is shifted to 1406.5 cm^{-1}; the peak at 1341.3 cm^{-1} is apparently attributed to the occurrence of covalent bonds between PVP and Fe_3O_4 nanoparticles. Thus, our FTIR studies show that the magnetite nanoparticles and the polymeric stabilizer undergo a chemical reaction by coordination

of the magnetite particles with the nitrogen and oxygen atoms in PVP, as evidenced in [7].

Thus, PVP was used as a polymeric stabilizator for the formation of magnetite nanoparticles. The introduction of the polymer during synthesis provides the formation of negatively charged carbonyl group on the surface of the magnetite nanoparticles, which contribute to the formation of a stable colloidal solution; the presence of large PVP molecules provides the occurrence of a steric effect and hinders their aggregation. Colloidal solutions based on the synthesized nanoparticles can be used in biotest.

4. Biological test

Trifluralin is a soil-active systemic herbicide. It effectively inhibits cereal, many monocotyledonous, and some dicotyledonous annual weeds. The toxic effect of this herbicide lies in the inhibition of the growth of roots, namely, in violation of the cell division processes in the roots of plants. In plants subjected to this treatment, secondary roots are not developed and the growth of the shoot stops; finally, the plant dies [8]. Trifluralin can exert a phytotoxic action on some cereals, such as wheat, oats, rice, and corn [9]. Since trifluralin is environmentally hazardous, the use of herbicides containing this substance is banned in the EU; however, they are still used in the United States, many Asian countries, and Russia. In 2012, trifluralin was excluded from the State Register of plant protection products and fertilizers permitted for use in the territory of the Republic of Moldova; however, residues of the pesticide are registered in soils of Moldova to the present day.

In the experiment described below, we studied the effect of two compounds of Fe_3O_4 magnetite nanoparticles with a size of 8–20 nm on the growth of wheat seedlings. One of the compounds (sample 2) contained a polyvinylpyrolidone (PVP) stabilizer; the other (sample 1) did not. The wheat seeds were germinated on soil plates; the soil used in the experiments was contaminated with pesticides for a long time; it was taken in the territory of the former warehouse of pesticides and fertilizers in Singera, Moldova. Colloidal solutions of Fe_3O_4 magnetite nanoparticles (samples 1 and 2) in concentrations of 10, 50, and 100 mg/kg of dry soil were used. The prepared colloidal solutions of nanoparticles were introduced into the contaminated soil and incubated in a germination chamber at a temperature of 25°C for 1 day (test versions 1–3) and 4 days (test versions 4–6). After this time, the wheat seeds were placed on soil plates and further incubated for 3 days. On the 4th day, the seed germination and the length of roots and shoots were estimated. The references were the wheat seeds grown on plates of the reference soil containing no pesticide residues, which was taken in the vicinity of the territory of the former warehouse of pesticides in Singera (reference), wheat seeds germinated on plates of pesticide-contaminated soil incubated for 1 day (reference 1) and 4 days (reference 2) in a germination chamber along with test versions.

After the treatment of the contaminated soil with solutions of nanoparticles of sample 1 for 1 day, no changes in the length of the roots of the test plants were recorded, except for a slight inhibition in the case of using a concentration of 100 mg/kg of soil (Table 1). A certain stimulatory effect–33%–on the growth of the shoots was observed at a concentration of 10 mg/kg of soil. The incubation of the soil with solutions of nanoparticles of sample 1 for 4 days contributed to an increase in the root length by 123.7–158.1% depending on the nanoparticle concentration. The length of the shoots remained at the reference level.

Table 1. Growth of wheat seedlings in the pesticide-contaminated soil after the introduction of Fe_3O_4 magnetite nanoparticles (sample 1) into the soil

Test version	Nano Fe_3O_4, sample1, mg/kg of dry soil	Root length, mm			Shoot length, mm		
		M ± m	% of reference	% of reference 1/2*	M ± m	% of reference	% of reference 1/2*
Reference	-	49.15 ± 5.84	100.00		31.90 ± 3.61	100.00	
Reference 1	-	5.35 ± 0.59	10.89	100.00	3.00 ± 0.52	9.40	100.00
1	10	5.55 ± 1.09	11.29	103.74	4.00 ± 0.37	12.54	133.33
2	50	5.20 ± 1.00	10.58	97.20	3.60 ± 0.28	11.29	120.00
3	100	4.95 ± 0.47	10.07	92.52	3.15 ± 0.31	9.87	105.00
Reference 2	-	4.65 ± 0.90	9.46	100.00	4.05 ± 0.28	12.70	100.00
4	10	6.70 ± 0.50	13.63	144.09	4.50 ± 0.28	14.11	111.11
5	50	7.35 ± 0.65	14.95	158.06	4.50 ± 0.39	14.11	111.11
6	100	5.75 ± 0.71	11.70	123.66	4.00 ± 0.34	12.54	98.77

Note: Versions 1–3 are related to reference 1; versions 4–6 are related to reference 2.

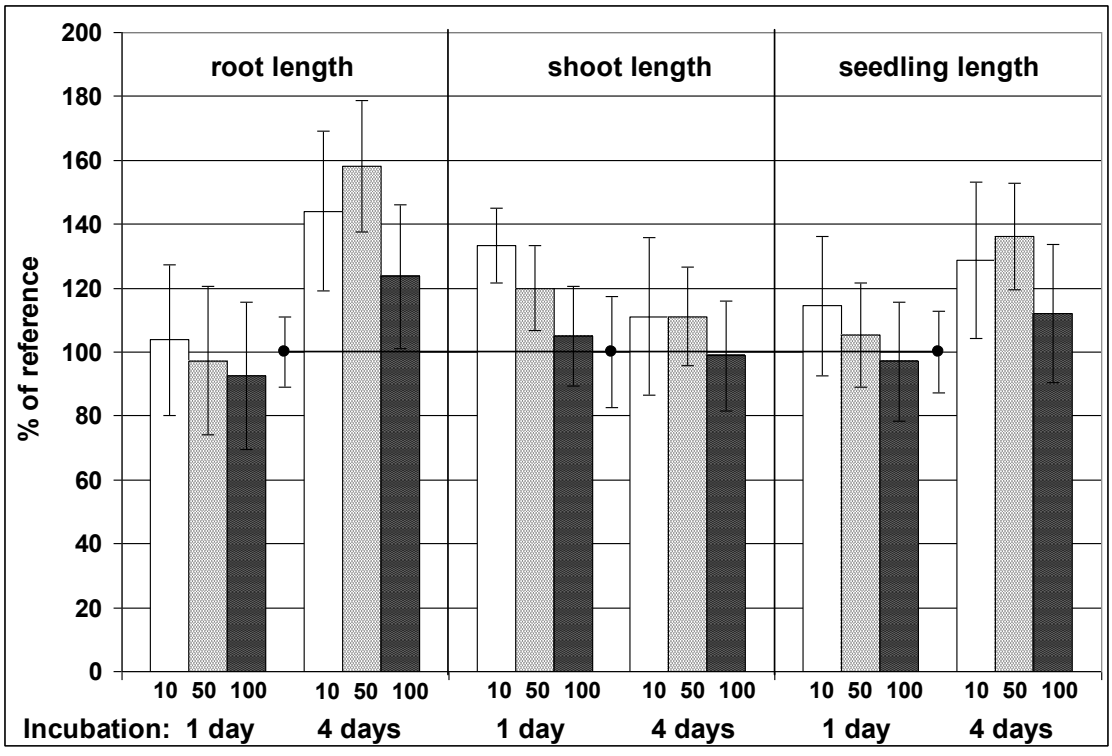

Fig. 9. Effect of Fe_3O_4 nanoparticles (sample 1) on the seedling length of the wheat inhibited by trifluralin.

The maximum effect was observed in the case of introduction of magnetite nanoparticles of sample 1 in a concentration of 50 mg/kg of soil; an increase in the concentration to 100 mg/kg of soil led to the weakening of the effect (Table 1, Fig. 9). After the incubation of the soil with solutions of nanoparticles of sample 1 for 1 day, the total growth of the seedlings remained at the reference level (with a slight stimulatory effect of 14.4% at a concentration of 10 mg/kg of soil); an increase in the incubation time to 4 days contributed to an increase in the seedling length by 12.1–36.2%, mostly owing to the elongation of the roots.

The introduction of solutions of nanoparticles of sample 1 into the contaminated soil and incubation for 1 day had the following effect on the growth of the test plants: the root length and the shoot length increased by 13.1–39.3 and 14.6–24.4%, respectively, depending on concentration; the effect of concentrations of 50 and 100 mg/kg of soil differed only slightly (Table 2). After the incubation of the contaminated soil with solutions of magnetite nanoparticles of sample 2 for 4 days, the stimulatory effect did not disappear; instead, it became even stronger: the root length and the shoot length increased by 49.2–78.5 and 12.7–49.1%, respectively, depending on nanoparticle concentration.

Table 2. Growth of wheat seedlings in the pesticide-contaminated soil after the introduction of Fe_3O_4 magnetite nanoparticles of sample 2 into the soil

Test version	Nano Fe_3O_4, sample2, mg/kg of dry soil	Root length, mm			Shoot length, mm		
		M ± m	% of reference	% of reference 1/2*	M ± m	% of reference	% of reference 1/2*
Reference	-	48.35 ± 3.68	100.00		28.75 ± 2.90	100.00	
Reference 1	-	3.05 ± 0.65	6.31	100.00	2.05 ± 0.18	7.13	100.00
1	10	3.45 ± 0.72	7.14	113.11	2.05 ± 0.24	7.13	100.00
2	50	4.25 ± 0.71	8.79	139.34	2.35 ± 0.27	8.17	114.63
3	100	4.15 ± 0.70	8.58	136.07	2.55 ± 0.32	8.87	124.39
Reference 2	-	3.25 ± 0.72	6.72	100.00	2.75 ± 0.48	9.57	100.00
4	10	3.50 ± 0.81	7.24	107.69	3.10 ± 0.68	10.78	112.73
5	50	5.80 ± 0.67	12.00	178.46	4.10 ± 0.43	14.26	149.09
6	100	4.85 ± 0.73	10.03	149.23	3.90 ± 0.48	13.57	141.82

Note: Versions 1–3 are related to reference 1; versions 4–6 are related to reference 2.

With respect to the total seedling length (Fig. 4), the incubation of the contaminated soil with solutions of nanoparticles of sample 2 for 1 day had a positive effect (129.4–131.4% of reference 1), which became stronger with an increase in the incubation time to 4 days (145.8–165.0% of reference 2). The growth stimulation effect was evident from an increase in the length of both the roots and shoots of the wheat; the maximum effect was observed in the case of using a concentration of 50 mg/kg of dry soil and the incubation of the soil for 4 days.

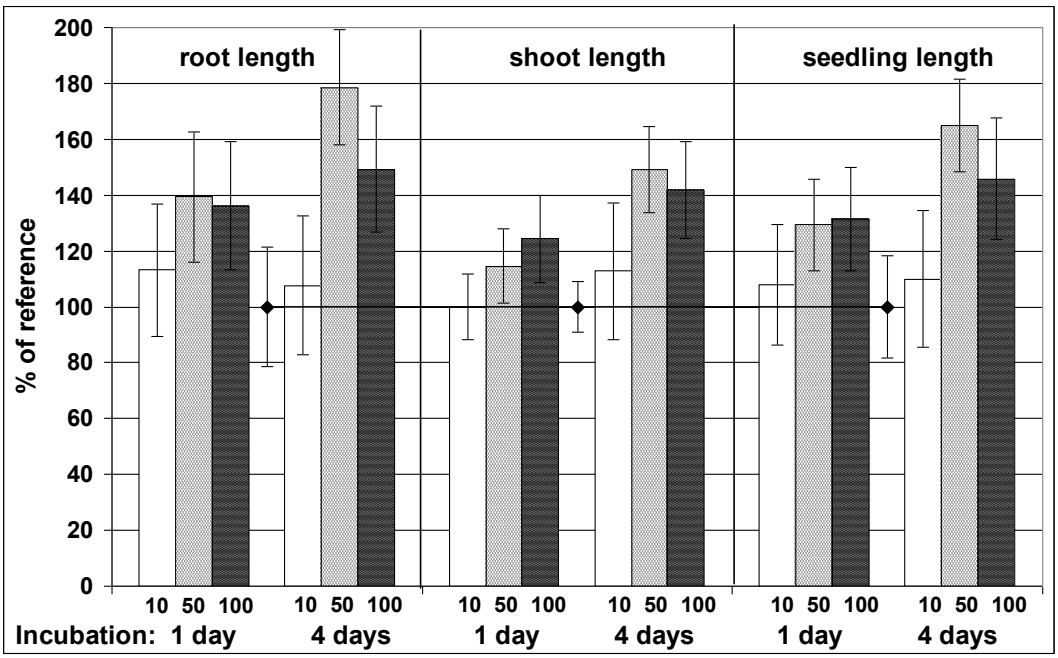

Fig. 10. Effect of Fe_3O_4 S12 nanoparticles on the seedling length of the wheat inhibited by trifluralin.

5. Conclusions

Magnetite nanoparticles coated with PVP used as a stabilizer and without it were prepared by chemical coprecipitation. The size of particles was 8–20 nm (sample 1) and 50–60 nm (sample 2).

The stimulatory effect on the growth of wheat seedlings in the long-term pesticide-contaminated soil was evident from an increase in the length of both the roots and the shoots; the maximum effect was observed in the case of incubation of the soil with a solution of Fe_3O_4 (sample 2).magnetite nanoparticles in a concentration of 50 mg/kg of dry soil for 4 days.

An increase in the time of incubation of Fe_3O_4 iron nanoparticle solutions with the long-term pesticide-contaminated soil from 1 to 4 days leads to the occurrence of a stimulatory effect in the case of using Fe_3O_4 nanoparticles without any stabilizer (sample 1) and to an enhancement of the growth stimulation effect in the case of Fe_3O_4 nanoparticles with a PVP stabilizer

References

[1] Xiaohu Xia, Jie Zeng, L. Kyle Oetjen, Qingge Li, and Younan Xia, Am. Chem. Soc. 134, 1793, (2012).
[2] J. A. Hakala and Y. P. Chin, J. Agric Food Chem. 58(24), 12840, (2010).
[3] J. H. Langwaldt and J. A. Puhakka , Biodegradation. 13, 5, 317, (2002).
[4] J. M. Tor, C. Xu, J. M. Stucki, and G. K.Sims, Environ. Sci. Technol. 34, 3148, (2000).
[5] N. A. Krasil'nikov, Metody izucheniya pochvennykh mikroorganizmov i ikh metabolitov, Mosk. Gos. Univ., Moscow, 1966, 158 p.

[6] K. Koczkur, S. Mourdikoudis, L. Polavarapu, and S. Skrabalak, Dalton Trans, 44, 17683, (2015).
[7] ICSD Database, Version 1.2.0, 2003, 50567 XRD.
[8] J. T. Keiser, C. W. Brown, and R. H. Heidersbach, J. Electrochem. Soc. 129, 2686, (1982).
[9] G. Ghosh, M. Naskar, A. Patra, and M. Chatterjee, Opt. Mater. 28, 1047, (2006).
[10] R. Y. Hong, J. H. Li, L. L. Chen, D. Q. Liu, H. Z. Li, and Y. L. Zheng, Powder Technol. 189, 426, (2009).
[11] S. Ya. Popov, L. A. Dorojkina, and V. A. Kalinin, Osnovy khimicheskoi zashchity rastenii, ed. S. Ya. Popov, Art-Lion, Moscow, 2003.
[12] V. A. Zinchenko, Khimicheskaya zashchita rastenii: sredstva, tekhnologiya i ekologicheskaya bezopasnost', Koloss, Moscow, 2012.

ANOMALIES IN MAGNETORESISTANCE OF BISMUTH WIRES IN HIGH MAGNETIC FIELDS

E. Condrea[1,2]

[1]*Institute of Electronic Engineering and Nanotechnologies, Academy of Science of Moldova, Chisinau, 2028 Republic of Moldova*
[2]*International Laboratory of High Magnetic Fields and Low Temperatures, Gajowicka 95, 51-421 Wroclaw, Poland*
E-mail: condrea@nano.asm.md

(Received December 1, 2015)

Abstract

Anomalous peaks in the magnetoresistance of Bi wires have been observed in a high magnetic field far above the quantum limit of the electrons. By combining a magnetic field and a uniaxial strain, we have obtained a modification of the electronic structure; as a result, the quantum limit for light and heavy electrons has changed in a different way. The origin of anomalous peaks is attributed to the complexity of the structure of the lowest Landau level of heavy electron pockets in a high magnetic field.

1. Introduction

The present work was motivated by the previous observations of the variety of unexpected anomalous features manifested in bulk Bi in an ultraquantum magnetic field. The electronic structure of bismuth can be modified under the action of a high magnetic field, where various kinds of magnetic-field-induced instabilities may occur. Low densities of electrons combined with their small effective masses and a small energy overlap are strongly affected under a magnetic field that gives rise to significant changes in the Fermi surface topology and in the dependence of the carrier density on magnetic field. In high magnetic fields, the band overlap diminishes and a magnetic-field-induced semimetal–semiconductor transition [1] is observed at 88 T. In the field where the energy overlap becomes small and approaches zero, the occurrence of various types of magnetic-field-induced phenomena is anticipated [2, 3].

In relatively high magnetic fields, where all Landau levels (LLs), except for the lowest Landau level (LLL), have passed through the Fermi level, the so-called quantum limit (QL) is achieved. A low carrier density in bulk Bi allows attaining a QL for all carriers in a moderate magnetic field. For example, if the magnetic field is oriented along the trigonal axis, both electrons and holes can be placed into the LLL below 9 T. Therefore, we would not expect any features in the transport properties of the carriers in a magnetic field above 9 T. Nevertheless, a lot of unexpected effects were experimentally detected in bulk Bi well beyond the QL, namely in the case where the magnetic field is oriented along the trigonal axis or close to it [4–12]. The measurements of the Nernst response in bismuth revealed giant quantum oscillations and unknown peaks up to a magnetic field of 33 T [4, 8]. Furthermore, anomalous peaks were observed even in higher magnetic fields of up to 50 T [8, 9]. The unidentified peaks found by Behnia [4], initially were associated with fractional peaks as signature of electron fractionalization possible for bulk Bi in a high magnetic field. Further, Zhu et al. [6] suggesting

the twinning scenario, concluded that the unidentified peaks found by Behnia are not fractional peaks as was initially assumed [4]; instead, those peaks originate from the crossing of the Fermi energy level by the LLs of holes from a secondary twined crystal. In the conclusions, the authors of [6] left an open question: why the magnitude of the unidentified peaks caused by the LLs of secondary twined crystal is comparable to those of the primary crystal? This question was raised again [7] at an attempt to explain a spontaneous symmetry breaking observed in the magnetostriction measurements where the authors have failed to detect traces of secondary twined crystal. In the same article, the authors put forward the idea that the observed angular asymmetries of magnetostriction point to a different density of states (DOS) of electrons at the Fermi energy level presumably due by the electron interaction which operates selective between the identical valleys for magnetic fields along the trigonal axis. A similar evidence of a different DOS was found [10] in measurements of the Shubnikov–de Haas (SdH) oscillations at the rotation of a magnetic field around the trigonal axis that revealed the difference in the amplitude of oscillations from the three identical electron valleys. To justify the emergence of a different DOS, in the last mentioned papers [7, 10] sophisticated theoretical arguments have been advanced including a quantifying of the components of the mobility tensor, a selective Coulomb interaction and scenario of valley nematicity, which are beyond the framework of the single particle model.

Another interpretation of the unusual peaks observed in the Nernst effect of bulk bismuth [4–6] has been recently proposed by Mikitik and Sharlai [11]. Their explanation is based on the effect of the spontaneous symmetry breaking which is caused by the electron–phonon interaction inducing the magnetostriction. As a result, a first-order phase transition can take place in certain intervals of magnetic fields when LLs of equivalent electron pockets approach the Fermi energy. This situation occurs in high magnetic fields (H > 9 T) oriented along the trigonal axis where the LLL of electrons 0^-(e) is filled, while the next LLL 0^+(e) is close to the Fermi energy level and could cross it. Further, the authors admit the possibility of spontaneous symmetry breaking of two equivalent electron ellipsoids in the case of the magnetic field oriented along the bisectrix direction. The last assumption will guide the discussion of our results in this context.

The origin of most of the observed Nernst peaks above the QL has been explained [13] in terms of the two-band model advanced by Smith, Baraff, and Rowell [14]. According to the conclusions in [13], this simple model is sufficient to account for the general shape of some experimental curves for the different magnetic field orientations.

Another advanced idea [15] of the responsibility of the surface states for anomalous high-field peaks has been convincingly denied by K. Behnia [16] in his detailed analysis of the Nernst experiment in bulk Bi. Another assumption [17] that high field features of bismuth are related to the electronic properties of the surface states refers to the Bi nanowires with d = 90 nm. Results of the investigations [17] of the effect of strong Rashba spin–orbit coupling on the superconducting proximity assume the existence of the surface channels that manifest specific conduction properties oscillating in a magnetic fields up to 11 T for thin Bi nanowires (d < 100 nm) with superconducting contacts. To date, however, there has been no reliable experimental evidence of the surface states in Bi wires, while there is the problem of correct separation of the effects originating from bulk or from surface of the wires.

In the cases where the magnetic field is oriented along the bisector direction, the QL for both light and heavy electrons is attained in a magnetic field less than 2.5 T, while the heavy T-holes remain in the quasi-classical regime. Some interesting features manifested in the magnetoresistance (MR) dependence in this field direction were observed in the previous

experiments performed in a magnetic field of up to 40 T reported by Brandt [2] and Hiruma [18]. In those earlier experiments [2, 18] on bulk Bi in a magnetic field oriented along the bisector and/or binary axis, the dependence of magnetoresistance exhibited a broad peak followed by a sharp decrease in the MR in a magnetic field of 32 T. Based on the "camel-back" structure in the $k(H)$ dependence of light electrons (k is the wave vector component in the direction of the magnetic field) proposed by Vecchi et al. [19], it was supposed that the peak observed at 32 T can be attributed to the crossing of the Fermi energy level by the LLL of light electrons [18]. More recently, results on the MR and Nernst effect [5, 8, 9], as well as the important theoretical calculations for a field oriented along different crystallographic directions [10–13, 19–22], have been reported.

In general, the variety of unexpected features [4–12] manifested in an ultraquantum magnetic field in the bulk Bi may not always be explained in terms of simple models. These complexities suggested that the band structure of bulk Bi becomes so intricate in a high magnetic field that, for any suitable explanation, we should take into account many factors including the enhancement of the interaction effect and its influence on the LL spectrum in the vicinity of the QL. In all instances, a plurality of observed phenomena beyond the QL, which cannot always be understood in the framework of the known models, requires new theoretical developments and inspires the expansion of experiments on bismuth in a high magnetic field.

Most of the published results have respect to experiments on bulk Bi that differ only in the configuration of the experiment with the different orientations of the magnetic field relative to the crystallographic axis and/or in the magnetic field range. At the same time, in addition to magnetic fields, the band structure of Bi is sensitive to other external influences. However, the design of measurements in a magnetic field may be diversified by using an additional external influencing factor, for example, uniaxial deformation.

It is well known that even a small lattice deformation leads to substantial changes in the energy spectrum and, accordingly, in values of kinetic parameters of electrons and holes [23]. It has been shown that deformation along some crystallographic directions in Bi can easily induce an Electronic Topological Transition (ETT), which is also referred to as a 2.5 Lifshitz transition [24]. Beyond the interesting effects caused by the Lifshitz transition in bulk Bi [25], there are similar effects in the transport properties of Bi whiskers [26] and Bi wires [27, 28]. The glass-coated Bi wires support strong elastic deformations up to the extension $\varepsilon = 3.0\%$. Our earlier investigations of the galvanomagnetic transport properties in uniaxially strained wires have revealed a non-monotonous behavior of electrical resistance and the sign change from positive to negative in the Seebeck coefficient for the Bi wires undergoing the Lifshitz transition of the Fermi surface [28].

Application of a uniaxial deformation directed along the bisectrix axis provides the occurrence of selective changes in the band overlap between T-holes and light electrons and between T-holes and heavy electron ellipsoids, which can be monitored by means of the SdH oscillations. It should be noted that the uniaxial strain in Bi wires contributes to an increase in the band overlap between pockets of heavy L-electrons and T-holes, in contrast to a decrease in this parameter under the action of a magnetic field.

The goal of this work was to study the transport properties of Bi wires under the simultaneous action of a uniaxial deformation and a magnetic field oriented along the bisectrix axis. By combining a high magnetic field and a strain, we have obtained a modification of the electronic structure of the wires; as a result, the QL for light and heavy electrons could be changed in different ways. For the case where heavy electrons are in the QL, a correlation between the exit of the LLL of light electrons and the Lifshitz transition was found. The result is

that the critical magnetic field of the ETT has decreased and, consequently, the magnetic field range of occurrence of magnetic-field-induced instabilities in the electron–hole system has been extended.

2. Experimental results and discussion

Investigated single-crystalline Bi wires were obtained using the glass-coated melt spinning method [29]. The axis of the prepared wires is oriented at an angle of about 19° to the C_1 bisector axis in the bisector–trigonal plane. Experimental procedure and methods are described in detail in our previous papers related to the galvanomagnetic properties of Bi wires [28, 30]. In the given work we consider the results of measurements in the magnetic field extended up to 35 T and focus on the explanation of the unusual features of magnetoresistance in a high magnetic field.

The measurements of longitudinal MR ($I \parallel B$) were made on Bi wires with diameters of d = 0.2 – 2.0 μm in a magnetic field parallel to the axis of the wire, i.e., close to the bisector axis. Figure 1 presents the dependence of the longitudinal MR for a wire with d = 400 nm in the pulsed magnetic field of up to 35 T. The non-monotonic field dependence of MR in the range of low magnetic field (up to 10 T) is similar to that reported previously for Bi wires [31]. In accordance with the Chambers theory [32] the longitudinal MR achieves its maximum, and after B_{max}, starts decreasing due to decrease in the carrier-surface scattering. The SdH oscillations are observed as the resistance maxima: weak oscillations from electrons in a low magnetic field and more visible from holes in a high magnetic field. The QL achieved for all electrons at magnetic field above ~ 3 T is followed by the negative MR range with an increase between 7 and 35 T.

Some instabilities evident as weak oscillations (wiggles) were observed in a magnetic field around 15 and 20 T. The most prominent feature of MR in a higher magnetic field is the presence of a sharp peak at 33 T. The magnitude of the unexpected peak is larger than that due to the SdH oscillations from holes and even than that due to the crossing of the Fermi level by the first Landau level of electrons in the QL. At the first glance, one can assume that the observed unusual features may be an indicator of unknown effects. On the other hand, the possible unexpected changes in the energy spectrum in the given field orientation may give the appearance of the anomalies in the transport properties that can nevertheless be understood in terms of well-known models of the band structure in bulk Bi.

In order to explain the origin of the observed unusual features of the MR dependence presented in Fig. 1, we will analyze the evolution of the energy spectrum with the magnetic field oriented along the bisector axis. From the well-established band structure [33] of bulk Bi, it is known that the transport in the bisector direction is provided by three groups of carriers: holes from the T-ellipsoid, light electrons from the ellipsoid (A) elongated along the bisectrix axis, and heavy electrons from the two ellipsoids (noted as B and C) placed symmetrically relative to the bisector axis.

In order to verify the contribution of different groups of carriers to the electrical conductivity in Bi wires, we conducted the Fourier analysis of SdH oscillations on the MR measurements using a slow sweep of the magnetic field in the Bitter magnet of up to 14 T. Quantum oscillations from three groups of carriers are visible on the derivative dependence of resistance dR/dB as a function of $1/B$. The calculated frequency of SdH oscillations for the heavy electrons from two equivalent ellipsoids is $F_{B,C}$ = 2.7 T; for light electrons, F_A = 1.3 T; and for T-holes, F_h = 16.1 T, which is in agreement with data for bulk Bi crystals oriented at an angle of about 19° with the bisector axis in the bisector–trigonal plane.

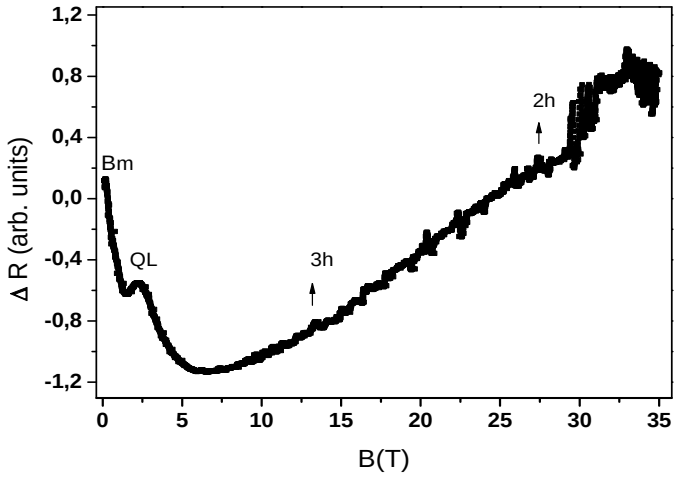

Fig. 1. Longitudinal magnetoresistance for Bi wire with d = 400 nm in a magnetic field up to 35 T at T = 4.2 K. Arrows indicate: QL_e is quantum limit of electrons, 2_h and 3_h are indexed as peaks of quantum oscillations from holes, B_{max} is the Chambers maxim.

To better understand the behavior of the MR dependences, we should trace the change in the carrier concentrations with increasing magnetic field oriented along the bisector axis. Unfortunately, we have not found any references with theoretical calculations on a variation in the carrier density in a high magnetic field in the bisector direction, except for the presented detailed calculations [5] for all the carriers, however, only up to 12 T; and Landau spectrum only for holes [6] up to 30 T.

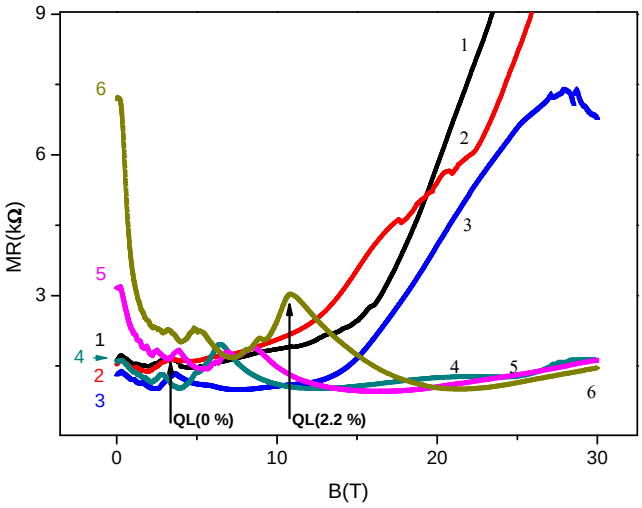

Fig. 2. Magnetoresistance for a Bi wire with d = 400 nm at various strain values: (*1*) 0, (*2*) 0.4, (*3*) 0.8, (*4*) 1.4, (*5*) 1.8, and (*6*) 2.2% at T = 4.2 K. The vertical arrows indicate the position of the QL_e of heavy electrons that shifts to high magnetic field: arrow QL(0) in the non-deformed state and QL(2.2) at a strain value of 2.2%. Inset: expanded version of the MR in a low magnetic field.

Figure 2 shows the data on the longitudinal MR for a wire with d = 400 nm for different uniaxial strain values at a temperature of 4.2 K measured in a resistive magnet of up to 30 T. In a non-deformed state of the wire (curve *1*, Fig. 2), the MR dependence is similar to that of the MR measured in a pulsed magnetic field up to 35 T (Fig. 1). The resistance dependence on strain in the absence of a magnetic field represents a nonmonotonic curve.

3. Discussion

In the following we analyze the observed instabilities evident as weak oscillations (wiggles) of MR manifested in a magnetic field range of 14–16 T. The strain leads to a shift of MR wiggles-instabilities to higher magnetic fields (curves *1–3* in Fig. 2; Figs. 3b–3d). Although these oscillating instabilities are obscured by the increasing background resistance in Fig. 2, they are clearly seen in the MR derivative, as shown in Fig. 3b. Close examination of the derivative dependence *dR/dB* more distinctly reveals the wiggles around 15 T followed by an unidentified peak indexed as X with a positive sign of the jump in the magnetic field range between 3h and 2h hole peaks (arrow X in Fig. 3b) and with a negative sign of the jump in the MTEP dependence (arrow X in Fig. 3a) in a magnetic field of 19.5 T. According to the Fourier analysis of the MR curves, the QL has already been achieved for all the electrons in a field of B = 2.7 T; only heavy T-holes remain in the quasi-classical regime; however, the period of the SdH oscillations from T-holes is not compatible (too large) to fit with the observed oscillating instabilities and with the unidentified peak X. The peak with a negative jump on the MTEP dependence (Fig. 3a) could be regarded as a simple minimum between 3h and 2h hole peaks. However, there are two reasons for opposing this assumption: (i) the peak is so deep that leads to a change in the sign of Seebeck coefficient at a magnetic field of 19.5 T and (ii) the displacement of its position in the magnetic field does not correlate with a decreasing period of quantum oscillations from holes under strain. Therefore, we can unambiguously claim that the wiggles and the anomalous jump in a magnetic field range of 15–20 T may not be attributed to the crossing of Fermi level by the LLs of the holes, which are still in the quasi-classical regime of magnetic field.

As was noted in introduction, to explain the variety of previously detected anomalies of electronic properties in a magnetic field above the QL, in the previous reports [4–22], theoretical models with different approaches—ranging from a simple non-interacting band picture to correlation effects that would lead to the exotic states in bulk Bi—have been invoked.

The possibility of appearance of unexpected features above the QL of electrons was confirmed by theoretical calculations [21] in terms of a tight-binding model appropriate for bismuth, where unconventional Zeeman splitting diminishes the separation between the LLL and the second LL and strongly suppresses the electron QL. Similar conclusions have been made in [13], where the origin of the unidentified peaks in the Nernst coefficient has been explained in terms of a simple model of the electron energy spectrum of bismuth advanced by Smith, Baraff, and Rowell [14]. The computed angular dependences [13] of the positions of electron peaks 0^+, 1^-, and 1^+ in the trigonal–bisector plane is of interest because our measurements were performed with a magnetic field oriented at an angle of 70° to the trigonal axis in the bisector–trigonal plane.

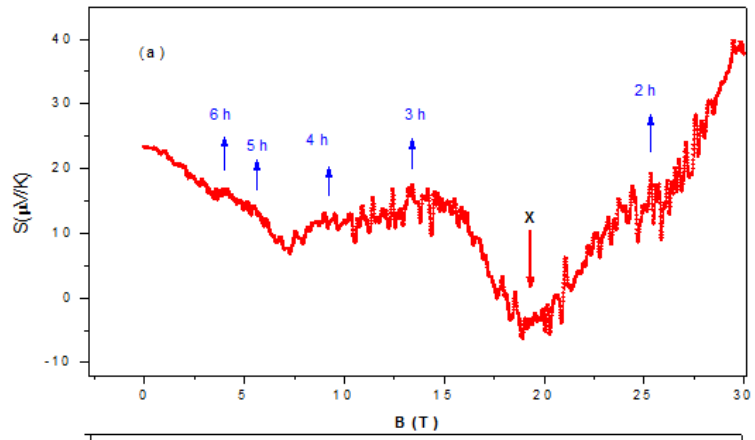

Fig. 3. (a) Seebeck coefficient as a function of magnetic field for Bi wire with d = 400 nm in a non-deformed state at T = 4.2 K. Red arrow indicates the position of the unidentified peak X; peaks of quantum oscillations from holes are indexed as 2_h,–5_h.

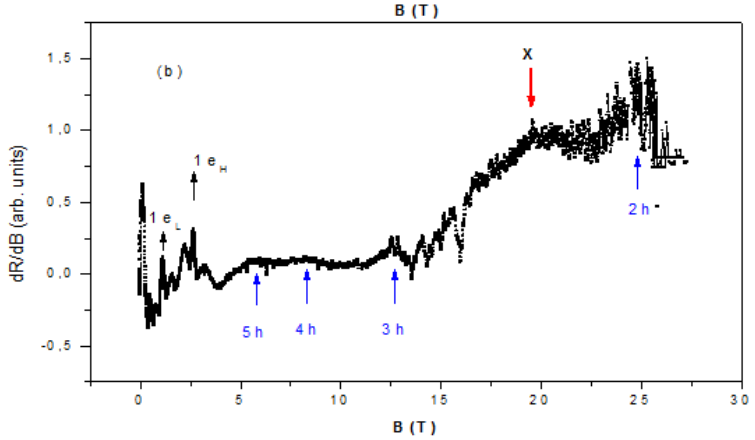

(b) Derivative dependence dR/dB as a function of B for the MR in curve *1* in Fig. 3 for Bi wire in a non-deformed state. The positions of the QL of electrons coincide with the first peak $1e_H$ and $1e_L$ of the quantum oscillations from heavy and light electrons respectively.

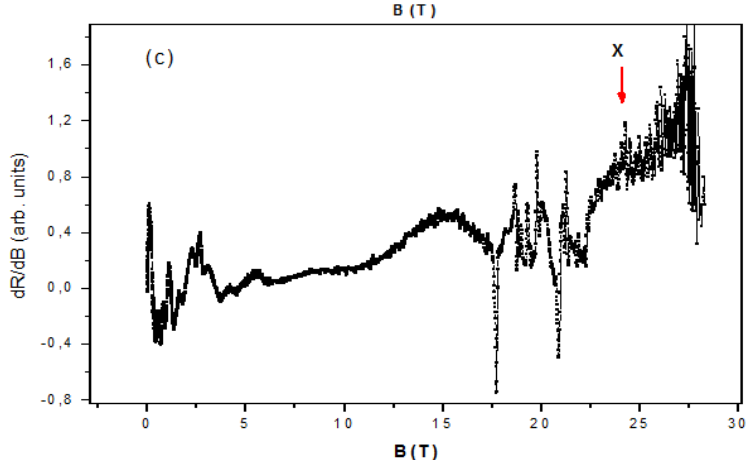

(c) Derivative dependence dR/dB as a function of B for the MR in curve *2* in Fig. 3 for Bi wire at strain values ε = 0.4 %.

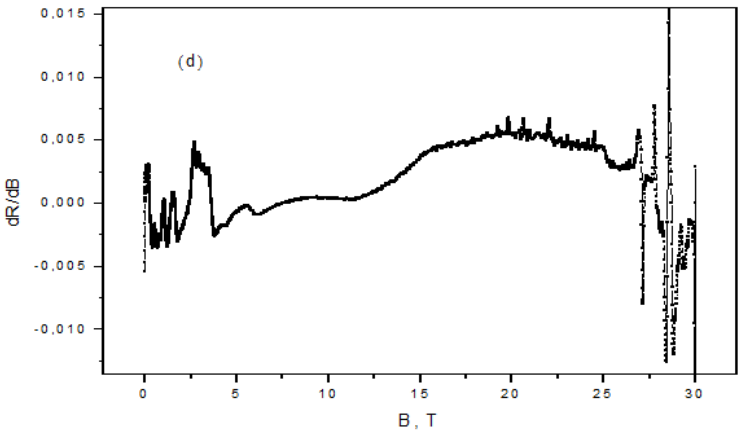

(d) Derivative dependence dR/dB as a function of B for the MR in curve *2* in Fig. 3 for Bi wire at strain values ε = 1.0 %.

Moreover, the prediction of the occurrence of an additional peak in the Nernst signal where the magnetic field is close to the bisectrix direction is an intriguing challenge for measurements in this configuration. Note that, on the MR and Seebeck dependences in a high field, we really observed double-splitting peaks attributed to the crossing of the Fermi level by the $j = 2$ and $j = 3$ Landau levels of holes at ~25.5 and ~14 T, respectively, i.e., close to the positions indicated in Fig. 5 in [13]. In addition to these peaks, an unidentified peak (denoted by X) was observed in a field of 19.5 T.

Further, a twinning scenario was suggested [6] where the origin of anomalous high-field peaks is attributed to the crossing of the Fermi energy level by the LLs of holes from a secondary twined crystal. Apparently, we could also assume the similar nature of unknown peak X, as we cannot exclude the possibilities of the presence of defects or twins in our Bi wires. However, there are several reasons for opposing this supposition: (i) assuming that the peak X is due to the crossing of the Fermi energy level by the $j = 2$ LLs of holes from a secondary twined crystal, one should expect the appearance of other holes peaks from a secondary twined crystal, however, in the experiments we did not observe any additional peaks, modulations, or beats in the visible period of the oscillations from holes; (ii) unidentified peak X is present at $B \approx 19$ T on MR and MTEP dependences for the set of wires with diameters of 0.3– 0.6 and 1.1–1.3 μm. It is inconceivable that the wires obtained under the different technological conditions (diameter is given by the different temperatures and drawing speeds) may have the same twinning structure. Furthermore, the peak at 19 T persists in the Bi wires after the thermal annealing; (iii) the last contradiction is shared with the open question left in the conclusions of [6]: why the magnitude of the unidentified peaks caused by the LLs of secondary twined crystal is comparable to those of the primary crystal?

This question was raised again [7] at an attempt to explain a spontaneous symmetry breaking observed in the magnetostriction measurements where authors have failed to detect traces of secondary twined crystal. Thus, the basic contribution to the signal in magnetic field comes from the primary crystal.

In spite of above mentioned reasons, we cannot completely rule out a twinning scenario. We found additional peaks (supposed of holes from twins) in a magnetic field of 16–19 T at the tilted angle of 70° with the trigonal axis (that is the orientation of the Bi wires) in the figure of plotted Landau spectrum in the trigonal-bisectrix plane [6]. Accidentally or not, the position of our unidentified peak X coincide with the indicated magnetic field interval.

Another interpretation of the unusual Nernst peaks has been recently proposed by Mikitik and Sharlai [11]. Their explanation is based on the effect of the spontaneous symmetry breaking which is caused by the electron–phonon interaction. As a result, a first-order phase transition can take place in certain intervals of magnetic fields when LLs of equivalent electron pockets approach the Fermi energy. This situation occurs in high magnetic fields oriented along the tigonal axis where the LLL of electrons 0^- is filled, while the next LLL 0^+ is close to the Fermi energy level and could cross it. Further, the authors admit the possibility of spontaneous symmetry breaking of two equivalent electron ellipsoids in the case of the magnetic field oriented along the bisectrix direction. The last assumption guides the discussion of our results in this context.

In the measurements, it was observed that the positions of the wiggles in a magnetic field and peak X following them exhibit the same tendency under strain; this fact suggests that they may have the same origin and can apparently be regarded as components of one complex anomaly. It is evident from Figs. 2 and 3 that the applied strain leads to a shift of the MR wiggles to higher magnetic fields simultaneously with an increase in the extreme cross sections of the

heavy electron ellipsoids. The movement of B_{QL} of the heavy electrons under strain is indicated by arrows in Fig. 2.

Might this anomaly be attributed to heavy electron ellipsoids?

It has already been noted [11, 30] that anomalous features associated with the electrons above the QL may arise in transport coefficients in a high magnetic field taking into account the electron–phonon effect, which can lead to a redistribution of the carriers between the pockets. We also may expect manifestation of this effect in Bi wires. In the case where the magnetic field is oriented along the bisectrix axis, the electron–phonon coupling can lead to a redistribution of heavy electrons between two equivalent ellipsoids B and C placed symmetrically relative to the direction of the magnetic field. This reasoning corresponds to the assumption [11] of the first-order phase transition due to the electron–phonon interaction and, generally speaking, could explain the presence of an additional peak at 19.5 T.

As concerns the wiggles, their presence at ~15 T on MR and MTEP dependences of non-deformed Bi wires for a long time was ignored supposing to be due to the mechanical vibrations of the cooling installation. In the previous paper [28] we acknowledged the unknown nature of the observed wiggles in the thermopower around 15 T. Further measurements of MR under strain revealed a dependence of the field position of the wiggles upon the modification of the energy spectrum during deformation. The profile of MR and MTEP dependences with anomalous features were reproduced before the strain and after the removal of stretching load.

We have attempted to justify the position of the anomalies at 15 T in terms of the model of two interacting LLLs proposed by Vecchi et al. [20] and developed it for the explanation of the anomalies in the magnetoreflection line shape of bulk Bi, where it was found that two $j = 0$ levels of the conduction and valence bands approach each other and reach a point of minimum separation at about $B_{min} \approx 15$ T for a magnetic field applied parallel to the bisector axis (j is the quantum number of the LL). As has already been pointed out [21], the correlation effect, which is more pronounced in this interband coupling regime, enhances interactions between electrons from the LLL and the second LL and affects the electron–phonon coupling process, and these phenomena taken together may lead to an instability in the system that has an effect on the transport properties. The observed oscillating instabilities (wiggles) at $B \approx 15$ T can be attributed to the superimposition of two effects: electron–phonon coupling and enhanced electron interactions.

The electron–phonon effect and redistribution of heavy electrons results in an increase in the degeneracy of two equivalent ellipsoids B and C and the formation of Landau sublevels. In particular, the splitting of each electron level into few sublevels was predicted by theoretical calculations for a magnetic field oriented in the bisector–trigonal plane [20]. The calculated angular dependences of the magnetic field at which the electron LLs cross the Fermi energy level indicate a possible crossing of the Fermi level by the 0_e^+ Landau sublevel of heavy electrons in a magnetic field close to 20 T. The above examined ideas about the influence of the electron–phonon effect, redistribution of heavy electrons and splitting of the LLL electron level into a few sublevels do not contradict each other and allow for the understanding of an anomalous high-field peak in the frame of the one-particle picture.

Thus, the unknown peak X with a positive sign of the jump in the MR and with a negative sign in the MTEP dependences (Figs. 3a, 3b) in a magnetic field of 19.5 T can be identified with the crossing of the Fermi energy level by the one of the spin-polarized lowest Landau sublevels of heavy electrons that should be shifted to a high magnetic field with an increase in their QL under an applied strain (Figs. 3b–3d). In this context, we may speculate on the attribution of

unusual wiggles and the unidentified peak X in the MR and MTEP dependences to the complex structure of the LLLs of heavy electron pockets in a high magnetic field.

In our explanations, we have not discussed the assumption of the effect of the surface states on the transport in bismuth since we fully share the Comment on 'Signatures of Surface States in Bismuth at High Magnetic Fields' [16]. As concerns Bi wires, a manifestation of the surface states may be possible in thin nanowires with $d < 100$ nm. Our Bi wires with $d > 200$ nm exhibit bulk-like properties.

Finally, the magnetic field position of peak X is reproduced for wires with $d = 0.2–2.0$ μm without showing a dependence on the limiting size indicating their bulk origin. Moreover, the magnitude of the unidentified peak X is larger for the more structurally perfect wires of larger diameters $d = 1.0–2.0$ μm, where phonon drag effect is dominant in the thermopower. Further, the MTEP peak at 19.5 T persists up to a temperature of 10 K, where quantum oscillations from holes are smeared. Detailed results of investigations of MTEP in temperature ranges of 4.2 – 20 K where the phonon drag effect is dominant may be the subject of another paper.

3. Conclusions

Measurements of the longitudinal magnetoresistance in a pulsed magnetic field of up to 35 T with the orientation along the bisector axis have revealed some anomalies in a magnetic field above the QL of the electrons: a sharp peak of MR at 33 T and some oscillating instabilities in a magnetic field below 20 T.

Investigation of MR under uniaxial strain has revealed that the sharp peak of the MR is reproduced in lower magnetic fields at 28 T according to a decrease in the light electron concentration under strain. The Lifshitz ETT was recorded at a strain of 1.1% in the result of the vanishing of the light electron ellipsoid. Since the MR peak detected in the strained wire fades after the Lifshitz ETT, we suppose that the MR peaks at 33 and 28 T have the same origin, which is attributed to the crossing of the Fermi level by the LLL of light electrons. The present conclusions are consistent with the previous assumption [15] based on the model of Vecchi et al. [14] which implies a "camel-back" structure in the k_H dispersion of the LLL for light electrons. Thus, a correlation between the exit of the LLL of light electrons and the Lifshitz transition has been found. The result is that the critical magnetic field of the ETT has decreased; thereby, the magnetic field range of occurrence of magnetic-field-induced instabilities associated with the LLLs of electrons has been extended.

The investigation of MR and Seebeck coefficient under the simultaneous action of a strain and a magnetic field has revealed a modification of the electronic structure where the QL for light and heavy electrons changes in different ways: QL_L of the light electrons decreases with a decrease in their concentration owing to the transfer to two equivalent ellipsoids of heavy electrons, while QL_H of the heavy electrons moves to a high magnetic field.

The observed correlation between the shift of QL_H of heavy electrons to a high magnetic field and the position of the MR anomalies (wiggles followed by an unidentified peak at 19.5 T) suggests that these effects can be attributed to the crossing of the Fermi level by the one of lowest Landau sublevels of heavy electrons that should be shifted to a high magnetic field with an increase in their QL. In this context, we may speculate on the attribution of the wiggles (oscillations) and the unidentified peak in the MR and MTEP dependences to the complex structure of the LLLs of heavy electron pockets in a higher field.

It should also be noted that a decrease in the resistance in higher fields with the apparent metallization of bismuth indicates possible changes in the mechanism of carrier scattering [2, 21]

associated also with the Lifshitz transition and with the substructure of the LLL of electrons.

The observed anomalies in the MR in a high magnetic field have been explained in terms of well-known models of the energy spectrum for bulk Bi additionally considering the performed theoretical calculations [5, 10, 11, 13, 20, 21]. Note that it cannot be ruled out that the observed anomalies may have a more exotic origin, which requires accurate theoretical calculations in the future. Some refinements on the contribution of electrons or holes to the anomalies in magnetotransport will be obtained through future experimental measurements of the Seebeck effect in a high magnetic field of up to 35 T.

Acknowledgments. This work was supported by a Polish-Moldovan bilateral project (PAN-2014-2016). The author acknowledges the support from EuroMagNET under the EU contract for access to the High Field Magnet Laboratory and Institute for Molecules and Materials, Radboud University in Nijmegen.

References

[1] N. Miura, K. Hiruma, G. Kido, and S. Chikazumi, Phys. Rev. Lett. 49, 1339, (1982).
[2] N. B. Brandt, E. A. Svistova, and G. Kh. Tabieva, Pis'ma Zh. Eksp. Teor. Fiz. 4 27, (1966).
[3] D. Yoshioka, J. Phys. Soc. Jpn. 45, 1167, (1978).
[4] K. Behnia K, L. Balicas, and Y. Kopelevich, Science 317, 1729, (2007),
[5] Z. Zhu, B. Fauque, Y. Fuseya, and K. Behnia, Phys. Rev. B 84 115137, (2011).
[6] Z. Zhu, B. Fauque, L. Malone, A.B. Antunes, Y. Fuseya, and K. Behnia , Proc. Nat. Acad. Sci. USA, 102 14813, (2012).
[7] R. Kuechler, L. Steinke, R. Daou, M. Brando, K. Behnia and F. Steglich, Nat. Mater. 13, 461, (2014).
[8] B. Fauque, B. Vignolle, C. Proust, J-P. Issi, and K. Behnia, New J. Phys. 11, 113012, (2009).
[9] X. Du, S-W. Tsai, D. L. Maslov, and A. F. Hebard, Phys. Rev. Lett. 94, 166601, (2005).
[10] A. Collaudin, B. Fauqué, Y. Fuseya, W. Kang, and B. Kamran, Phys. Rev. X 5, 021022, (2015).
[11] G. P. Mikitik and Yu. V. Sharlai, Phys. Rev. B 91, 075111, (2015).
[12] L. Li, J. G. Checkelsky, Y. S. Hor, C. Uher, A. F. Hebard, R. J. Cava, and N. P. Ong, Science 321, 547, (2008).
[13] Yu.V. Sharlai and G. P. Mikitik, Phys. Rev. B 79, 081102(R), (2009).
[14] G. E. Smith, G. A. Baraff, and J. W. Rowell, Phys. Rev. 135, A1118, (1964).
[15] B. Seradjeh, J. Wu, and P. Phillips, Phys. Rev. Lett. 103**,** 136803, (2009).
[16] K. Behnia, Phys. Rev. Lett. 104, 059705, (2010).
[17] Chuan Li, A. Kasumov, A. Muran, Shamashis Sengupta, F. Fortuna, K. Napolskii, D. Koshkodaev, G. Tsirlina, Y. Kasumov, I. Khodos, R. Deblock, M. Ferrier, S. Guéron, and H. Bouchiat, Phys. Rev. B 90, 245427, (2014).
[18] K. Hiruma, G. Kido and N. Miura, Solid State Commun. 31, 1019, (1979).
[19] M. P. Vecchi, J. R. Pereira and M. S. Dresselhaus, Proc. Int. Conf. Phys. Semicond. (Stuttgart, 1974) (Edited B. G. Teubner, Stutgart, 1974, 1181p.
[20] M. P. Vecchi, J. R. Pereira and M. S. Dresselhaus, Phys. Rev. B 14, 298, (1976).
[21] J. Alicea and L. Balents, Phys. Rev. B 79, 241101, (2009).
[22] Yu. V. Sharlai and G.P. Mikitik, Phys. Rev. B 83, 085103, (2011).

[23] D. Balla and N. B. Brandt, Zh. Eksp. Teor. Fiz. 47, 1653, (1964); D. Balla and N.B. Brandt, Sov. Phys. JETP. 20, 1111, (1965).
[24] I. M. Lifshitz, Zh. Eksp. Teor. Fiz. 38, 1569, (1960); I.M. Lifshitz, Sov. Phys. JETP. 11, 1130, (1960).
[25] N. B. Brandt, V. A. Kul'bachinskii, N. Ya. Minina, and V. D. Shirokikh, Sov. Phys. JETP. 51, 562, (1980).
[26] Yu. P. Gaidukov, Sov. Phys.-Usp. 27, 256, (1984); Yu.P. Gaidukov, Usp. Fiz. Nauk. 142, 571, (1984).
[27] E. Condrea and A. Nicorici, Solid State Commun. 150, 118, (2010).
[28] E. Condrea, A. Nicorici, A. Gilewski, S. Matyjasik, J Low Temp. Phys. 174, 232, (2014).
[29] M. Hagiwara and A. Inoue, Production Techniques of Alloy Wires by Rapid Solidification in Rapidly Solidified Alloys, ed. H H Liebermann (New York: Dekker), 1993, 141p.
[30] A. D. Grozav and E. Condrea, J. Phys.: Condens. Matter 16, 6507, (2004).
[31] N. B. Brandt, D. V. Gitsu, V. A. Dolma, Yu. A. Ponomarev, Sov. Phys. JETP 65, 515, (1987); N. B. Brandt, D. V. Gitsu, V. A. Dolma, Yu. A. Ponomarev, Zh. Eksp. Teor. Fiz. 92, 913, (1987).
[32] R. G. Chambers, Proc. R. Soc. London, Ser. A 202, 378, (1950).
[33] V. S. Edelman, Adv. Phys. 25, 555, (1976).
[34] P. B. Littlewood, B. Mihaila, and R.C. Albers, Phys. Rev. B 81, 144421, (2010).

ENGINEERING MICROWAVE PROPERTIES OF MICROWIRES

S. A. Baranov [1, 2]

[1]*Institute of Applied Physics, Academy of Sciences of Moldova, Academiei str. 5, Chisinau, MD-2028 Republic of Moldova*

[2]*Département de Génie Physique, École Polytechnique de Montréal, C.P. 6079, succ. Centre-ville, Montréal H3C 3A7, (Québec) Canada*

(Received December 04, 2014)

Abstract

A correlation between the frequency of natural ferromagnetic resonance (NFMR) (1−12 GHz) determined from the dispersion of permeability and alloy composition (or magnetostriction between 1 and 40 ppm) of glass-coated microwires has been systematically confirmed. Absorption of composite (microwire pieces embedded in a polymer matrix) screens has been experimentally investigated. Parallel theoretical studies suggest that a significant fraction of the absorption can be ascribed to a geometrical resonant effect, while a concentration effect is expected for the thinnest microwires.

Keywords: Amorphous magnetic microwires; Ferromagnetic resonance; Natural ferromagnetic resonance, high frequency properties

1. Introduction

Microwave engineering is of great importance in a wide spectrum of applications most of which are related to wireless telecommunications systems, such as telephone, broadcast satellite television, or satellite global positioning. Radar systems are also very useful for detecting mobile targets in air, sea, or ground, for air-traffic control or missile tracking radars, and for a wide variety of remote sensing systems. In addition, resonance phenomena appearing at microwave frequencies offer an opportunity for novel applications in heating systems, medical diagnosis and treatment or just new effects in basic science. In all these cases, the involved phenomena are characterized by millimeter electromagnetic waves with frequencies in a range of 300 MHz to 300 GHz.

The search for materials exhibiting outstanding properties in this frequency range is thus relevant in the development of the mentioned applications. Here, we focus on a particular family of materials, i.e., glass-coated amorphous magnetic microwires, exhibiting an exciting microwave behavior with enormous technological applications as elements for absorption of electromagnetic radiation.

Glass-coated magnetic microwires are characterized by a nucleus of a magnetic alloy, a structurally amorphous and metallic conductor, with a diameter between 2 and 20 μm, covered by a Pyrex-like coating with a thickness of 2−10 μm. They are prepared by quenching and drawing rapid solidification method, following the early Taylor technique later modified by Ulitovsky [1−4]. The coating, in addition to insulating the metallic nucleus from corrosion and electrical viewpoints, induces strong mechanical stresses in the nucleus, which, coupled with its

magnetostriction, determine strong magnetoelastic anisotropy, in the origin of a unique magnetic behavior. Particularly, magnetic bistability characterized by a square low-field loop with a single giant Barkhausen jump is observed in magnetostrictive Fe-rich microwires [4, 5]. Alternatively, non-magnetostrictive Co-base microwires exhibit giant magnetoimpedance (GMI) effect, which originates in the electromagnetic classical skin-effect, observed in the radio frequency range [6−8]. GMI has been also correlated to ferromagnetic resonance phenomena appearing typically in the microwave frequency range [8]. In addition, glass-coated microwires also show interesting electromagnetic absorption properties as shown through different techniques like wave-guide experiments, through the scattering and the transmission coefficients, and in general the ferromagnetic-resonance (FMR)and antiferromagnetic-resonance (AFMR) behavior. Of particular interest is the natural ferromagnetic resonance (NFMR) observed as a consequence of a strong intrinsic magnetoelastic anisotropy.

The technological use of high and ultra-high frequencies in engineering has led to the need of creating electromagnetic protective screens. Amorphous microwires can be thus employed as radio-absorption elements when embedded in suitable matrices. Here, we introduce an analysis of the opportunity of application of these materials in composite protective screens.

2. Production and properties

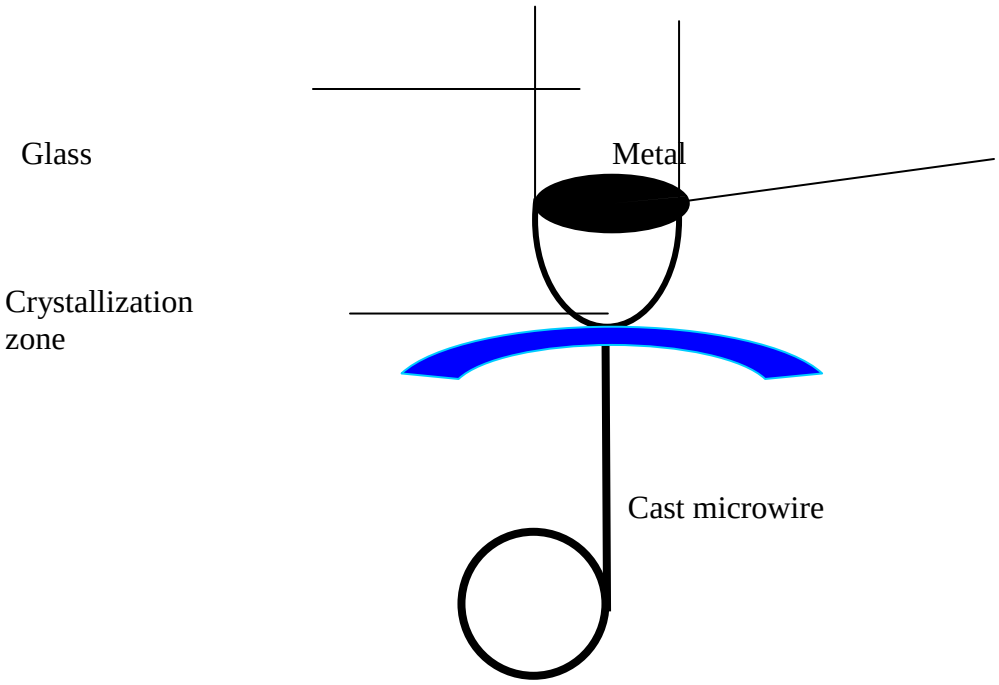

Fig. 1. Taylor−Ulitovsky method for fabrication of microwires.

Cast glass-coated amorphous magnetic microwires are produced by the Taylor−Ulitovsky method (see [1–4] and Fig. 1). The alloy is heated in an inductor up to the melting point. The portion of the glass tube adjacent to the melting metal softens and envelopes the metal droplet. Under suitable conditions, the molten metal fills the glass capillary and a microwire is thus formed with the metal core completely covered by a glass shell.

The microstructure of a microwire depends mainly on the cooling rate, which can be

controlled when the metal-filled capillary enters a stream of cooling liquid in its way to the receiving coil. Critical quenching rates (10^5–10^7 K/s) for fabrication of amorphous materials can be obtained.

The glass coating of the cast amorphous magnetic microwires, in addition to protecting the metallic nucleus from corrosion and providing electrical insulation, induces large mechanical stresses in the nucleus. Coupled with its magnetostriction, these factors determine its magnetoelastic anisotropy, at the origin of a unique magnetic behavior. The residual stresses are the result of differences in the coefficients of thermal expansion of the metal and the glass. A simple theory for the distribution of residual stresses was presented in [2,3]. In cylindrical coordinates, the residual tension is characterized by axial, radial, and tangential components which are independent of the radial coordinate. The value of these stresses depends on the ratio of radius r of the metallic nucleus to total microwire radius R:

$$x = \left(\frac{R}{r}\right)^2 - 1,$$

$$\sigma_r = \sigma_\phi = P = \sigma_0 \frac{kx}{\left(\frac{k}{3}+1\right)x + \frac{4}{3}},$$

$$\sigma_z = P\frac{(k+1)x+2}{kx+1}, \qquad (1)$$

where $\sigma_0 = \varepsilon E_1$; ε is the difference between the thermal expansion of the metallic core and that of the glassy cover with expansion coefficients α_1 and α_2: ($\varepsilon = (\alpha_1 - \alpha_2)(T^* - T)$); E_1 is the Young's modulus of the metal core, T^* is the solidification temperature of the composite in the metal/glass contact region ($T^* \sim$ 800–1000 K), T is the room temperature ($\varepsilon E_1 \sim 2GPa$ is the maximum stress in the metallic core).

Technological parameter k is the ratio of Young's moduli of the glass and the metal ($k = E_2/E_1 \sim 0.3$–0.6). Numerical calculation indicates that, for small values of x, the dependence $\sigma_z(x)$ is almost linear and reaches saturation (up to 1GPa) at about $x = 10$:

$$\sigma_z \sim (2 \div 3)P > \sigma_r,$$

$$(P \to 0{,}5\sigma_0 \sim 1\ GPa)$$

The general theory of residual tension is presented in [5] where other calculations of residual tension are criticized. Here, we further analyze the case where the depth of the skin layer is less than nuclear radius r. In this case, Eq. (1) provides a good description of experiment (see below, Eqs. (11)–(13) and Figs. 2–4).

For materials with positive magnetostriction, the orientation of the microwire magnetization is parallel to the maximal component of the stress tensor, which is directed along the axis of the wire (see [1–3]). Therefore, cast Fe-based microwires with positive magnetostriction constant show a rectangular hysteresis loop with a single large Barkhausen jump between two stable magnetization states and exhibit the phenomenon of NFMR (see [1–3]).

The FMR method is often used for the investigation of amorphous magnetic materials (ribbons, wires, thin films). Both macroscopic and microscopic heterogeneity of amorphous

materials can be investigated by FMR. Residual stress is an important parameter for amorphous materials which can be studied by FMR (see [1−3]).

FMR is also used for diagnostics of the uniformity of amorphous materials. Extrinsic broadening of FMR lines due to fluctuations of the anisotropy, magnetization, and exchange-interaction constant in amorphous materials has also been investigated. Microwave experiments are very useful for investigation of spin-wave effects. In particular, microwave generation and amplification are of great interest. Investigation of structural relaxation of amorphous materials during heat treatment using FMR is also important. Differential FMR curves combined with hysteresis curves can give important information in this case.

In the present work, cast glass-coated amorphous microwires with metallic cores and diameters of 0.5−25 μm were considered. The amorphous structure of the core was investigated by X-ray methods. The thickness of the glass casing varied between 1 and 20 μm. Using microscopy, samples with the most ideal form and with lengths of about 3−5 mm were selected for investigation. Microwires based on iron, cobalt, and nickel (doped with manganese), with additives of boron, silicon, and carbon were studied. Microwires made of different materials have diverse magnetostriction. We studied microwires from the same spool whose glass casing was removed by etching in hydrofluoric acid.

In almost all cases, standard FMR spectrometers of 2−32 GHz were used. The magnetic field was measured using a Hall sensor (with an accuracy within 0.1%). In addition, magnetometer measurements determined the magnetization needed for calculation.

The basic measurements were made in a longitudinal field configuration (the external magnetic field was directed along the microwire axis). In this case, a signal of a correct form was obtained from good samples. This gives the possibility of measuring resonant-curve width.

For thick cores, skin effect must be taken into account. In this case, the resonant frequency was described by the Kittel formula for a plane (with longitudinal magnetization). The *g* factor was estimated at two resonant frequencies as ~ 2.08 ÷ 2.1 on average. Our results are in good agreement with literature data on the *g* factor for amorphous materials (see[1−4, 6−8]). In a transverse field (when the external field is perpendicular to the microwire axis), the signal was weak or not observed in samples with negative magnetostriction. It is obvious that the presence of this signal is associated with non-uniformity of the high-frequency demagnetizing factor.

A microwire was considered to be a ferromagnetic cylinder with small radius *r*. To characterize it, we introduce following parameters.

1. The depth of the skin layer is:

$$\delta \sim [\omega(\mu\mu_0)_e \Sigma]^{-1/2} \sim \delta_0(\mu)_e^{-1/2}, \quad (2)$$

$(\mu\mu_0)_e$ is the effective magnetic permeability, and Σ is the electric conductivity of the microwire. In the case of our magnetic microwires, with the relative permeability ıμ eht fo ecnanoser raen ı order 10^2, (ω~8–10GHz) δ changes from1 to 3μm.

2. The size of the domain wall (according to Landau−Lifshits theory) is

$$\Delta_{LL} \sim (A/K)^{1/2} \sim 10–0.1\mu m, \quad (3)$$

where *A* is the exchange constant and *K* is the anisotropy energy of the microwire ($K \sim \lambda\sigma$, where λ is the magnetostriction constant and σ is the effective residual stress from the fabrication

procedure (see [2, 3] and Eq. (1)). The full theory gives $\Delta_f \sim 0.1$ μm for the size of the domain wall of glass-coated microwires (see [5]).

3. The radius of a single domain (according to Brown theory) is

$$a \sim A^{1/2} / M_S \sim 0.1\text{–}0.01\mu\text{m}, \tag{4}$$

Where M_s is the saturation magnetization of microwire.

According to [2, 3], the frequency of the NFMR is

$$\left(\frac{\omega}{\gamma}\right)^2 = (H_e + 2\pi M_S)^2 - (2\pi M_S)^2 \exp(-2\delta / r), \tag{5}$$

Where γ is the gyromagnetic ratio ($\gamma \sim 3$ MHz/Oe). The anisotropy field is $H_e \sim 3\lambda\sigma/M_s$ (for exact calculations of anisotropy field, see below).

If $r<\delta$, we have

$$\frac{\omega}{\gamma} = H_e + 2\pi M_S . \tag{6}$$

If $r>\delta$, the NFMR frequency is given by (see [1−3])

$$\left(\frac{\omega}{\gamma}\right)^2 = H_e(H_e + +4\pi M_S) . \tag{7}$$

The discovery of NFMR in amorphous microwires [3] was preceded by the study of the wires using standard FMR methods [4]. Then, a shift in the resonant field due to core deformation of the microwire associated with fusing of the glass and the core at the temperature of microwire formation was observed. The FMR line width is also of interest because it characterizes, in particular, the structural parameters [2, 3].

Since the skin penetration depth of a microwave field in a metallic wire is relatively small in comparison with its diameter, the resonant frequency of FMR can be determined by means of Kittel formula (Eqs. (6)−(8)). Taking into account the magnetoelastic stress field [2, 3], for a thin film magnetized parallel to the surface, we can obtain

$$\left(\frac{\omega}{\gamma}\right)^2 = (H + (N'_Z - N'_X)M_S + 4\pi M_S) \times (H + (N'_Z - N'_Y)M_S) , \tag{8}$$

Where H is the FMR field; N'_X, N'_Y, N'_Z are the components of tensor of effective demagnetizing factors in the case of magnetoelastic stress:

$$N'_i = \frac{3|\lambda|\sigma i}{2M_S^2}\left(\cos^2\theta i - \frac{1}{3}\right); \tag{9}$$

where

$\theta_1 = \theta_2 = 90^\circ, \theta_3 = 0.$

Components σ_i (see Eqs. (1)) are residual stresses (see [2, 3]). Then,

$$N'_X = N'_Y = -\frac{|\lambda| P}{2M_S^2};$$
$$N'_Z = \frac{|\lambda| P}{2M_S^2}\frac{(k+1)x+2}{kx+1}; \tag{10}$$

Substituting the σ_i values obtained in our previous work [2,3] (see Eqs. (1)), and taking into account Eqs. (8) and (9), we can calculate conditions for FMR:

$$\left(\frac{\omega}{\gamma}\right)^2 = \left[H + \frac{(3|\lambda|P)}{2M_S}\frac{x\left(k+\frac{2}{3}\right)+\frac{5}{3}}{kx+1} + 4\pi M_S\right] \times \left[H + \frac{(3|\lambda|P)}{2M_S}\frac{x\left(k+\frac{2}{3}\right)+\frac{5}{3}}{kx+1}\right] . \tag{11}$$

.

If the glass is removed, the stress is completely removed. Then the FMR resonant field of wire without glass casing H_0 is determined from

$$\left(\frac{\omega}{\gamma}\right)^2 = H_0(H_0 + +4\pi M_S) \tag{12}$$

We have shown (see [1−4, 6−8]) that these relations quantitatively explain all of the basic features of NFMR and FMR. Note that the value of M_S required for the calculations was determined both by standard methods on a vibration magnetometer and with the use of interpolation formulas given here. The error relative to tabular values for the given alloys is not greater than 5%.

For the frequency of NFMR under the simple approximation taking $\varepsilon E_1 \sim$ 2GPa and $k \sim$ 0.4, this formula can be written as

$$\omega(GHz) \approx \omega o\left(\frac{0.4x}{0.4x+1}\right)^{1/2}$$
$$\omega o(GHz) \approx 1{,}5(10^6\lambda)^{1/2}, \tag{13}$$

It is evident that the dependence for the frequency of NFMR (Eqs. (13), and Figs. 2, 3) is determined from two typical values x, λ.

The basic contribution to the NFMR frequency and NFMR line width is due to the effective magnetostriction and parameter x (Eqs. (13), and Figs. 2, 3, 5). The residual stress in the microwire plays the dominant role in the formation of the absorption line width, as will be shown

below (Figs. 5, 6).

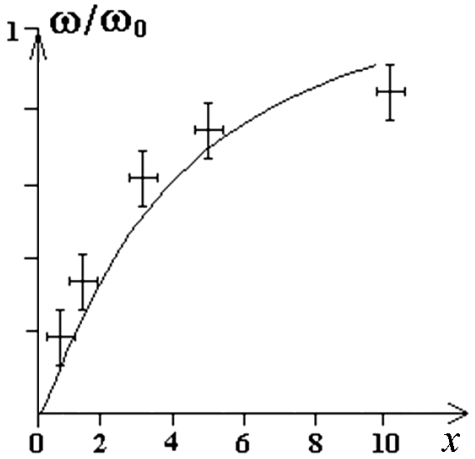

Fig. 2. Theoretical curve of NFMR frequency as a function of x (according to Egs. (11)–(13)) and experimental data (see [2, 3]).

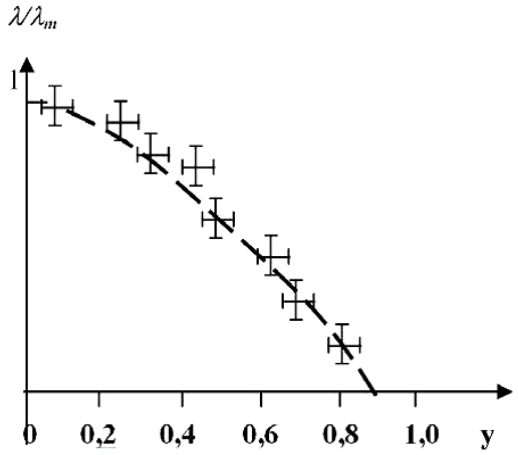

Fig. 3. Dependence of relative magnetostriction λ/λ_m for alloy composition $(Co_y\ Fe_{1-y})_{75}(BSiC)_{25}$ series cast glass-coated amorphous magnetic microwires according to Eqs. (11)–(13), where y = Co/(Co+Fe) (see [2, 3]).

When the penetration depth of the microwave field in the metallic wire is small relative to the wire diameter (on account of the skin effect), the resonant frequency in FMR and NFMR can be determined by means of Eqs. (1). (The general theory of residual tension is presented in [5]; however, here it is enough to use the simple theory from [2, 3]).

Substituting typical values of λ and x in Eq. (13), we reach numerical values of NFMR in a range of 1−12 GHz. A systematic study on the NFMR frequency for the alloy series $(Co_yFe_{100-y})_{75}(BSiC)_{25}$ has been performed as a function of the Co content (Fig.3). The magnetostriction has then been evaluated using Eq. (13). The result is plotted in Fig. 3 which shows good agreement with the magnetostriction values as determined through conventional techniques (Fig.4. according to [9]). Thus, the final theory quantitatively explains all the basic

features of NFMR and FMR. However, the area of experimental research in the case of a small radius of the metallic nucleus of a microwire remains vacant.

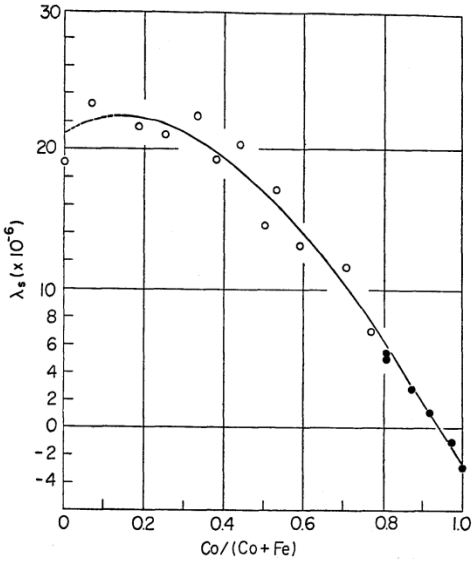

Fig. 4. Typical saturation magnetostriction λ_s in the amorphous Co–Fe alloys: ○ $(Fe_{1-y}Co_y)_{80}(PC)_{20}$; ● $(Fe_{1-y}Co_y)_{75}(SiB)_{25}$ (according to [9]).

3. Radio-absorption shielding

NFMR occurs when the sample is submitted to a microwave field without application of any biasing field other than the intrinsic anisotropy field of the microwire.

Near the NFMR frequency, the dispersion of permeability μ given by

$$\mu(\omega) = \mu'(\omega) + i\,\mu''(\omega), \tag{14}$$

exhibits a peak in μ" and a zero crossing of μ' .

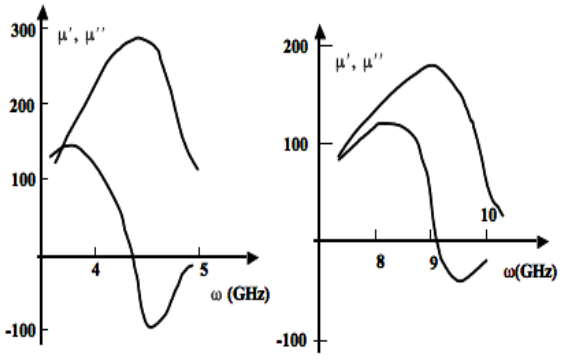

(a) (b)

Fig. 5. Real and imaginary relative permeability components around NFMR for $Co_{59}Fe_{15}B_{16}Si_{10}$ (a) and $Fe_{69}C_5B_{16}Si_{10}$ (b) microwires (r~ 5 μm, x > 8 (see [10])).

Figures 5a and 5b show resonance frequencies of 4.4 and 9.0 GHz and resonance widths

of 1 and 0.5 GHz for two compositions. Near resonance μ" is expected to be described by

$$\mu''/\mu_{dc} \sim \Gamma\Omega / [(\Omega - \omega)^2 + \Gamma^2], \quad (15)$$

where μ_{dc} is static magnetic permeability and Γ is the width of the resonant curve. Very near resonance, when $\Gamma > (\Omega - \omega)$, Eq. (15) reduces to

$$\mu''/\mu_{dc} \sim \Omega / \Gamma \sim 10–10^2.$$

Note that, in Fig. 5a, the imaginary component is rather symmetrically distributed around the resonance frequency. This is due to the symmetric distribution of the circular permeability in the near surface layer within the penetration depth. In contrast, in Fig. 5b, the imaginary component shows a non-symmetric feature around the resonance frequency. This can be attributed to the inhomogeneous pattern of permeability in the region close to the surface of the microwire where metastable phases occur, as demonstrated by X-ray studies.

Monitoring the geometry of the microwire (i.e., its diameter) and the magnetostriction through its composition makes it possible to prepare microwires with tailorable permeability dispersion for designing radio-absorption materials:

(i) Determining the resonant frequency in a range of 1−12 GHz;

(ii) Controlling the maximum of the imaginary part of magnetic permeability.

High-frequency properties, pieces of microwires have been embedded in planar polymeric matrices to form composite shielding for radio absorption protection. Experiments have been performed employing commercial polymeric rubber with a thickness of about 2−3 mm. Microwires are spatially randomly distributed within the matrix before its solidification. Concentration is maintained below 8−10g of microwire dipoles (1−3mm long) per 100g of rubber [11]. A typical result obtained in an anechoic chamber is shown in Fig. 6 for a screen with embedded $Fe_{69}C_5B_{16}Si_{10}$ microwires. As observed, an absorption level of at least 10 dB is obtained in a frequency range of 8−12 GHz with a maximum attenuation peak of 30 dB at around 10 GHz. In general, optimal absorption is obtained with microwires with metallic nuclei of diameter $2r$ = 1−3 μm (2R ~ 20μm (x > 10)) and length L = 1−3 mm. These pieces of microwires can be treated as dipoles whose length L is comparable to the half value of the effective wavelengths $\Lambda_{eff}/2$ of the absorbed field in the composite material (i.e., in connection to a geometric resonance).

Figure 6 also shows how the frequency absorption spectrum of shielding with $Fe_{69}C_5B_{16}Si_{10}$ microwires changes when it is rotated (90º each spectrum).

We attribute the changing attenuation to the lack of perfect angular distribution of microwires whose length does not always fit within the shielding thickness.

The effect does not even have mirror symmetry. (The measurement error was less than 10% for the frequency, and while the spread of the attenuation factor was 5 dB).

Small fluctuations in concentration of dipoles at a concentration of dipoles near the percolation threshold can lead to fluctuation of the absorption curve. Similar results were presented in [12].

As observed, both frequency dependences (Figs. 5b and 6) are similar except for the half-width value of the permeability.

Although the design of absorption shielding can be based on disposing the dipolar pieces in a stochastic way, we consider, for simplicity, a theoretical analysis for a diffraction grating

with spacing between wires Q < Λ (Λ is wavelength of absorbed field). (Another simple example is in Appendix A).

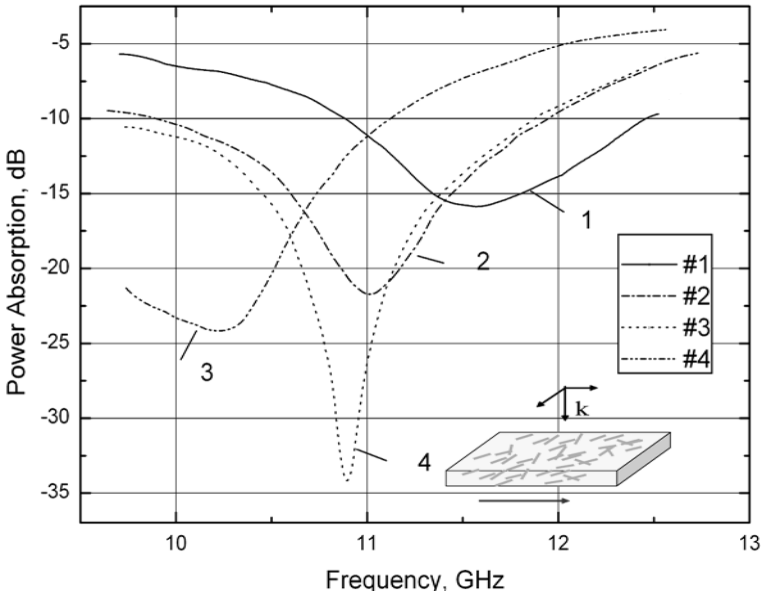

Fig. 6. Absorption characteristics of shielding by a microwire composite with NFMR in the HF-field in a frequency range of 10−12 GHz. Curve 1 represents an initial situation of the screen; (2−4): the screen is turned by 90° about a perpendicular axis each time.

The propagation of an electromagnetic wave through absorption shielding with microwire-based elements is characterized by transmittance $|T|$ and reflectance $|R_r|$ coefficients given by

$$|T| = (\alpha^2 + \beta^2)/[(1+ \alpha)^2 + \beta^2];$$

$$|R_r| = 1/[(1+ \alpha)^2 + \beta^2], \quad (16)$$

where $\alpha=2X_r/Z_0$, and $\beta=2\ Y/Z_0$, with $Z_0=120\pi/Q$, and the complex impedance $Z= X_r + iY$.

Absorption function *G*is correlated with the generalized high-frequency complex conductivity Σ (or high-frequency impedance *Z*).

Here, we use the analogy between the case of a conductor in a waveguide and that of a diffraction grating. The absorption function, given by

$$|G| = 1 - |T|^2 - |R_r|^2 = 2\alpha / [(1+ \alpha)^2 + \beta^2] \quad , \quad (17)$$

has a maximum

$$|G_m|=0.5 \geq |G|,$$

for simultaneous $\alpha=1$ and $\beta=0$, for which
$|T|^2 = |R_r|^2 =0.25$.

The minimum $|G|=0$ occurs at $\alpha=0$, β of any positive number).

Theoretical estimations taking into account only the active resistance of microwires result in attenuation within a range of 5−15 dB being much lower than experimental results, which for spacing of microwires Q =10^{-2} m ranges between 18 and 15 dB, while for a spacing Q = 10^{-3} m it increases up to 20−40 dB. Thus, it becomes clear that shielding exhibits anomalously high absorption factors, which cannot be explained solely by the resistive properties of microwires.

The high-frequency conductivity Σ_m of a stochastic mixture of microwires in the polymeric matrix can be expressed as a function of conductivities Σ_i of non-conducting (polymeric matrix) and conducting (microwire) elements, denoted by subscripts 1 and 2, respectively, as follows [13]:

$$\Sigma_m = B + (B^2 + A\,\Sigma_1\,\Sigma_2)^{1/2}, \qquad (18)$$

where

$$B=1/2\{[\Sigma_1(X_1-AX_2)+\Sigma_2(X_2-AX_1)]\};$$

X_i is the fractional volume:

$$(X_1+X_2)=1;$$

$$A=1/(J_1-1), \text{ with } \quad J_1\sim (J+Y/X_r)$$

being the fractal dimension of the system (J is the geometrical dimension of the system) and

$$Y/X_r \sim (r/\delta)^2.$$

Figure 7 shows that, in case of a thick microwire ($r > \delta \approx 1\mu m$), the conductivity of the system becomes very high, even in case of a low microwire concentration, indicating the case of an antenna resonance as reported in [11].

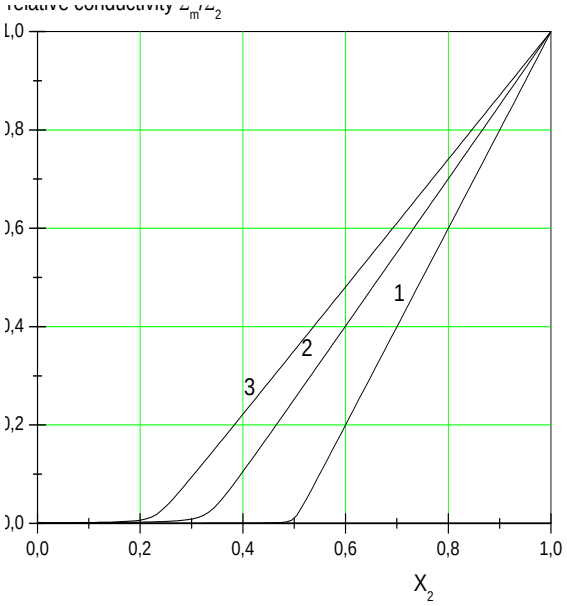

Fig. 7. Generalized conductivity calculated using Eq. (18) for $\Sigma_2 / \Sigma_1 \sim 10^4$: (*1*) thin microwire ($r < \delta$ ~1 μm) J = 2, Y = 0; (*2*) thin microwire ($r < \delta$ ~ 1 μm) J = 3, Y = 0; and (*3*) thick microwire ($r > \delta$ ~1 μm) J_1 = 4, Y/X_r = 1.

Let us consider the effective absorption function (as in Eq. (17))**:**

$$|G_{eff}| \sim \Gamma_{eff}\, \Omega_{eff}/\, [(\Omega_{eff} - \Omega)^2 + \Gamma_{eff}^2], \tag{19}$$

where $\Gamma_{eff} \geq \Gamma$ (see Eq. (12)) and $\Omega \sim \Omega_{eff}=2\pi c/\Lambda$.
A microwave antenna will resonate when its length, L, satisfies

$$L \sim \Lambda/\, 2(\mu_{eff})^{1/2}. \tag{20}$$

The maximum absorption (see Fig. 6) occurs for $\Omega_{eff} \sim 10$ GHz ($\Lambda \sim 3$ cm) and $\mu_{eff} \sim 10^2$, (according to Fig. 5). This corresponds to

$$L \sim 1.5–2 \text{ mm}, \tag{21}$$

where the microwire concentration (see Fig.7) $X_2<0.2$) is much less than the percolation threshold. A greater concentration of dipoles increases absorption, $|G_{eff}|$, but also increases reflectance, $|R_{r1}|$, which can be simply evaluated to be [14]:

$$|R_{r1}| \sim 1 - 2\sqrt{(\Omega/2\pi\Sigma_m)}, \tag{22}$$

Where $\Omega/2\pi \sim 10^{10}$ Hz.

The formula is applicable, and calculation of small reflectance, $|R_{r1}|$ is possible, only if

$$\Sigma_m \sim 10^{11} \text{Hz},$$

for concentration below the percolation threshold (as $\Sigma_2 \sim 10^{15}$Hz).

Thus, for very thin microwires (i.e., thinner than 1 μm in diameter) embedded in a composite matrix with concentration larger than the percolation level $X_2 \sim 0.2$, a noticeable absorption effect should be expected.

4. Conclusions

The microwave electromagnetic response has been analyzed for a composite consisting of dipoles of amorphous magnetic glass-coated microwires in a dielectric. This material can be employed for radio absorbing screening. The spontaneous NFMR phenomena observed in glass-coated microwires has opened the possibility of developing novel materials with broad-band of radio absorbing materials.

Acknowledgments. This research received financial support from the Department of Engineering Physics *École Polytechnique de Montréal.* The author thanks A. Yelon and D. Menard for their participation in discussions of the results.

Appendix A

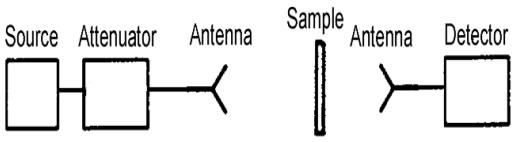

It is well known, that the simple model of contact of vacuum with the absorbing material gives the following equations [14] (the general theory is presented in [15]; see also [16]):

$$1+ R_r = T, \tag{A. 1}$$

$$(\alpha+i\,\beta)(1- R_r)= T;$$

that gives

$$R_r = \frac{1-\alpha-i\beta}{1+\alpha+i\beta}, \tag{A. 2}$$

and at β =0 , α =1 ,we find

$$R_r = 0. \tag{A. 3}$$

From these findings, it is possible to obtain a simple criterion for matching the vacuum with a radio absorbing material:

$$\mu_m \sim \Sigma_m / \Omega, \tag{A. 4}$$

(where μ_m is the effective magnetic permeability of the composite). This condition cannot be satisfied for composites containing amorphous magnetic wires. This fact forces us to use other physical principles for designing radio absorbing materials presented above).

We note that similar results were obtained in [16].

References

[1] A.N. Antonenko, S.A. Baranov, V.S. Larin, and A.V. Torcunov, Suppl. Mater. Sci. Eng. A 248, (1997).
[2] S.A. Baranov, V.N. Berzhansky, S.K. Zotov,V.L. Kokoz, V.S. Larin, and A.V. Torcunov, Fiz. Met. Metalloved. 67 , 73, (1989).
[3] S.A. Baranov, S.K. Zotov, V.S. Larin, andA.V. Torcunov, Fiz. Met. Metalloved. 69, 172, (1991).
[4] L. Kraus, Z. Frait, and I. Schneider, Phys. Stat. Sol. A 63, 669, (1981).
[5] S.A. Baranov,Surf. Eng. Appl. Electrochem. 47, 316, (2011).
[6] F. Yıldız, B.Z. Rameev, S.I. Tarapov,L.R. Tagirov, and B. Aktas,J. Magn. Mag. Mater. 247, 222, (2002).

[7] M. Vazquez and A.-L. Adenot-Engelvin, J. Magn. Mag. Mater. 321, 2066, (2009)
[8] D. Menard and A. Yelon, J. Appl. Phys. 88, 379, (2000).
[9] H. Fujimori, M. Kikuchi, Y. Obi, andT. Masumoto. New Co-Fe Amorphous Alloys as Soft Magnetic Materials. The 1659th report of Research Institute for Iron, Steel and Other Metals, 46 p., 1976.
[10] S. A. Baranov, J. Commun. Tech. Electron. 48, 226, (2003).
[11] S. A. Baranov, Tech. Phys. Let. 24, 549, (1998).
[12] A. P. Vinogradov, D. P. Makhnovskii, and K. N. Rozanov, J. Commun. Tech. Electron. 44, 317, (1999).
[13] S. A. Baranov, Tech. Phys. 44, 853, (1999).
[14] M. Born and E. Wolf, Principles of Optics: Electromagnetic Theory of Propagation, Interference and Diffraction of Light, Oxford–New York:Pergamon press, 1969.
[15] H.W. Bode, Network and Feedback Amplifier Design, Princeton: van Nostrand, 1945.
[16] Mingzhong Wu, Huahui He, Zhensheng Zhao, and Xi Yao,J. Phys. D: Appl. Phys. 33, 2398, (2000).

EFFECT OF TECHNOGENIC ELECTROMAGNETIC FIELDS ON EMBRYOS

A. Sidorenko, I. Shibaeva, and A. Shibaev

Gitsu Institute of Electronic Engineering and Nanotechnologies,
Academy of Sciences of Moldova

(Received September 07, 2015)

Abstract

Experiments on the exposure of dry wheat seeds to a magnetic field in a frequency range of 1–10 Hz with a flux density of 40–50 μT have shown that, in the period of active cell division, the cells of plants become more sensitive to external fields. In view of this fact, the seeds of the experimental sample show better results on germination percentage and spout length than the seeds of the reference sample against the background of natural fields under environmentally safe conditions. Under the action of technogenic electromagnetic fields, the experimental seeds showed worse results on germination percentage and sprout length than the reference seeds; this fact proves the enhancement of the negative role of these fields on the cells of the developing organism. Taking into account the general laws governing the development of organisms at the cellular level, we can assume that technogenic fields play a particular negative role for a human body at the moment of impregnation and initial development of the body when the cells of the embryo most actively respond to the surrounding fields.

1. Introduction

In the development of life throughout the Earth's history, during a long-term evolution, all existing organisms, in one way or another, have fully adapted to the various environmental conditions on our planet [1]. The living organisms have had to adapt not only to the physicochemical conditions, such as temperature, pressure, composition of the atmosphere, light, and humidity, but also to the natural fields of the Earth: geomagnetic, gravitational, electrical, and electromagnetic fields. The living organisms have evolved in an environment characterized by the presence of low-intensity electromagnetic fields, such as the Schumann waves (7.8–0.8 Hz) [2]. Everything that happens in the cells of living organisms is associated with these natural fields.

Within a relatively short historical period, the technogenic human activities have had a significant impact on natural objects and thus dramatically upset the delicate balance between the living organisms and the environmental conditions, which has been formed over thousands of years. This factor has led to many irreparable consequences, in particular, to the extinction of some animals and plants, numerous diseases, a reduction in the average duration of life of people in some regions, and infertility. In recent decades, research into the effect of natural and anthropogenic factors on the human body and other living organisms has been conducted [3].

In modern life, people are constantly being faced with the conditions in which the natural electric field of the atmosphere can be shielded or distorted by metal roofs of houses, reinforced-concrete buildings, vehicles, etc. Electric fields are absent in submarines and spacecrafts, where the plants will play an important role in the regeneration of the gas composition and the replenishment of food products in the future [4, 5]. Therefore, the biological role of natural

electric fields in the life of organisms, in particular plants, is an urgent problem.

Along with the natural fields, there are artificial technogenic fields produced by the operation of commercial frequency generators, microwave and EHF devices, transmitters, etc. In addition, the frames of reinforced-concrete buildings partially shield and partially distort natural electromagnetic fields [6, 7] and thus inflict harm to living organisms. This effect is of particular importance to growing organisms which undergo constant cell division and to the regeneration and reproduction processes in mature organisms.

In recent decades, these processes have been the subject of many scientific studies [8]. The aim of this study is to examine the respond of plant embryos to the action of low-intensity ow-frequency fields in different combinations of external fields.

It is known that exposure to low-frequency low-intensity fields has beneficial effects on seed germination and plant growth [9, 10]. In our studies of this phenomenon, we used a magnetic field with a flux density of 40–50 μT and a frequency of 1–10 Hz for the pre-germination treatment of dry seeds for 1 h. Positive results were obtained with respect to some parameters, such as seed germination, growing capacity, germination uniformity, yielding capacity, and growing season length. In addition, the differences induced by the energy component in the zone of seed treatment with a field with the above parameters were identified.

Treatment was conducted in buildings made of white ashlar limestone in environmentally safe regions of the city, in open areas in the field, in various parts of an industrial reinforced-concrete building with a high level of electromagnetic interference, and in a special shielded room. Despite the fact that a magnetic field with fixed parameters was used in all the experiments, results of these experiments were different.

2. Experimental

Seeds of wheat of the Odesskaya 51 cultivar were taken for the experiment. Seed germination was conducted in Petri dishes on moist filter paper. The seeds taken as a reference sample were not subjected to any treatment. Ordinary tap water was used for moistening. In the experiments, dry seeds placed in Petri dishes were treated for 1 h; after that, the seeds were moistened and left to germinate.

Experiment 1: treatment and germination in limestone house no. 1 in an environmentally safe region of the city.

Experiment 2: treatment and germination in a room in an industrial reinforced-concrete building on the side facing the television tower located at a distance of 300 m from the building.

Experiment 3: treatment in a room in an industrial reinforced-concrete building on the side facing the television tower; germination in a grounded metal cabinet.

Experiment 4: treatment in a room in an industrial reinforced-concrete building on the side opposite of the television tower; germination in a grounded metal cabinet.

Experiment 5: treatment and germination in limestone house no. 2 in an environmentally safe region of the city in the zone of action of a constant magnetic field generated by home appliances (column loudspeakers).

Seed germination percentage and sprout length were measured in the experiments.

3. Results

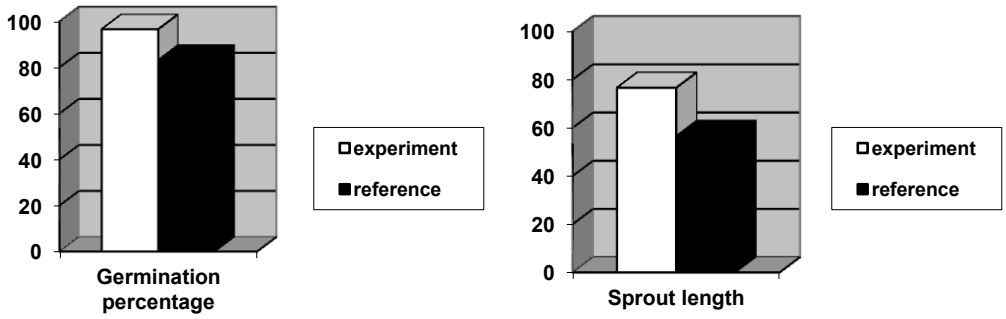

.

Fig. 1. Experiment 1

The "Germination percentage" diagram shows the results of comparative calculation of the percentage of germinated seeds on the 7th day in the experimental and reference samples.
The "Sprout length" diagram shows the results of calculation of the percentage of seeds in which the sprout length is greater than the average sprout length in this experiment.
The results show that, under natural environmentally safe conditions, the seeds in the experimental sample exposed to a positive effect of the magnetic field give better results than the seed of the reference sample.

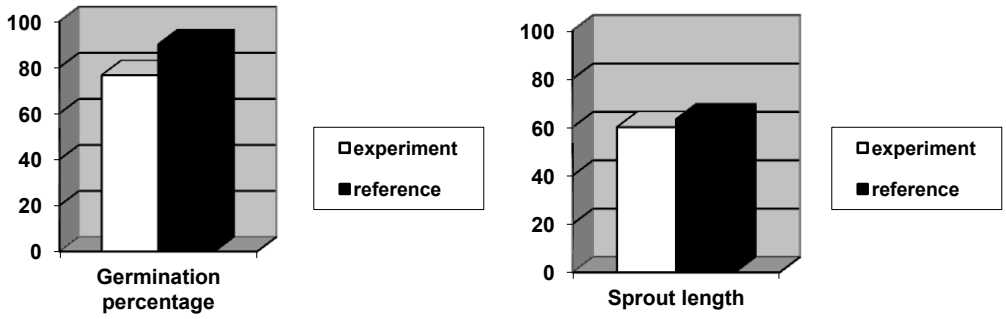

.

Fig. 2. Experiment 2

The "Germination percentage" diagram shows the results of the comparative calculation of the percentage of germinated seeds on the 7th day in the experimental and reference samples.
The "Sprout length" diagram shows the results of calculation of the percentage of seeds in which the sprout length is greater than the average sprout length in this experiment.

The experiment was conducted in the presence of various technogenic fields (electrical power cables, reinforced-concrete building fittings, emissions of television transmitters and retransmitters). The results show that the seeds in the experimental sample were more sensitive to external fields, including harmful technogenic emissions.

The "Germination percentage" diagram shows the results of the comparative calculation of the percentage of germinated seeds on the 7th day in the experimental and reference samples.

The "Sprout length" diagram shows the results of calculation of the percentage of seeds in which the sprout length is greater than the average sprout length in this experiment.

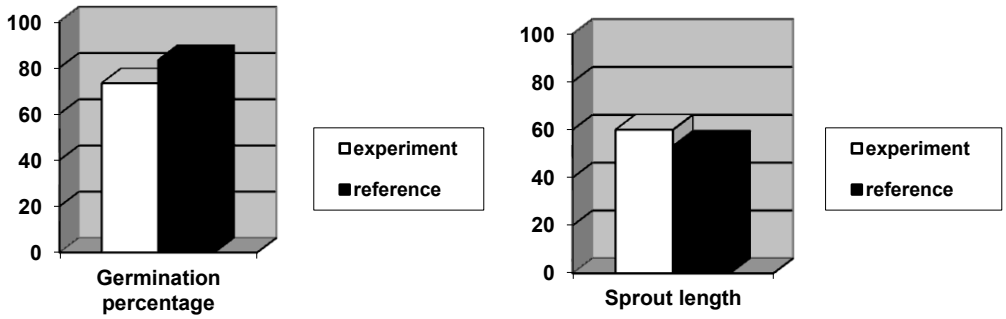

.

Fig. 3. Experiment 3

In the experiment, the magnetic field treatment was conducted with the above parameters in the presence of technogenic fields (similar to Experiment 2), while germination was conducted in a grounded steel cabinet to exclude the impact of any external fields.
The results on the germination percentage were better in the reference sample. The data on the sprout length in the experimental sample were better than in the reference sample.

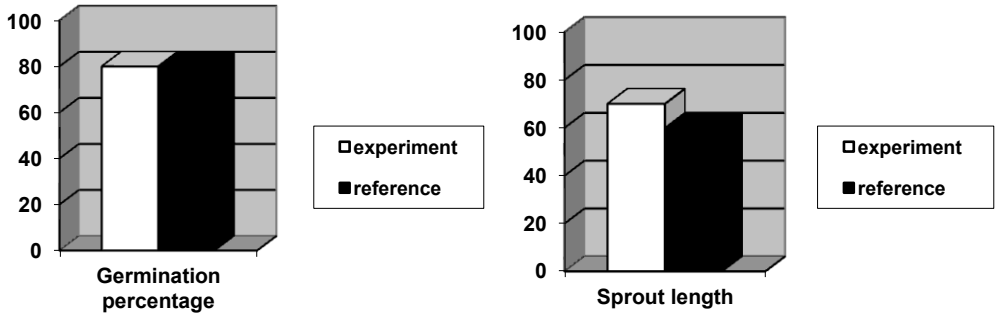

Fig. 4. Experiment 4

The "Germination percentage" diagram shows the results of the comparative calculation of the percentage of germinated seeds on the 7th day in the experimental and reference samples.

The "Sprout length" diagram shows the results of calculation of the percentage of seeds in which the sprout length is greater than the average sprout length in this experiment.
In this experiment, treatment was conducted under conditions of a significant weakening of the effect of the television tower, while maintaining all other technogenic fields. Germination was conducted in a grounded steel cabinet similar to Experiment 3.

The results show that there is no difference in the germination percentage of the experimental and reference samples, while the number of sprouts with a length greater than the average sprout length in the experiment is larger in the experimental sample.

The "Germination percentage" diagram shows the results of the comparative calculation of the percentage of germinated seeds on the 7th day in the experimental and reference samples.

The "Sprout length" diagram shows the results of calculation of the percentage of seeds in which the sprout length is greater than the average sprout length in this experiment.

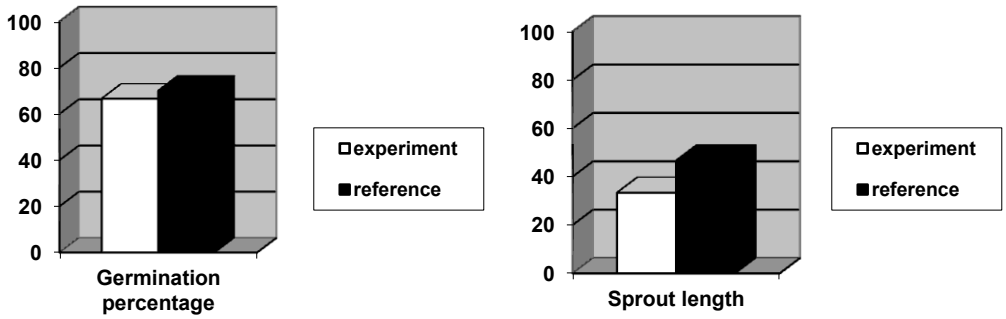

.

Fig. 5. Experiment 5

In this experiment, the effect of a constant magnetic field induced by the magnets of a home audio system was studied. Treatment and germination were conducted in close vicinity (0.7 m) to the magnetic field source. The germination percentage of the experimental sample was lower than that in the reference sample. With respect to the number of seeds with the sprout length greater than the average sprout length in this experiment, the results of the experimental sample were also worse than in the reference sample.

4. Discussion

To optimize the technique of exposing dry seeds to a low-frequency low-intensity magnetic field, experiments were conducted under different environmental conditions associated with the presence of natural and technogenic electromagnetic fields. In the development of the technique, it was found that the magnetic field treatment of seeds leads to an increase in the sensitivity of the seed cells to external fields, including technogenic fields.

Seed treatment with a low-frequency magnetic field under natural conditions (in the absence of technogenic fields) and germination under the same conditions (Experiment 1) give a positive effect in the development of spouts compared to the reference sample because the cells of the germinating seed receive an additional stimulation pulse.

Subsequent experiments have shown the response of embryos to an adverse impact of technogenic fields. This fact is illustrated by Experiments 2–5, which were conducted in the presence of various technogenic fields. The development of seeds in the experimental samples was worse than that in the reference sample. Thus, seed treatment and germination under the same conditions with exposure to technogenic fields (Experiment 2) shows a delay in development in the experimental sample with respect to both seed germination and sprout length in comparison with the reference sample. In the case of treatment in the zone of action of technogenic fields and germination under neutral conditions in a grounded metal cabinet (Experiment 3), the results show that, in the absence of technogenic fields, the experimental sample is superior to the reference sample in the sprout length and inferior in the germination percentage. In Experiment 4, treatment was conducted at a distance from the television tower; this condition led to the same results on the germination percentage in the experimental and reference samples; germination under neutral conditions of a metal cabinet also showed the advantage of the experimental sample. The experiment (seed treatment and germination) conducted under the action of a constant magnetic field generated by a home audio system yielded results identical to those of Experiment 2, where the seeds were subjected to technogenic

fields of industrial origin.

These facts suggest that, at the initial stage of development of an organism, in the period of active cell division, the role of the energy component of the environment becomes more significant. Therefore, the absence of any field of artificial technogenic origin is of particular importance in this period.

Taking into account the general laws governing the development of organisms at the cellular level, we can assume that technogenic fields play a particular role for a human body at the moment of impregnation and initial development of the body when the cells of the embryo most actively respond to the surrounding fields.

5. Conclusions

(1) The exposure of dry seeds to a low-frequency low-intensity magnetic field of natural origin has a positive effect on the development of plants.
(2) Technogenic fields of industrial and domestic origin negatively affect the growth and development of organisms.
(3) It is necessary to take into account the negative impact of artificial technogenic fields on the human body, especially during pregnancy.

References

[1] V. P. Kaznacheev and L. P. Mikhailova, Bioinformatsionnaya funktsiya estestvennykh elektromagnitnykh polei, Nauka, Novosibirsk, 1985.
[2] N. A. Temur'yants, B. M. Vladimirskii, and O. G. Tishkin, Sverkhnizkochastotnye elektromagnitnye signaly v biologicheskom mire, Naukova Dumka, Kiev, 1992.
[3] A. M. Berkutov, V. I. Zhuleva, G. A. Kuraeva, and E. M. Proshina, Sistemy kompleksnoi elektromagnitoterapii, Laboratoriya Bazovykh Znanii BINOM, Moscow, 2000.
[4] N. G. Bochkarev, Magnitnye polya v kosmose, Nauka, Moscow, 1985.
[5] Ju. A. Kholodov, Reaktsiya nervnoi sistemy na elektromagnitnye polya, Nauka, Moscow, 1975.
[6] A. S. Presman, Eelektromagnitnye polya i zhivaya priroda, Nauka, Moscow, 1968.
[7] A. P. Dubrov, Geomagnitnoe pole i zhizn', Ed. by Yu.A. Kholodov, Gidrometeoizdat, Leningrad, 1974.
[8] Eelektromagnitnye polya v biosfere, Ed. by N. V. Krasnogorskaya, Nauka, Moscow, 1984.
[9] A. O. Koshkina, Sovrem. Tekh. Tekhnol., 6 (2012). URL: http://technology.snauka.ru/2012/06/985
[10] Sidorenko Anatolie, Sibaev Alexandr, Groisman Irina, Procedeu de tratare a semintelor inainte de semanat , Brevet de inventie de scurta durata MD 641, 2012.10.26.

THEORETICAL AND EXPERIMENTAL STUDY OF MECHANISMS GOVERNING THE OCCURRENCE OF ELECTRIC DISCHARGES IN GASES

P. Topala[1], V. Kantser[2], and A. Hirbu[1]

[1]Alecu Russo Balti State University, 38 Pushkin Str., Balti, MD - 3100, Republic of Moldova
[2] Institute of the Electronic Engineering and Nanotechnologies, Academy of Sciences of Moldova, Academiei, 3/3. MD - 2028. Chisinau, Republic of Moldova
E-mail: arefahirbu@yahoo.com

(Received September 17, 2015)

Abstract

Some mechanisms governing the occurrence of electric discharges in air at atmospheric pressure have been analyzed theoretically and demonstrated experimentally. It has been shown that several electron avalanches can be simultaneously and randomly initiated on the active surface of the cathode; at the same time, the plasma ions can cause additional avalanches both on the cathode surface and in the gap.
Keywords: plasma, electron, ion, avalanche, homogeneity

1.Introduction

Electric discharges in gases have found wide application in various fields of physics [1–5] and engineering [6–10]; however, some problems of ignition, plasma formation, plasma homogeneity or heterogeneity, energy transformation and energy balance, etc. remain open. The concept of electric discharge in gases is applied in all cases where an electric current flows through a gaseous medium. To provide the electric current circulation through a gaseous medium, it should be subjected to ionization using any effective method. Electric discharges in gases can be produced for a wide range of pressures, while the current can be varied in very wide limits (from 10^{-8} to 10^{6} A and even higher). Electric discharges in gases can be of two types: stationary and nonstationary; both exist for a very short time.

An important role in electric discharges in gases is played by the parameters of the circuit of loading and unloading of the current pulse generator, because even the gap formed by the electrodes in which the plasma arises is part of this electric circuit.

At present, electric discharges are divided into three distinct types as follows [5]:

(i) Townsend discharge, or dark discharge (discharge current $I < 10^{-8}$ A);
(ii) glow discharge ($I \sim 10^{-6}$–10^{-1} A);
(iii) arc discharge ($I > 10^{-1}$ A).

The dark discharge current is very low; therefore, it is difficult to register it. A dark discharge is nonstationary; that is, a current does not cause ionization capable of maintaining the discharge; therefore, it is necessary to affect the medium of the gap with an external ionizing agent, such as UV radiation, X-rays, laser radiation, or other types of actions capable of ionizing the working medium.

With an increase in the potential difference applied to the gap and at low pressures of the active gaseous medium, a dark discharge is transformed into a glow discharge at which the

diffuse illumination of a color that is characteristic of the used gas (or gas mixture) is observed, while an electric current up to a few milliamperes circulates in the working medium.
The gas pressure on the order of atmospheric pressure and a low external circuit resistance provide conditions for the transition to an arc discharge. The current is a function of parameters of the external discharge circuit.

The initial structure of the plasma formed in the gap in the case of electric discharges is determined by the breakdown voltage.

The breakdown voltage is considered to be a potential difference applied to the gap in a gaseous medium, an increase in which provides a self-discharge in the gas. This quantity is a function of properties of the electrode material, the medium in which the discharge occurs, and the size of the gap.

2. Theoretical Analysis of the Conditions for Electric Discharge Ignition in Gases

Let two electrodes be arranged in a given volume of a gas to form a gap with size *L* and a constant-value potential difference *U* be applied to the gap. The appearance of free electrons and ions in the gap is caused by the action of an external agent and by the action of an electric field with intensity *E*. In this case, they receive a certain amount of energy exceeding the ionization potential of the neutral particles. Under these conditions of action of external energy sources and application of electric fields to the gap, the following was found [4]:
—In the gas, only one type of singly charged ions can appear, and the ion concentration is so small that the number thereof remains constant in time owing to recombination.
—The rate of occurrence of electron–ion pairs caused by an external ionizer in the entire volume is also a constant quantity.
—The pressure in the gap (*L*) has such a value that both the free path of electrons and the transmission of the kinetic momentum and energy are much smaller than the gap size $\lambda << L$.
—The drift velocity of electrons and ions is directly proportional to the intensity of the local electric field expressed by the relationships [4]

$$v_e(x) = \mu_e E(x);$$
$$v_i(x) = \mu_i E(x) \quad (1)$$

where μ_e and μ_i represent the mobility of electrons and ions.

The mobility of electrons and ions can be expressed in terms of collision frequency through the following relationships [4]:

$$\mu_e = \frac{e}{m_e \nu_{e0}};$$
$$\mu_i = \frac{e}{m_i \nu_{i0}} \quad (2)$$

The distribution function of electrons with respect to energy is determined by the intensity of the local electric field. For a small degree of ionization of the plasma, the electron distribution function in any gas is determined by the ratio of the intensity of the local electric field (*E(x)*) and the neutral particle concentration (*N*) through the relationship: $\frac{E(x)}{N}$. Depending on the $\frac{E(x)}{N}$ parameter and ionization frequency, the rate of increase in electrons and ions owing to collisional ionization is determined through the relationships [4]

$$\frac{\partial n_e}{\partial t} = S + \nu_i n_e - \frac{\partial}{\partial x}\left[\mu_e n_e E(x)\right] \tag{3}$$

$$\frac{\partial n_i}{\partial t} = S + \nu_i n_e + \frac{\partial}{\partial x}\left[\mu_i n_i E(x)\right] \tag{4}$$

where ν_i is the ionization frequency that, in the case of collision with a molecule or an atom in the working medium, gives rise to an electron at a point in space per second.

Conditions for electric discharge ignition in gaseous environments depend on both the potential difference applied to the gap and the free path of electrons and ions. In the case of motion of electrons in gaseous environments, they collide with molecules or atoms of the gas and cause the formation of free electrons. This process is characterized by the first Townsend coefficient [3]:

$$\alpha = \frac{\nu_i}{\nu_e} \tag{5}$$

It characterizes the number of electrons that form a free electron in the working medium at a distance of 1 cm in the path while moving in the opposite direction to the electric field with intensity *E*.

If we take into account that the electrons are initially emitted from the cathode and move to the anode, then the following boundary conditions can be established for this situation [3]:

at the cathode ($x = 0$): $\gamma_i j_i(0) = j_e(0)$; $\quad j_e = en_e\nu_e$

at the anode ($x = L$): $j_i(L) = 0$. $\qquad j_i = en_i\nu_i$ (6)

Plasma ions in collision with the cathode can cause secondary electron emission. To take this fact into account, the second Townsend coefficient γ_i is used; its values lie in a range of $\gamma_i = 10^{-4} - 10^{-1}$.

The electron and ion current density varies depending on the area of the gap with respect to the origin of coordinates and can be expressed by the relationships [3]

$$\begin{cases} \dfrac{\partial j_e}{\partial x} = eL + \alpha j_e; \\ -\dfrac{\partial j_i}{\partial x} = eL + \alpha j_i, \end{cases} \tag{7}$$

The total density of electron and ion currents in the gap is constant and described by the equation [3]

$$j = j_e + j_i = const\ . \tag{8}$$

Taking into account the intensity of the electric field applied to the gap and the variation in the size thereof in accordance with the Townsend breakdown criterion, we can determine the breakdown voltage in the gap for a gaseous medium through the relationship [3]

$$Ubr = \int_0^L E(x)\,dx \tag{9}$$

Considering equation (9), we can write the following equation [3]:

$$\gamma_i \exp \int_0^L \alpha\left[E(x)\right]dx = 1 + \gamma_i \tag{10}$$

The condition given by equation (10) can be achieved only if the gap size (L) is smaller than the Debye radius [3]:

$$L < \left(W / 4\pi n_e e^2\right)^{-1/2} \equiv r_D \tag{11}$$

Based on relations (10) and (11), in accordance with [4], we can write

$$\gamma_i \exp\left[\alpha (U_{str} / L)\right] L = 1 + \gamma_i \ . \tag{12}$$

Executing the required transformations, we obtain the following expression for the first Townsend coefficient [3]:

$$\alpha = \frac{2N}{v_e} \int_{\varphi}^{\infty} f(W)\sigma_i(W)\left(\frac{W}{m}\right)^{1/2} dW \ , \tag{13}$$

where *f(W)* is the energy distribution function, $\sigma_i(W)$ is the ionization section of the gas molecules, φ is the ionization potential of the gas molecules, and N is the total number of particles in the gap. The *f(W)* and ν_e quantities are determined by the $\frac{E}{N}$ ratio.

Taking into account relations (10), (12), and (13) and executing the required transformations according to [3], we obtain

$$\frac{\alpha}{N} = \psi\left(\frac{E}{N}\right) \ . \tag{14}$$

The last equation is in a good agreement with the Paschen similarity rule, according to which the breakdown voltage is determined by the product of the gas pressure (which expresses the density of neutral particles N) by the discharge gap length $P \cdot L$.

Dependence $\psi\left(\frac{E}{N}\right)$ as a function of $U_{br}(NL)$ takes the form [3]

$$\psi\left(\frac{E}{N}\right) = A \exp\left(-\frac{BN}{E}\right) . \tag{15}$$

Here, A and B are empiric constants.

3. Experimental Analysis

The mechanisms governing the occurrence of electric discharges in gases were determined as in the case of classical schemes with the release of the energy stored in a bank of capacitors into the gap with a gaseous medium formed by two electrodes. The experimental installation, the circuit of which is shown in [11–13], consists of the following elements: a DC power source at a voltage of U = 25 kV, a circuit-breaker CB, a bank of capacitors (C), a ballast resistor R, a tool electrode, and a workpiece. With the use of a tool electrode (specifically designed), division of the discharge current occurs in a few channels. This feature facilitates the development of pulse discharges leading to high current densities and thereby to an improvement of the efficiency of consumption of the discharge energy. The interelectrode gap is S = 5 mm. The tool electrode composed of a large number of channels (about 800 channels/cm^2) electrically separated from each other limits the current in each channel and provides the homogeneity of the resulting plasma.

Measurement of current pulse parameters (length, shape, and amplitude value) [11] and visualization thereof are conducted using an Osc (C8-13) memory oscilloscope and a coaxial

shunt with an active resistance of R_s = 0.003 Ω [8] included in the negative branch of the discharge circuit. Figure 1 shows the shape of the resulting discharge pulses. The total current measured in this circuit will be equal to the algebraic sum of the elementary currents flowing parallel in each of these channels. The shape of the pulse is a direct function of the capacity and resistance (active, capacitive, and inductive) of the discharge circuit of the current pulse generator. The shape of pulse discharge oscillations obtained in the studies is determined by the capacitive and inductive components of the discharge circuit [11–13]; they can be modified through the construction of the electrodes and the deviation from straightness of the wires that form the discharge circuit.

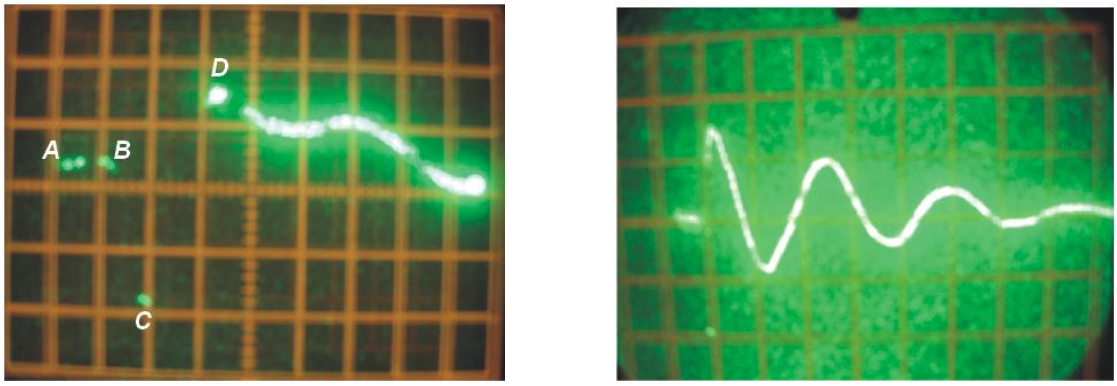

(a) (b)

Fig. 1. Shape of the electric discharge pulse [11]: the scale interval along the vertical axis of 200 V/div; the scale interval along the time axis: (a) 0.1 and (b) 10 μs/div.

Under laboratory conditions, plasma was obtained using a voltage multiplier circuit (voltage pulse generator) to a potential difference of about 80 kV. Plasma was formed in an air environment at atmospheric pressure and a vacuum chamber pressure of 50 torr. Figures 1a and 1b show oscillograms of electric discharges for different scan times. The *AB* curve in Fig. 1 corresponds to autoionization (in this case, a special electrode acts as an electron gun); the *BC* curve corresponds to the basic discharge (plasma formation); and the *CD* curve corresponds to the relaxation process followed by the recharging of the bank of capacitors of the generator.

Only about 7–10% of the energy stored by the bank of capacitors of the generator is consumed for preventive ionization, while the other portion is released in the active medium which is already maximally ionized.

4. Results and Discussion

Examination of electric breakdowns in gases under the action of pulse voltage is a separate problem of physics of electric discharges in gases. It is these studies where the breakdown mechanisms were determined: Townsend and streamer.

To provide a self-discharge on electrodes placed in a gaseous environment, it is necessary to apply a potential difference, which in turn is a function of pressure and type of the gas, electrode configuration, the distance between the electrodes, the type of preventive ionization applied to the active medium, etc. A critical potential difference is considered to be a static

breakdown applied to the gap (U_{br}). As the voltage applied to the gap achieves a value of breakdown voltage ($U = U_{br}$), the current that flows through the active medium abruptly increases (see the *BC* portion in Fig. 1) and visible illumination of the working medium between the electrodes is apparent owing to the fact that the resistance of the medium becomes comparable with the resistance of the external discharge circuit.

A completely different situation is observed if a pulse voltage is applied to the gap (see Fig. 1b). In this case, voltage pulses applied to the gap are much shorter than the time of development of a breakdown. In this case, the discharge occurs at voltages exceeding the static breakdown voltage. Overvoltage is characterized by coefficient K_p which represents the ratio between voltage pulse amplitude U_a and static breakdown voltage U_{br}:

$$K_p = \frac{U_a}{U_{br}} \tag{16}$$

It was experimentally found that, with an increase in coefficient K_p, the time of ignition of the discharges decreases; accordingly, in this case, pulses applied to the gap should have a voltage front with the duration on the order of a nanosecond.

At the breakdown of the gap in a gaseous medium, the active resistance decreases almost from ∞ to very low values. In [8, 9], for conditions of pulse electric discharges, it was shown that the gap resistance in the air at normal pressure decreases to 0.1 Ω; therefore, at the initial time of application of voltage U_a to the gap, the current through the active medium increases and the voltage between the electrodes decreases resulting in the ignition of a pulse electric discharge, which is a glow discharge. The transition from a glow discharge to an arc discharge is characterized by an abrupt decrease in the gap resistance and the transition from an aperiodic to oscillatory current discharge.

At a pulsed breakdown of gases, between the time of application of the voltage to the gap and the beginning of a breakdown, which is evident from an abrupt decrease in voltage, there is a time interval referred to as the delay time. The delay time is measured from the moment when the voltage achieves a breakdown value to the moment of voltage decrease to a value of 0.9 U_a. The beginning of a breakdown in gases is equivalent to a sudden decrease in voltage, while the level of the current that determines the decrease in voltage depends on the external electric circuit resistance.

The decrease in the gap voltage occurs at different stages of increase in the gap conductivity as a function of both the electric circuit resistance and different physical and chemical processes that cause an increase in the charged particle concentration. Until the beginning of ionization in the working medium between the electrodes, there must be at least one free electron; therefore, the ignition delay time for electric discharges should be decomposed into two components [3]:

(a) static delay time t_s, during which an electron capable of ionizing the gaseous medium appears in the interelectrode gap and

(b) the time of formation of a conductivity channel t_f during which a breakdown occurs owing to the development of an electronic avalanche and the intensification of ionization.

Depending on the established initial conditions, the correlation between t_s and t_f can be different. During the ionization of the active medium with an external agent, $t_s = 0$; after that, the delay time of the discharge will be determined only by the time of formation t_f. Experimental tests conducted under these conditions provide the possibility of deriving information on the ionization mechanism in the case of delay of the breakdown.

The pattern of development of a breakdown in the gap in a gaseous medium for arc electric discharges is determined by the initial number of electrons present in it at the moment of application of a potential difference. This feature is responsible for the condition of a spatial homogeneity of plasma in a direction perpendicular to the lines of force of the electric field and caused by the electronic avalanche field.

This condition can be shown through the expression for the diffusion radius of the avalanche for time τ [3]:

$$R = (4 D \tau)^{1/2} \tag{17}$$

where D is the diffusion coefficient of the electrons. This coefficient is a function of the average energy; the electron mobility can be expressed in terms of the Einstein relationship [3]:

$$D = \frac{2W\mu_e}{3e} \tag{18}$$

where W is the average energy of the electrons; $\mu_e = \dfrac{e}{m_e \nu_e}$ is the electron mobility, m_e is the electron mass; ν_e is the electron collision frequency; and e is the electron charge.

Critical radius R_{cr} of the electronic avalanche at time τ_{cr} (time within which the intrinsic electric field becomes equal to the applied electric field) can be determined by the relationship [3]

$$R_{cr} = \left(\frac{eN_e}{E} \right)^{1/2} \tag{19}$$

where N_e is the number of electrons in the avalanche and E is the intensity of the external electric field (applied).

The number of electrons in the avalanche at time τ_{cr} is determined by the ionization in the direction of electron drift from the relationship [3]:

$$N_e = \exp(\alpha \nu_e \tau_{cr}) \tag{20}$$

where α is the collisional ionization coefficient, or the first Townsend coefficient and ν_e is the electron drift velocity. The latter is equal to the product of the electron mobility by the intensity of the electric field applied to the gap [3]:

$$\nu_e = \mu_e E \tag{21}$$

Executing the necessary transformations, from relationships (19)–(21), we obtain the following expression for the critical radius of the electronic avalanche [3]:

$$R_{cr} = \left[\frac{8}{3} \frac{W}{\alpha e E} \ln N_e \right]^{1/2} \tag{22}$$

Using equation (22), we can write the condition for the minimum spatially homogeneous electron concentration required for the breakdown in the gaseous medium in the gap [3]:

$$n_e > (2 R_{cr})^{-3} = \left(\frac{3}{32} \frac{\alpha e E}{W} \right)^{3/2} \left(\ln \frac{E R_{cr}^2}{e} \right)^{-3/2} \tag{23}$$

Depending on the type and pressure of the gas, the calculations conducted using relationship (23) show that the initial electron concentration required for the breakdown of the gap is as follows: $n_e > (10^4–10^6)$ cm^{-3}.

Another condition for spatial homogeneity of the plasma at the time of breakdown of the gap is the rapid emergence of electrons in regions that they have left and the movement of these

electrons towards the anode. If this condition is not fulfilled for the time interval of $\frac{L}{v_e}$, then the electron concentration in the volume of the gas in the gap will be at a level of background and a breakdown will not occur outside the dielectric medium between the electrodes.

An important contribution will come to the reproduction of electrons in the space between the electrodes from the secondary ionization caused by the electron emission as a result of ion bombardment of the cathode and the photoionization of the gas under the action of the intrinsic emission of plasma.

To meet the condition of complete compensation of the number of electrons moving to the anode, it is necessary to fulfill the following condition [3]:

$$\gamma_i \exp\left(\int_0^L \alpha\, dx\right) > 1, \tag{24}$$

where L is the distance between the electrodes and γ_i is the second Townsend coefficient that takes into account secondary electron emission.

During the development of a breakdown of the working medium (i.e., in the case where the electric field in the interelectrode gap is strongly distorted), with allowance for relationship (24) and the data of [3], the following dependence can be found:

$$\gamma_i \exp\left(\int_0^L \alpha\, dx\right) > \gamma_i \exp(\alpha L). \tag{25}$$

Analysis of the above reveals the following inequality:

$$\gamma_i \exp(\alpha L) > \exp(\alpha v_e \tau_{cr}) = N_e. \tag{26}$$

Taking into account relationships (19) and (23), we can deduce that

$$\gamma_i \exp(\alpha L) > \gamma_i \frac{E}{en_e^{2/3}}. \tag{27}$$

The right-hand side of inequality (27) can be determined taking into account the fact that the initial electron concentration is $n_e = 10^6$ cm^{-3}, the second Townsend ionization coefficient has a value of $\gamma_i \approx 10^{-4}$, and the typical value of the electric field intensity at the time of development of the discharge is $E = 10^2 \frac{V}{cm}$; then, according to [3], we obtain

$$\gamma_i \frac{E}{en_e^{2/3}} = 10^{13} \tag{28}$$

Thus, we can state that the main advantage of a multichannel electrode is that it, on the one hand, excludes an auxiliary preventive ionization installation and, on the other hand, determines a substantial increase in the first Townsend coefficient and an increase in the critical number of electrons in the avalanche in the case of electric discharges in an air environment at atmospheric pressure.

The time of formation of breakdown pulses is a function of the intensity of ionization of the gas in the gap at the time of development of an electronic avalanche and at later stages. This fact depends on the increase in the charged particle concentration in the gap. To correctly describe this process, collisional ionization coefficient is applied. In accordance with [3], an increase in the number of charge carriers in a single electron avalanche over time obeys the law

$$N = \exp(\alpha v_e t), \tag{29}$$

where v_e is the electron drift velocity.

In a homogeneous electric field, the emission current at the cathode can be determined by the relationship

$$i = i_{em} \frac{\exp(\alpha d)}{1 - \gamma[\exp(\alpha d) - 1]} \Rightarrow \ln \frac{i}{i_{em}} = \alpha d . \tag{30}$$

Based on the fact that the collisional ionization coefficient is a function of electric field intensity and gas pressure, in accordance with the similarity law, we can write

$$\frac{\alpha}{p} = f\left(\frac{E}{p}\right);$$

$$\frac{\alpha}{p} = A \exp\left(-\frac{B}{E/p}\right). \tag{31}$$

For the air: E/p = (36–180) $\frac{V}{cm \cdot Torr}$, A = 8.6 (cm · Torr)$^{-1}$, B = 254 $\frac{V}{cm \cdot Torr}$; applying equation (31) we obtain α = 38. The calculations conducted for a nitrogen working medium under the same conditions have revealed that α = 32.

The Townsend mechanism of breakdown of an active gaseous medium assumes that the volume load of the electronic avalanche does not distort the electric field in the gap. In this case, the number of electrons in the avalanche will be lower than a critical value (N_{cr}) [3]:

$$\exp(\alpha L) < N_{cr} \tag{32}$$

Substituting values of α and L in (32) we obtain [3]

$$N_{cr} > e^{\alpha L} = e^{38 \cdot 0.5} = e^{19} \approx 1.8 \cdot 10^8$$

In this situation, it is clear that, under the studied conditions, the condition for self-discharges is also satisfied [3]:

$$\mu = \gamma_i [\exp(\alpha L) - 1] \geq 1 \tag{33}$$

The meaning of this coefficient is that the formation of a solitary avalanche as a result of secondary processes (characterized by coefficient γ_i) at the cathode gives rise to a secondary electron that acts as an initiator of a new electronic avalanche.

If these conditions are satisfied, the initial phase of the breakdown is determined by a large number of consecutive electronic avalanches and the parameter μ determines how many times greater is the number of electrons in each presiding avalanche than in the previous avalanche.

Since the avalanches were formed randomly on different portions of the active surface of the cathode (this fact is visually confirmed by electrode spots on the cathode surface [12]), this mechanism, in most cases, leads to a volumetric flow (transition) of current at the delay of the breakdown and initial moments after an abrupt decrease in voltage.

Thus, the following criteria can be established for the transition of pulse electric discharges in arc discharges:

$$\exp(\alpha L) \geq N_{cr}$$

$$\ln(N_{cr}) = 18 \div 20 . \tag{34}$$

In the case of the circuit applied in experimental research [11–13], the critical value of the number of electrons for the transition from glow discharges to arc discharges (breakdown) is $\ln(N_{cr}) \approx 30 \div 50$, which improves conditions for the development of glow discharges.

5. Conclusions

Taking into account the theoretical and experimental findings from the literature and our own results, we can make the following conclusions.

—The main role in pulse electric discharges is played by the first Townsend coefficient.

—The necessary and sufficient condition for the ignition of glow electric discharges is the critical number of electrons of $N_{cr} \leq 1.8 \cdot 10^8$.

—The circuit applied in the experimental research does not require preventive ionization of the studied environment (air) because of the increased excitation capacity owing to the special construction of the electrodes, which makes it possible to exceed the critical number of electrons described in the literature.

—The basic discharge with the formation of plasma in the used circuit occurs after the autoionization of the continuous active medium in a pulsed discharge cycle.

References

[1] V. L. Granovskii, Elektricheskii tok v gazakh. Ustanovivshiisya tok v gazakh, Nauka, Moscow, 1971, 292 p.

[2] Yu. P. Raizer, Fizika gazovogo razryada, Nauka, Moscow, 1987, 593 p.

[3] Yu. D. Korolev and G. A. mesyats, Fizika impul'snogo proboya gazov, Nauka, Moscow, 1991, 224 p.

[4] E. P. Velikhov, A. S. Kovalev, and A. T. Rakhimov, Fizicheskie yavleniya v gazorazryadnoi plazme, Nauka, Moscow, 1987, 154 p.

[5] A. M. Khovatson, Vvedenie v teoriyu gazovogo razryada, Atomizdat, Moscow, 1980, 182 p.

[6] L. Slatineanu, Tehnologii neconventionale in constructia de masini, Tehnica Info, Chisinau, 2000, 252 p.

[7] B. A. Artamonov, Iu. S. Volkov, V. I. Drojalova, et al., Elektrofizicheskie i elektrokhimicheskie metody obrabotki materialov, vol. 1, Vysshaya Shkola, Moscow, 1983, 242 p.

[8] P. Topala and P. Stoicev, Tehnologii de prelucrare a materialelor conductibile cu aplicarea descaarcarilor electrice in impuls, Tehnica Info, Chisinau, 2008, p.265.

[9] I. Grigoriev, S. O. Şireeva, D. F. Belonojko, and A. V. Klimov, Elektron. Obrab. Mater. 4, 34, (2004).

[10] C. Diaconescu, Cercetari privind structura generatoarelor de impulsuri cu adaptare flexibila, in timpul real, la conditiile procesului de prelucrare prin eroziune electrica, Extended Abstract of Doctoral Dissertation, Lucian Blaga University, Sibiu, 2008, 37 p.

[11] A. Hirbu, P. Topala, and A. Ojegov, Secondary Radiation in Color Optical Filter Glasses by the Action of Plasma, Modern Technologies in Industrial Engineering II, ModTech 2014, Trans Tech Publications, Switzerland, pp. 158–163.

[12] P. Topala, A. Hirbu, and A. Ojegov, Nonconvent. Technol. Rev. 1, 49, (2011).

[13] P. Topala, A. Hirbu, and A. Ojegov, Fiz. Tehnol. Mod. 10 (1–2), 13, (2012).

THE THREE KINDS OF BROWNIAN MOTION

J.-S. Rattinacannou

Member of the European Physical Society
180 rue du Centre Aere, Saint Paul les Dax, 40990 France
E-mail: jsrtncn@free.fr

(Received September 15, 2015)

Abstract

In addition to the Brownian motion of a small particle in the air and the Brownian motion of a resonator, a third and new kind is proposed; it is referred to as the "coherent Brownian motion" and represents the permanent in-phase Brownian motions of an array of nanoresonators. From a theoretical point of view, the possibility of achieving that is addressed, and from a practical point of view, it is shown that the coherent Brownian motion is within current technology reach. An application in energy harvesting devices is considered.

1. Introduction

The description by Robert Brown in his article [1] of 1828, of what will later be called the Brownian motion, drew only little attention of physicists. Some of them supposed that its origin was molecular agitation [2]; however, one had to wait until 1905 and Albert Einstein's article [3] to see that the Brownian motion plays a more important role in Physics [4]. French physicist Jean Perrin conducted experimental tests of the Einstein's theory, which confirmed it and gave evidence of the existence of atoms [5].
Usually, large amplitude of Brownian motion is only observable on microscopic particles. Macroscopic objects do also have a Brownian motion, but so small that it is negligible, although still observable [6]. With the new kind of Brownian motion introduced in this study, large amplitudes of vibration, sustained by thermal agitation, appear in macroscopic bodies and give rise to unexpected properties.

2. The First Kind: the Brownian Motion of a Small Particle in a Fluid Medium

In Fig. 1, the position of a particle subjected to a Brownian motion is taken at a constant time interval, which gives this broken-line trajectory.

Fig. 1. Brownian motion of a particle (Jean Perrin [7]).

Mean-square displacement $\langle x^2 \rangle$ of the particle along the X-direction is [3, 5]

$$\langle x^2 \rangle = 2Dt \tag{1}$$

where x is the displacement of the particle, D is the diffusion constant, and t is the time.

The main feature of this first kind of Brownian motion is that it is a completely disordered motion that never stops.

3. The Second Kind: the Brownian Motion of a Resonator

The Brownian motion of a mechanical resonator [6, 8–19] related to a damped harmonic oscillator is described by the following Langevin equation:

$$m\frac{d^2x}{dt^2} + r\frac{dx}{dt} + kx = f_{th} \tag{2}$$

where x is the resonator displacement, t is the time, m is the resonator mass, r is the resonator mechanical resistance, k is the resonator spring constant, and f_{th} is the fluctuating force due to thermal agitation that drives the resonator. Spectral density $S_{f_{th}}(\omega)$ is constant over all frequencies corresponding to a broad band random process or white noise [19]:

$$S_{f_{th}}(\omega) = 4k_B Tr \tag{3}$$

where ω is the angular frequency, k_B is the Boltzmann's constant, and T is the absolute temperature in Kelvin.

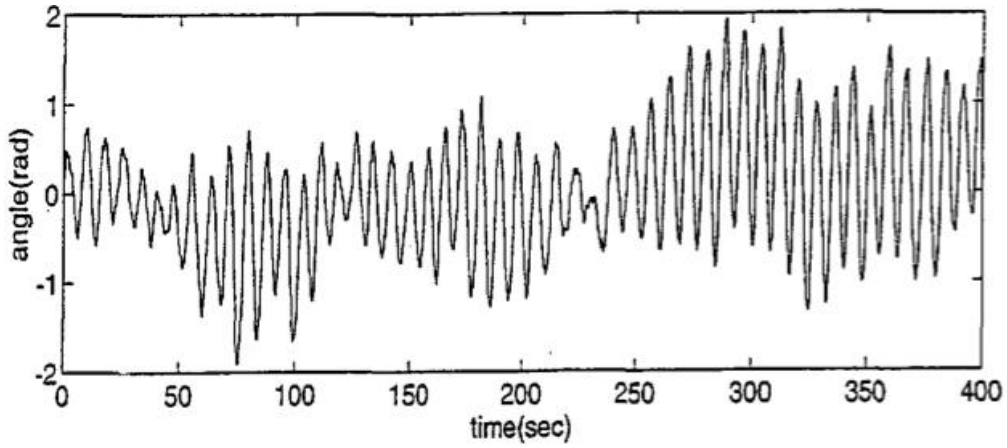

Fig. 2. Brownian motion of a resonator [16] (reproduced with the permission of G. I. González).

Figure 2 shows the Brownian motion of a resonator, which looks like a sine wave of varying amplitude and phase. It is a time record of resonator displacement x. The spectral density of x is peaking at the resonant angular frequency of the resonator ω_0 [12]. So x is a Gaussian narrow band random process [19], and the Brownian motion of a resonator is a vibration of steady frequency ω_0. Then it can be said that a resonator is a fascinating system, which has an outstanding characteristic: its Brownian motion is ordered. This has been well known for a long time [8], but it was not considered outstanding and enough attention has not been paid to it. I point out here this unique property, and I emphasize its prime importance in Physics, which has so far never been acknowledged.

The main feature of this second kind of Brownian motion is its fairly constant vibration frequency, and that it produces order from the disorder of thermal agitation.

4. The Third Kind: Coherent Brownian Motion

4.1. Introduction

Permanent in-phase Brownian motions are possible owing to a resonance, which occurs in mechanical interaction between a macroscopic structure—a plate—and a very large number of microscopic ones—nanopillars [20]. I propose to refer to this unknown kind of Brownian motion as the coherent Brownian motion. This new phenomenon allows energy to be extracted from Brownian motion without preventing such an extraction as stated by the Principle of Microscopic Reversibility [21, 22].

4.2. Description of the device

The device consists of two parts. The first part is a macroscopic object—a plate—which can be square or circular in shape, with a side or a diameter, respectively, of at least 1 mm.

The second part comprises a huge number of microstructures—nanopillars—which form an array on the plate (Fig. 3). An example of a pillar height is 1 μm and the pillar diameter is 100 nm. The aspect ratio (height/diameter) is 1 to 10.

The plate thickness is several times the pillar height.

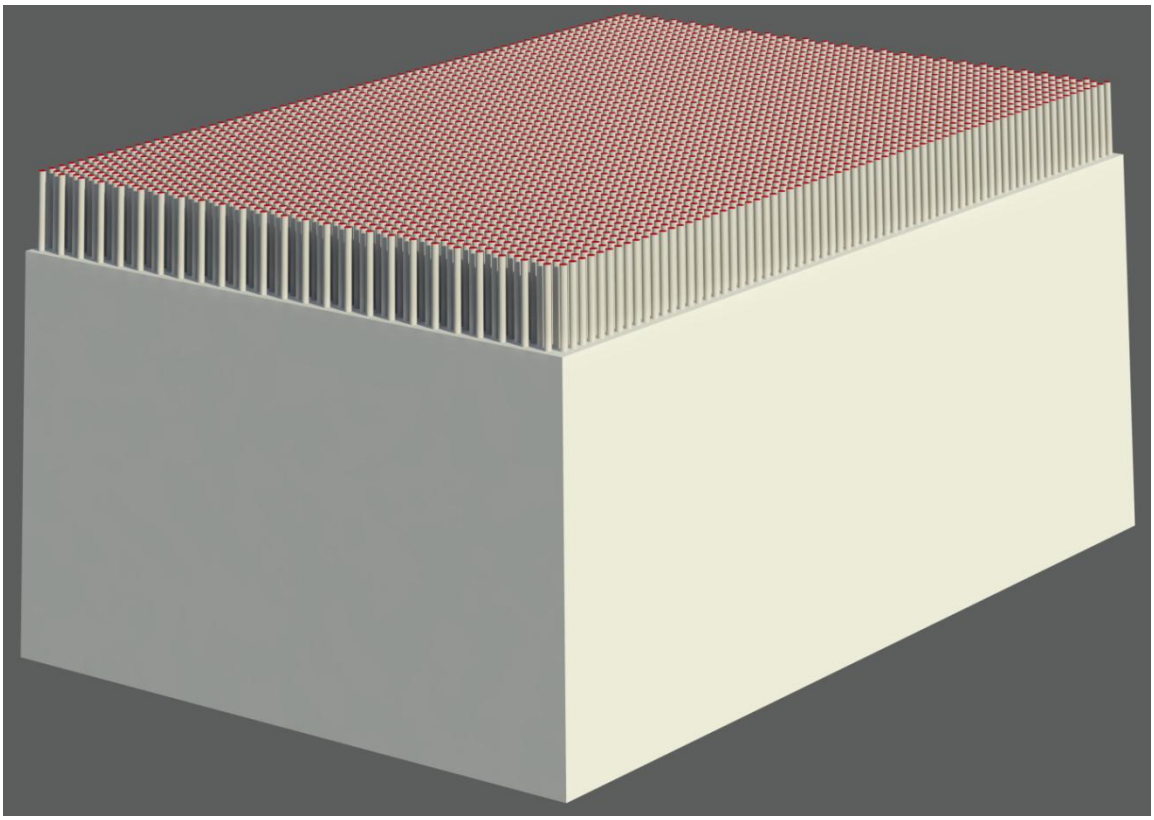

Fig. 3. Small part of the device (50 × 50 pillars), which actually comprises 10^8 to 10^{12} pillars or more.

4.3. The specific problem under study: the random phases of the Brownian motions of nanoresonators

4.3.1 Presentation of the problem: Nanopillars are tiny resonators subjected to Brownian motion; the vibration under consideration is a bulk wave one directed along the axis; it is referred to as the "length mode" (Fig. 4). In this device, the pillars of the array have the same resonant frequency, but random phases, since they vibrate independently of each other. Even if all pillars vibrated in phase at a given time, this process would not last because of the varying phase of the Brownian motion. Then, the question is to maintain one phase throughout the array.

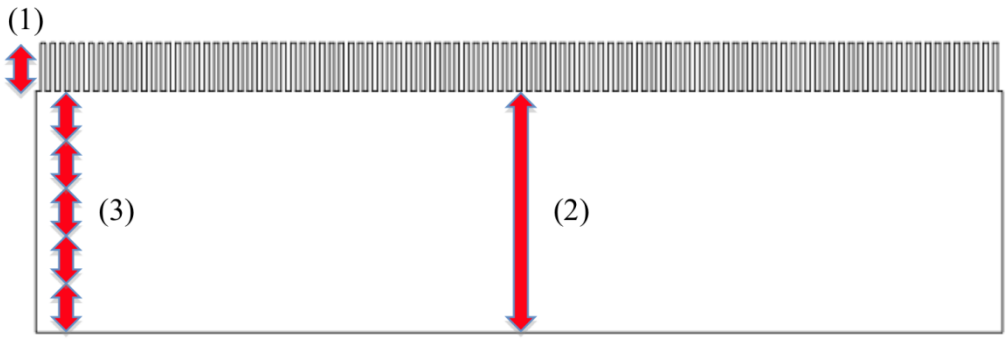

Fig. 4. Cross section of a small part of the device showing: (*1*) the length mode of the pillars, (*2*) the thickness compression mode of the plate, and (*3*) a harmonic of it.

4.3.2 The proposed solution: a mechanical resonance. In order to address this question, the plate is regarded as a macroscopic resonator. Its vibration is a thickness compression mode (Fig. 4), a harmonic of which has the same frequency as the pillar length mode. Then, as soon as the pillars vibrate in phase (ways to achieve this effect are proposed in the next paragraph), they will induce a large resonance of the plate. In turn, the plate, due to its big mass, will impose one single phase to the small pillars. To sum up, the pillars drive the plate, and the plate locks the phase of the pillars.

This makes a standing wave (Fig. 5) appear inside the device, with nodes of vibration and antinodes, including plate and pillars. The pink curve in Fig. 5 is the standing wave. The drawings below the curve show a small part of different device shapes.

The result of this mechanical resonance is a permanent vibration of the plate driven by the in-phase Brownian motions of the pillars.

4.4 Keeping up one phase in an array of nanopillars

In the following, the plate is made of a piezoelectric material with an electrode on each side. I propose two ways to keep up one phase in the vibrations of the pillars.

4.4.1 Application of an external voltage: An easy way to set the pillars in phase is to apply an alternating voltage to the electrodes at the resonant frequency during a short time. I make the supposition, according to paragraph 4.3.2, that the device will then maintain one phase in the vibrations of the pillars.

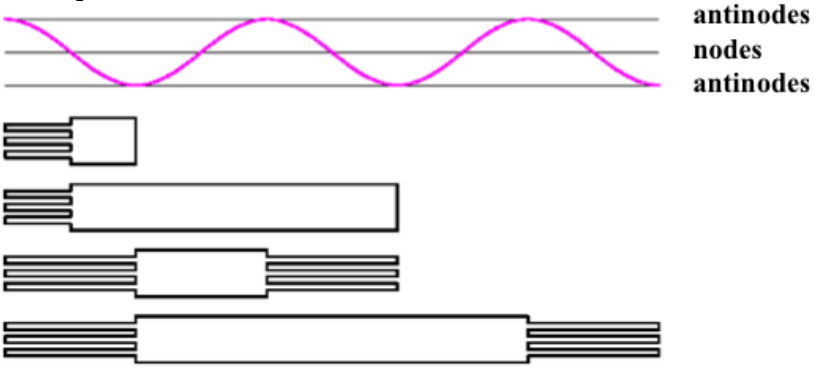

Fig. 5. Standing wave.

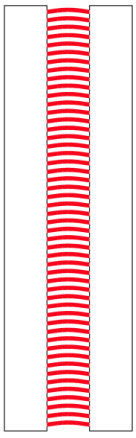

Fig. 6. Double-plate device.

4.4.2 The double-plate device: What is not a supposition but a certainty is the maintaining of the phase provided by a device comprising two plates and an array of nanopillars between those plates (Fig. 6). The latter are set in phase as in the previous case. The resonance of the two plates prevents any phase shift in the vibration of the pillars. The example chosen in Fig. 6 is a flexural vibration; however, it also works for the pillar length mode. The pillars are linked to the plates by their ends. However, they vibrate under thermal agitation. This is essentially because those pillars, on the one hand, have the size to be subjected to a large Brownian motion and, on the other hand, are free to vibrate for the specific mode under study, since their ends are nodes of vibration. Because of this freedom, they can experience Brownian motion.

4.5 Energy harvesting device

The constant vibration of the piezoelectric plate makes a permanent alternating voltage appear at the electrodes. Then, this device can supply an electrical power. At absolute temperature T, the mean energy of the pillar Brownian motion [11] is $k_B T$, the very low value of thermal energy. It is not possible to get a sufficiently large number n of pillars so that it can balance this value. For this reason, the energy of an array of n pillars, which is $nk_B T$, remains low. However, the array power is proportional [23] to both n and ω_0. Then it is product $n\omega_0$ that must balance the above value to get a reasonable amount of power:

$$n\omega_0 \approx (k_B T)^{-1}. \tag{5}$$

This is much easier than in the case with n alone and feasible with the present technology. In this case, the device output power is large enough to be useful.

4.6 Conditions for the resonance to occur

The main conditions for the appearance of resonance in the plate are as follows.
(i) An extremely large number of nanopillars.
(ii) An accurate tuning of the pillar resonant frequencies.
(iii) An accurate ratio of plate thickness to pillar height.
(iv) A not too low ratio of array mass to plate mass.
(v) Very small mechanical losses in the device or, in other words, a device with a very high quality factor.

4.7 A direct connection between the microscopic world and the macroscopic one

Innumerable Brownian motions, coming from the microscopic world, the world of atoms, molecules, micro and nanostructures, are gathered together to produce a mechanical resonance in the macroscopic world, our world. This provides a unique opportunity to observe, at the macroscopic scale, the behavior that usually is the privilege of very low dimensional objects. For instance, the permanent vibration of the plate, which comes from thermal agitation, through the nanopillar array, has an amplitude which is far beyond that of the plate under direct thermal agitation, that is to say, far beyond its own Brownian motion. Then a macroscopic object, the Brownian motion of which is imperceptible, exhibits a vibration due to thermal agitation, which has the same amplitude as the Brownian motion of a nanostructure, a very unusual and strange situation. This makes features that normally belong to microstructures, appear in macrostructures, and this unexpected and amazing property leads to new applications.

4.8 Fabrication

Current technology is able to produce arrays containing a very large number of nanopillars. The best way seems to be: to start with a piezoelectric film (the plate) deposited on a substrate (with electrodes), to deposit a thin film on the surface of this piezoelectric film, and to etch it by RIE or ICP [24–26] in order to get the array. After that, the piezoelectric film is made free-standing by removing the substrate.

5. Discussion and Conclusions

The main feature of this third kind of Brownian motion is a higher degree of order than that of a single resonator, mainly because of the vibration of the plate. The frequency of the pillar Brownian motions is very constant. There is no phase shift in them. There are still variations in the amplitude of the Brownian motion of a pillar, because the thermal energy still acts individually and separately on each pillar, but the plate resonance tends to diminish those changes. The time record of the vibration of any pillar of this array is closer to a sine wave than that in Fig. 2. These peculiar qualities immediately raise two questions:

1. Is coherent Brownian motion still a Brownian motion?
2. Does Physics allow coherent Brownian motion?

5.1 Is coherent Brownian motion still a Brownian motion?

Looking at the disorder in Fig. 1 and at the order in Fig. 2 would not incline us to think that, in both cases, this is Brownian motion, if we knew very little about it. Why then did physicists refer to this vibration of a resonator as Brownian motion? The answer is straightforward: thermal agitation is the cause of it and is also the cause of coherent Brownian motion. We have therefore to admit the possibility of occurrence of an unvarying-phase Brownian motion, the time record of which is close to a perfect sine wave, that is to say, a kind of Brownian motion exhibiting a higher degree of order than the two others.

On the other hand, the plate vibration, which is not a Brownian motion, although thermal energy keeps it going, has a time record which is a pure sine wave.

5.2 Does Physics allow coherent Brownian motion?

The nature of Brownian motion seems to have a varying phase in each pillar of an array. The nature of Brownian motion seems to have random phases in this array. Then I pose the question: how is it possible to assert that coherent Brownian motion will appear in this array, does Physics allow this?

The answer is yes, since there are examples of spontaneous in-phase thermal vibrations of molecules in some liquid crystals [27]. One explains the molecule shape leads to this collective or cooperative motion. If these molecules are taken to be small resonators, this fact strongly supports the existence of coherent Brownian motion.

5.3 Conclusions

We have therefore to acknowledge that the randomness of the usual Brownian motion phase is the result of events and circumstances, rather than a law. It is a contingent fact. For this

reason, because randomness is not a fundamental property of Brownian motion, coherent Brownian motion will occur if the required experimental conditions are met.

The new phenomenon described in this study opens up a new path in the field not only of Brownian motion, but also of all random processes, suggesting that randomness is not a law, nor an essential feature of them, but the lack of any law. Since no law governs randomness, it is possible to introduce some order in random processes, if we know how to do that. I have given two examples of this: more order in the Brownian motion of a resonator, and more order even in thermal agitation by choosing molecules with a special shape without stopping being thermal agitation.

Finally, I would like to point out that coherent Brownian motion needs the device to be built and operate in order to become a reality.

I thank Mr. Jean Lussagnet, architect from Biarritz, France, for the computer-assisted design.
I thank Mrs. Caroline Coombes, English professor, for reviewing the English of this paper.

References

[1] R. Brown, Philosophical Magazine 4, 161, (1828).
[2] See for example: C. Wiener, Ann. Phys. (Leipzig) 118, 79 (1863); Gouÿ L. G., J. Phys. 7, 561, (1888); Rev. Gén. Sci. 1 (1895).
[3] A. Einstein, Annalen der Phys. 17, 549, (1905).
[4] S. G. Brush, The Kind of Motion We Call Heat, North-Holland, Amsterdam, Book 2, 1986.
[5] J. Perrin, Ann. Phys. Chim., 18, 5, (1909).
[6] P. F. Cohadon, A. Heidmann, and M. Pinard, Phys. Rev. Lett. 83, 3174 (1999).
[7] J. Perrin, Les atomes, Félix Alcan, Paris, 1913.
[8] G. E.Uhlenbeck and S. Goudsmit, Phys. Rev. 34, 145, (1929).
[9] M. Morimura, K. Nakagawa, and Y. Nezu, Jap. J. Appl. Phys. Suppl. 2, 135, (1974).
[10] V. B. Braginsky and A. B. Manukin, Measurement of Weak Forces in Physics Experiments, University of Chicago Press, Chicago, 1977.
[11] V. B. Braginsky, V. P. Mitrofanov, and V. I. Panov, Systems with small dissipation, University of Chicago Press, Chicago, 1985.
[12] P. R. Saulson, Phys. Rev. D 42, 2437, (1990).
[13] T. R. Albrecht, P. Grütter, D. Horne, and D. Rugar, J. Appl. Phys. 69, 668 (1991).
[14] T. B. Gabrielson, IEEE Trans. Electron Devices 40, 903, (1993).
[15] G. I. González and P. R. Saulson, Phys. Lett. A 201, 12, (1995).
[16] G. I. González, Brownian Motion of a Torsion Pendulum Damped by Internal Friction, Ph.D. thesis, Syracuse University, NY, 1995.
[17] E. Majorana and Y. Ogawa, Phys. Lett. A 233, 162, (1997).
[18] K. L. Ekinci and M. L. Roukes, Rev. Sci. Instrum. 76, 061101, (2005).
[19] D. E. Newland, An Introduction to Random Vibrations, Spectral & Wavelet Analysis, Third Edition, Dover Publications Inc., Mineola NY, 2005.
[20] J.-S. Rattinacannou, Keeping up One Phase in the Brownian Motions of Nanoresonators By Mechanical Meansm the 7th MSCMP Int. Conf., Chisinau, Republic of Moldova, 16-19 September 2014.
[21] G. E. Crooks, J. Stat. Mech.: Theory Exp. 7, P07008, (2011).

[22] R. Mauri, Non-Equilibrium Thermodynamics in Multiphase Flows (Chapter 2), 13-24, Springer, Dordrecht, The Netherlands, 2013.
[23] J.-S. Rattinacannou, EPJ Web of conferences, 79, 01006, (2014).
[24] Y.-F. Chang, Q.-R. Chou, J.-Y. Lin, and C.-H. Lee, Appl. Phys. A 86, 193, (2007).
[25] K. J. Morton, G. Nieberg, S. Bai, and S. Y. Chou, Nanotechnology 19, 345301, (2008).
[26] M. D. Henry, ICP Etching of Silicon for Micro and Nanoscale Devices, Ph.D. thesis, Caltech, CA, 2010.
[27] J. W. Goodby, Phase Structures of Calamitic Liquid Crystals, in Handbook of Liquid Crystals 2A, 12-13 Demus D. Ed., Wiley, New York, 1998.

CONTENTS

Events and Personalia

Bulk Materials

Nanostructures and Nanomaterils

Device Physics and Technologies

Miscellaneous and General Physics